Shock-tube investigation of key reactions for chemiluminescence in various combustion systems

Von der Fakultät für Ingenieurwissenschaften, Abteilung Maschinenbau und Verfahrenstechnik

der

Universität Duisburg-Essen

zur Erlangung des akademischen Grades

eines

Doktors der Ingenieurwissenschaften

Dr.-Ing.

genehmigte Dissertation

von

Metehan Bozkurt

aus

Hattingen

Gutachter:
Univ.-Prof. Dr. rer. nat. Christof Schulz
Univ.-Prof. Dr. rer. nat. Matthias Olzmann
Tag der mündlichen Prüfung: 30.07.2013

Abstract

Existing combustion systems, especially gas turbines in power generation applications must be optimized with regard to the reduction of pollutant emission and increase of efficiency. Combustion under fuel-lean conditions is beneficial for a significant reduction of NO_x and soot formation. However, these operating conditions can lead to undesired combustion phenomena such as combustion-induced oscillations and flame flash back which must be avoided. For this purpose, fundamental knowledge of the underlying chemical processes is required. Non-intrusive optical methods such as the use of chemiluminescence are potential practical approaches to provide combustion relevant information for the development of combustion apparatus and process control. This requires knowledge of the formation reactions of chemiluminescence as well as adequate kinetics models that link the light intensity to relevant combustion parameters such as local heat release.

An accurate description of chemiluminescence fundamentally depends on the corresponding ground-state chemistry. For small hydrocarbons such as CH_4 and C_2H_2 detailed reaction mechanisms already exist which were used as a base for the development of OH* and CH* sub-mechanisms in the present work. The present work was devoted to study the formation reactions of OH* and CH* chemiluminescence in shock tubes time-resolved detection of the emission with a photomultiplier with narrowband interference filters. The signals were compared to the corresponding excited-state species concentrations from simulations where based on established ground-state mechanisms, OH* and CH* kinetics models were compiled and validated with the experimental data from the present work. Based on the present work, the reactions H + O + M = OH* + M and CH + O_2 = OH* + CO are identified as the main OH* formation channels in hydrogen and hydrocarbon oxidation and their corresponding rate coefficients are determined as $(1.5\pm0.45)\times10^{13}$ exp(−25.0 kJ mol^{-1}/RT) $cm^6mol^{-2}s^{-1}$ and $(8.0\pm2.56)\times10^{10}$ $cm^3mol^{-1}s^{-1}$, respectively. For CH* chemiluminescence the reactions C_2 + OH = CH* + CO and C_2H + O = CH* + CO are the most important formation reactions and their underlying rate coefficients are $(5.7\pm3.02)\times10^{13}$ $cm^3mol^{-1}s^{-1}$ and $(1.0\pm0.53)\times10^{12}$ exp(−10.9 kJ mol^{-1}/RT) $cm^3mol^{-1}s^{-1}$, respectively.

While for small hydrocarbons well-known ground-state mechanisms are available, reliable kinetics models for ethanol oxidation, especially for high temperatures, are sparse. Therefore, the formation of important intermediates and products (e.g., OH, C_2H_2, and CO_2) was studied for ethanol oxidation by time-of-flight mass spectrometry and ring-dye laser absorption spectroscopy under shock-tube conditions. The experimental data were compared to simulations using different reaction mechanisms from the literature and recommendations for the improvement of the corresponding mechanisms were suggested.

Zusammenfassung

Bestehende Verbrennungssysteme, insbesondere Gasturbinen für die Erzeugung von Strom, müssen in Hinblick auf die Reduzierung des Rohstoffeinsatzes und des Ausstoßes von Emissionen optimiert werden. Hierbei kann die Verbrennung unter mageren Mischungsbedingungen zu einer signifikanten Reduzierung der Stickoxid- und Rußbildung führen. Diese Betriebszustände führen jedoch teilweise zu unerwünschten Schwingungen und Flammenrückschlag innerhalb der Brennkammer, die vermieden werden müssen. Hierfür ist ein grundlegendes Wissen über den zugrundeliegenden Verbrennungsprozess erforderlich. Nichtinvasive optische Methoden wie das Flammenleuchten sind potentielle Ansätze zur Bereitstellung von verbrennungsrelevanten Informationen für die Entwicklung von Verbrennungskonzepten und deren Regelung. Dies erfordert jedoch zum einen die Kenntnis über die Bildungsreaktionen der Chemilumineszenz und zum anderen sind geeignete Kinetikmodelle zur Beschreibung erforderlich.

Die Beschreibung der Chemilumineszenz erfordert genaue Kenntnis über die zugrundeliegende Grundzustandschemie. Für einfache Kohlenwasserstoffverbindungen wie z.B. CH_4 oder C_2H_2 existieren bereits gut validierte Modelle, die in der vorliegenden Arbeit als Basis für die Entwicklung von OH*- und CH*-Mechanismen verwendet wurden. Im Rahmen dieser Arbeit wurden die Bildungsreaktionen der OH*- und CH*-Chemilumineszenz in Stoßwellenreaktoren mit Hilfe von Emissionsmessungen untersucht. Hierbei wurde das Flammleuchten mit einer Kombination aus Photomultiplier und schmalbandigem Interferenzfilter zeitaufgelöst gemessen. Basierend auf etablierten Mechanismen zur Beschreibung der Grundzustandschemie wurden Kinetikmodelle für OH*- und CH*-Chemilumineszenz aufgestellt und mithilfe der experimentellen Daten validiert. Die Reaktionen H + O + M = OH* + M und CH + O_2 = OH* + CO wurden als Hauptreaktionen für die Bildung von OH* bei der Oxidation von Wasserstoff oder Kohlenwasserstoffen identifiziert und ihre zugrundeliegenden Geschwindigkeitskoeffizienten wurden ermittelt mit $(1.5\pm0.45)\times10^{13}$ exp(−25.0 kJ mol^{-1}/RT) cm^{6}mol^{-2}s^{-1} bzw. $(8.0\pm2.56)\times10^{10}$ cm^{3}mol^{-1}s^{-1}. Für CH*-Chemilumineszenz wurden die Reaktionen C_2 + OH = CH* + CO und C_2H + O = CH* + CO als wichtigste Bildungsreaktionen identifiziert und mit den Geschwindigkeitskoeffizient $(5.7\pm3.02)\times10^{13}$ cm^{3}mol^{-1}s^{-1} bzw. $(1.0\pm0.53)\times10^{12}$ exp(−10.9 kJ mol^{-1}/RT) cm^{3}mol^{-1}s^{-1}.

Während für kleine Kohlenwasserstoffe etablierte Mechanismen vorliegen, ist der Reaktionsmechanismus der Verbrennung von Ethanol, insbesondere bei hohen Temperaturen, nur unzureichend bekannt. Daher wurde im Rahmen dieser Arbeit die Bildung von wichtigen Intermediaten und Produkten (u.a. OH, C_2H_2, CO_2) bei der Oxidation von Ethanol im Stoßwellenrohr mittels Flugzeit-Massenspektrometrie und Farbstoff-Ringlaser-Absorptionsspektroskopie untersucht und mit verschiedenen Reaktionsmechanismen verglichen, die zusätzliche Daten zur Verbesserung und weiteren Validierung der bestehenden Modelle liefern.

Content

1. Introduction 1

2. Theoretical background 4

2.1. Reaction kinetics 4

2.2. Kinetics of complex reaction systems 6

2.2.1. H_2 mechanism 6

2.2.2. CH_4 mechanism 7

2.2.3. C_2H_2 and C_2H_4 mechanisms 7

2.2.4. C_2H_5OH mechanism 8

2.3. Chemiluminescence 9

2.3.1. Fundamentals of the formation of chemiluminescent species 10

2.3.2. OH* chemiluminescence 13

2.3.3. CH* chemiluminescence 14

2.3.4. C_2* chemiluminescence 14

2.3.5. CO_2* chemiluminescence 15

2.3.6. Spectroscopic properties of chemiluminescent species 15

2.4. Shock-tube fundamentals 16

3. Experimental 20

3.1. Shock-tubes for kinetics studies in highly diluted systems 20

3.1.1. Chemiluminescence emission detection 21

3.1.2. Ring-dye laser absorption measurements 23

3.2. Shock-tube facility for the validation of reaction mechanism at percent-level concentrations 30

3.2.1. Time-of-flight mass spectrometry 30

4. Results and discussion 33

4.1. Shock-tube measurements of OH* chemiluminescence 33

4.1.1. Review of OH* kinetics 33

4.1.2. Strategy of investigating OH* chemiluminescence 35

4.1.3. OH* chemiluminescence in H_2/O_2/Ar systems 36

4.1.4. OH* formation in $H_2/O_2/CH_4$/Ar systems 45
4.1.5. OH* chemiluminescence in CH_4 systems 48
4.1.6. OH* chemiluminescence in C_2H_2 systems 51
4.1.7. OH* chemiluminescence in C_2H_4 systems 57
4.1.8. OH* chemiluminescence in C_2H_5OH systems 60
4.1.9. OH* kinetics model 62
4.1.10. Additional validation of the OH*-chemiluminescence mechanism with laminar premixed flames 64
4.2. Shock-tube measurements of CH* chemiluminescence 67
4.2.1. Review of CH* kinetics 67
4.2.2. Strategy of the investigation of CH* chemiluminescence 70
4.2.3. CH* chemiluminescence in C_2H_2 mixtures 70
4.2.4. CH* chemiluminescence in C_2H_4 systems 80
4.2.5. CH* chemiluminescence in CH_4 systems 83
4.2.6. CH* chemiluminescence in C_2H_5OH systems 86
4.2.7. CH* kinetics model 91
4.2.8. Additional validation of the CH* chemiluminescence mechanism with laminar premixed flames 92
4.3. Validation of the ethanol ground-state chemistry 95
4.3.1. Time-of-flight mass spectrometry of ethanol pyrolysis and oxidation under shock-heated conditions 96
4.3.2. Ring-dye laser measurements of OH 103
5. Conclusions 106
6. Own publications 110
7. Bibliography 111
8. List of abbreviations 124
9. Symbols 125
10. Acknowledgement 127

1. Introduction

Ecological and economical restrictions have pushed constraints to reduce fossil fuel consumption and pollutant emissions that are mainly attributed to electricity production and transportation. The prospective development of renewable power generation and low-emission internal combustion (IC) engines technologies [1] are the most promising approaches to protect the environment. Nevertheless, conventional combustion of hydrocarbons will still be the most important energy source for the next decades. Therefore, optimization of existing combustion technologies based on fossil fuels is important.

Furthermore, renewable energy sources such as wind power and solar power plants show high fluctuations in their energy production depending on the meteorological conditions. Hence, conventional energy production must be designed to rapidly cover the energy demand for peak-period demand or for unfavorable weather conditions. Compared to coal-fired power plants, gas-fired power plants have a high flexibility with regard to short starting times. Furthermore, they emit up to 60% less carbon dioxide (CO_2) [2], which makes them very attractive for future electricity production. However, due to higher fuel costs, gas-fired power plants are playing only a minor role in global electricity generation. Therefore, the efficiency of gas-turbine combustion must be increased to make them competitive with other conventional combustion systems. For this purpose, operating gas turbines at low temperatures or fuel-lean conditions is required to further reduce pollution emission and to increase fuel efficiency. However, these conditions can cause unstable combustion states in terms of thermoacoustic instabilities and flame flash-back [3] due to heat-release fluctuations which can lead to destructive pressure oscillations within the combustor. Preventing this effect requires a fundamental knowledge of the underlying chemical reactions which can be gathered by local heat-release rate and equivalence-ratio measurements based on chemiluminescence to avoid such undesired combustion phenomena. The knowledge of these two combustion parameters is important to improve the combustor design with regard to fuel-efficiency, pollutant emission and combustion stability.

In research environments, sophisticated laser-based diagnostics are used to visualize the heat-release distribution in lab-scale flames. A state-of-the-art technique is heat-release imaging of formaldehyde (CH_2O) by means of laser-induced fluorescence (LIF) [4-5]. The LIF technique was successfully applied to characterize and to quantify spatially-resolved CH_2O and OH concentrations. These species are combustion-relevant intermediates and their combined concentrations correlate with the local heat release. The benefit of optical measurements is its non-intrusive nature which allows to study combustion processes without disturbing them. In harsh environments of practical applications, laser-diagnostic techniques, however, are not suitable for in-situ measurements. These techniques require an external light source and optical ports to couple the laser beam into the combustion chamber. Common industrial combus-

tors have limitations in the available geometry and are originally not designed to provide optical accessibility. Moreover, additional technical modifications would affect the combustion process. The required laser and imaging system make optical diagnostic very complex and expensive for practical applications. These disadvantages rule out conventional laser-based diagnostics for many field applications. Hence, less costly and straightforward optical techniques are desired. Luminescence of flames from chemical excitation of specific intermediate species, the so called chemiluminescence (CL), is a promising tool that can potentially provide information about local heat release [6-8] and equivalence ratios [9-11] once the underlying mechanisms are well enough understood.

Emission of UV- and visible light from electronically-excited species is a characteristic of hydrocarbon combustion. The most common chemiluminescent species are OH*, CH*, C_2*, and CO_2*, where the asterisk denotes electronic excitation as a consequence of chemical reactions. Chemiluminescence investigation is an important tool in the field of combustion research. The correlation of combustion relevant parameters such as heat release and fuel/air ratio with the chemiluminescence emission of excited state species was subject of many investigations [6, 12-15]. These studies showed that chemiluminescence can be used to spatially-resolve flame fronts [16] and to measure heat release [5, 17] and local equivalence ratios [6, 18-20].

Due to their simplicity, chemiluminescence sensors are desirable and can be easily designed for practical applications. However, the fundamental chemical kinetics leading to chemiluminescence, which is required for these applications, is still under debate. Overall, the capability to provide combustion-relevant information in combination with the simplicity of the detection system makes chemiluminescence very attractive for practical applications. This, however, requires the coupling of chemiluminescence signals with the underlying chemical processes in a quantitative manner. A quantitative and direct coupling between measured light intensity and the relevant combustion parameter (chemiluminescent species concentration, heat release rate or local equivalence ratio) is not straightforward. An interpretation of the measured signals can be done by linking the measured chemiluminescence intensities with the corresponding species concentrations taken from kinetics mechanisms.

In conventional ground-state mechanisms, chemiluminescence and its formation pathways are not considered because electronically excited species are several orders of magnitude less abundant compared to ground-state species. Therefore, chemiluminescent species have no influence on the global combustion process and are mostly not included in the ground-state mechanisms. For a quantitative investigation of the chemiluminescence, the available ground-state mechanisms must be extended by sub-models to describe the chemiluminescence pathways.

Based on the low concentrations of chemiluminescent species and the sophisticated interpretation, the characterization of the responsible formation reactions leading to chemiluminescence

and determining their associate rate coefficients is challenging. This issue is also reflected in the controversial kinetics data of chemiluminescence reactions in literature where notable deficiencies in the proposed reaction pathways and rate coefficients can be seen. This is because of the lack of consistent concentration information and the difficulty of specifically preparing species in the excited states.

Therefore, the aim of this study is to identify the key reactions forming OH* and CH* and to determine their corresponding rate coefficients in shock-tube experiments using a model-based calibration strategy. Here, various shock-heated mixtures were selected to selectively initiate reactions that generate chemiluminescent species. Time-resolved chemiluminescence emission profiles from both species were measured in various hydrogen and hydrocarbon combustion systems. These shock-tube experiments provide important data such as ignition delay times and concentration-time histories which are of fundamental importance for the development of chemical reaction mechanisms. Existing ground-state mechanisms were used as basis for the implementation of chemiluminescence formation and consumption reactions to describe the OH* and CH* concentration histories. The strategy of the present work is (i) Evaluation and extension of ground-state mechanism describing the underlying chemical process. (ii) Development and validation of a kinetics model of OH* chemiluminescence for hydrogen and hydrocarbon combustion under shock-tube and flame conditions. (iii) Development and validation of a kinetics model of CH* chemiluminescence for hydrocarbon combustion under shock-tube and flame conditions.

2. Theoretical background

2.1. Reaction kinetics

Classical thermodynamical equilibrium assumption can be used for the description of reaction systems where chemical reactions are fast compared to diffusion, transport processes and heat conduction. However, in combustion chemical reactions occur on similar time scales with other processes and therefore, the reaction kinetics must often be considered as a rate-determining process. The simplest combustion system is the oxidation of hydrogen. The combustion process is typically summarized by the global reaction

$$2H_2 + O_2 = 2H_2O \tag{2.1}$$

which describes the overall combustion process represented by the educts hydrogen and oxygen and the product water. However, combustion research revealed that the real oxidation process is more complex and involves intermediate species (O, H, OH) being formed and consumed during the combustion. The underlying detailed reaction mechanism is typically described with a set of elementary reactions. These elementary reactions describe a reactive molecular (collision) process and cannot be broken down to further reactions. A typical elementary reaction in hydrogen oxidation is the chain branching reaction of molecular oxygen with atomic hydrogen which provides high amounts of radicals accelerating the reaction progress.

$$O_2 + H = OH + O \tag{2.2}$$

Elementary reactions can be separated into three fundamental types. Unimolecular reactions represent the decomposition or isomerization of one reactant and are usually chain initiation reactions at the beginning of a combustion process. In a bimolecular reaction, two educts or intermediates react together to form product(s). This type of reaction is the most common one in combustions. Termolecular reactions incorporate three reactants and usually describe recombination reactions.

A reaction mechanism for combustion modeling consisting of a set of R elementary reactions j, $-j$ with N species (X_i) and their corresponding stoichiometric coefficients v_i can be described by the equation:

$$\sum_{i=1}^{N} v_{i,j} X_i \Leftrightarrow \sum_{i=1}^{N} v_{i,-j} X_i \qquad j = 1, \dots, R \tag{2.3}$$

The rate law of each species incorporating forward and backward reactions is given by:

$$\frac{d[X_i]}{dt} = \sum_{j=1}^{R} (v_{i,-j} - v_{i,j}) R_j \tag{2.4}$$

The rate of formation R_j describes the species conversion of the reaction in which forward and backward reactions are considered:

$$R_j = k_j \prod_{i=1}^{N} [X_i]^{v_{i,j}} - k_{-j} \prod_{i=1}^{N} [X_i]^{v_{i,-j}} \tag{2.5}$$

Aside from the corresponding species concentration, reactions strongly depend on the rate coefficients k_j and k_{-j}, respectively. These rate coefficients are characteristic for elementary reactions and therefore are essential for the fundamental knowledge of a reaction mechanism. A rate coefficient usually depends on the temperature and is expressed by a modified Arrhenius equation:

$$k_j(T) = A_j T^{n_j} \exp\left(-\frac{E_j}{RT}\right) \tag{2.6}$$

A_j is the pre-exponential factor, which is commonly only weakly temperature dependent. To account for this behavior, the original Arrhenius equation is extended by the term T^n. It is essential to specify the experimental T-range where the rate coefficients have been measured. The activation energy E_j corresponds to the energy barrier which must be overcome during the reaction. The value of the activation energies range between the sum of bonding energies for dissociation reactions and zero [21].

Based on the thermodynamics data (enthalpy, entropy, heat capacity) of each species, the equilibrium constant K_C can be determined which subsequently provides the rate coefficient for the reverse reaction k_{-j} according to equation from the rate coefficient k_j (2.7):

$$K_C = \frac{k_j}{k_{-j}} \tag{2.7}$$

Modern theoretical approaches such as Rice-Ramsperger-Kassel-Marcus (RRKM) theory [22-23] based on the transition-state theory [24] and statistical adiabatic channel model (SACM) [25-26] provide computational estimates for rate coefficients. Nevertheless, practical kinetics experiments are required to determine the underlying rate coefficients. Spectroscopic techniques such as absorption spectroscopy combined with shock-tube experiments are frequently employed to investigate ultrafast elementary reactions relevant for combustion. The high sensitivity of spectroscopic experiments coupled with the well-known experimental conditions from shock tubes enables accurate measurements in highly diluted mixtures without perturbation from transport processes. A detailed description of shock-tube fundamentals is given in section 2.4. This combination is necessary for the isolated study of elementary reactions by avoiding the influence of subsequent reactions which would interfere at high concentrations.

The corresponding time-resolved concentration profiles of the involved species are used to determine the corresponding rate coefficient k_j.

2.2. Kinetics of complex reaction systems

As introduced in the previous section, complex reaction mechanisms that describe the overall combustion process typically consist of a subset of elementary reactions incorporating the corresponding educts, the intermediate species and the products. The mechanism is built up as a sequence of elementary reactions and their corresponding formation and consumption rate coefficients. Typically, the mechanisms are validated with regard to global observables such as ignition delay times, flame velocities or concentration-time histories of important intermediate species like OH and CH radicals. Even the description of the simplest combustion reaction of hydrogen oxidation requires 20 reactions and 8 species [21]. For hydrocarbon combustion the complexity increases exponentially with the chain length and therefore hundreds (methane) [27] or thousands (liquid fuels) [28] of elementary reactions are required for the description of the process. Some of the reactions are directly measured, or are calculated based on quantum chemical calculations or are estimated. However, only a limited number of reactions are rate determining for the overall process.

2.2.1. H_2 mechanism

The common characteristic of hydrogen oxidation mechanisms is a core mechanism consisting of these chain-branching and propagation reactions (i) $H + O_2 = OH + O$, (ii) $H_2 + O = OH + H$, (iii) $H_2 + OH = H_2O + H$, and (iv) $OH + OH = H_2O + O$. These four reactions are the most prominent reactions in all hydrogen mechanisms while the existence of other reactions can vary. In general, hydrogen as well as hydrocarbon combustion shows very strong sensitivity towards the reaction (i) which is a rate-determining reaction.

A hydrogen oxidation mechanism describing the ground-state oxidation process was taken from Warnatz mechanism [21]. It includes temperature as well as pressure-dependent reactions and has been recently documented in [29] where the rate coefficients of the elementary reactions are based on the recommendations of Baulch et al. [30]. This mechanism is validated with respect to flame velocity (5 – 70 fuel percentage) and ignition delay times in the temperature range from 950 – 3000 K. The absolute concentration of the major species (H_2, O_2, H_2O, H, OH, O) were in very good agreement with species concentration measurements from [31]. This reaction mechanism was used in the present work as a base to develop an OH* submechanism in H_2/O_2 combustion systems.

2.2.2. CH_4 mechanism

There is a consensus in the description of the hydrocarbon oxidation which is typically initiated by chain-branching reactions where H, O, and OH radicals are formed which interact with fuel molecules forming alkyl radicals. Especially the ignition delay time is very sensitive towards the chain-branching reaction $H + O_2 = OH + O$ which controls the break-up of the fuel. These alkyl radicals further decompose and accelerate the combustion progress. In case of methane oxidation, CH_3 radicals are thermally formed by H-atom abstraction or by chain-branching reactions according to the above-mentioned scheme. Formaldehyde (CH_2O) is formed from CH_3 which reacts instantaneously to HCO forming CO and finally generating CO_2.

In the present work, the simulations of methane combustion were performed using the state of the art mechanism GRI3.0 [27]. This mechanism incorporates 53 species and 325 elementary reactions, which was extensively validated for a wide range of conditions where various shock-tube and flame experiments were considered. The validation conditions in terms of temperature, pressure and mixture conditions are comparable to our experiments. While the performance of the GRI3.0 mechanism [27] for highly diluted systems for low pressures and temperatures is well, there are deficiencies in predicting the ignition delay times for pressures above 60 bar. However, the altering performance with increasing pressure is not a methane-specific issue and can be observed for various combustion systems.

The GRI3.0 mechanism [27] contains a comprehensive nitrogen chemistry validated with regard to the formation of NO_x. However, the model was not explicitly tested for the oxidation of methane with N_2O which was used as an alternative oxidizer within the present study to generate high amounts of atomic oxygen which will be extensively described in section 4.1.5. The GRI3.0 mechanism has been established as the most reliable mechanism for the numerical analysis of methane oxidation. Therefore, the present shock-tube measurements are consistently simulated using the GRI mechanism.

2.2.3. C_2H_2 and C_2H_4 mechanisms

There are different well-validated comprehensive mechanism for hydrocarbon combustion which are built up in a hierarchical manner starting from elementary hydrogen and methane combustion towards acetylene [32-34]. According to the reaction process for methane combustion, the oxidation of hydrocarbons is typically initiated by H-atom abstraction or in case of acetylene and ethylene, by unimolecular dissociation of the fuel by C—C cleavage. In contrast to the available kinetics mechanisms, Wang and Laskin [35] reported that the oxidation of acetylene or ethylene under shock-tube conditions can be initiated by a third pathway via vinylidene which can significantly enhance the formation of the radical pool.

In the present study, the ground-state model from Wang and Laskin [35] was considered for the interpretation of acetylene and ethylene combustion. The mechanism is especially developed for high-temperature oxidation of both fuels and it consists of 75 species and 529 reactions. Chemistry of higher hydrocarbons is more complex compared to methane combustion and thus, requires in-depth validation efforts. The mechanism was previously optimized for a wide range of conditions with regard to shock-tube experiments, laminar burning velocity and burner-stabilized flames. The entire validation data are published in [35].

2.2.4. C_2H_5OH mechanism

The first comprehensive oxidation model for ethanol was developed by Natarajan and Bashkaran [36] more than 20 years ago consisting of 56 elementary reactions. They proposed the C—C cleavage of ethanol as the primary decomposition reaction forming CH_2OH and CH_3. This mechanism was validated based on ignition delay times from shock-tube experiments within a temperature range of 1300 and 1700 K at 1.0 and 2.0 bar. Borisov et al. [37] extended the mechanism from [36] by implementing additional pyrolysis and chain-branching reactions which were initially not considered in [36]. They tested the model with regard to ignition delay times from shock tubes for different equivalence ratios from lean to fuel-rich conditions around atmospheric pressures. In 1999, Marinov [38] developed a comprehensive reaction mechanism which considers 56 species, contains 351 reversible reactions and covers the entire oxidation chemistry from hydrogen (H_2) to propane (C_3H_8). The validation process was done based on various experimental data sets such as ignition delay times from shock tubes, laminar flame speed measurements from a combustion bomb and a counterflow twin flame, and species concentration profiles from ethanol oxidation in jet-stirred and turbulent flow reactors. The experimental conditions ramped between 1000 and 1700 K, a pressure range of 1.0 – 4.5 bar and various equivalence ratios from 0.5 to 2.0. More recently, Saxena and Williams [39] presented a kinetics mechanisms consisting of 288 elementary reactions and involving 57 species. The model was tested against measured concentration profiles in counterflow flames, ignition delay times, and burning velocities. Li et al. [40] measured the pyrolysis of ethanol in a variable pressure flow reactor. According to the results from Marinov [38], they emphasized that the pyrolysis is very sensitive to the decomposition reactions (i) $C_2H_5OH = C_2H_4 + H_2O$ and (ii) $C_2H_5OH = CH_3 + CH_2OH$. However, they pointed out that the Marinov mechanism underestimates the contribution of the first reaction. Based on their experimental results, they determined rate coefficient for reaction (i) where good agreement was found with theoretical work from Tsang [41] and shock-tube measurements from Herzler et al [42]. More recently, Li et al. [43] presented a detailed oxidation mechanism for ethanol consisting of 238 elementary reactions and 39 species which was validated, inter alia, with regard to concentration profiles from their flow reactor experiments. The predictions from their mechanism were compared with the results from [38] and [39].

According to the observations from [44] where ethanol was mainly consumed during the induction period, any ethanol oxidation mechanism must be developed based on the fundamental knowledge of the ethanol pyrolysis. While for temperatures below 1000 K the decomposition of ethanol predominantly starts with H-atom abstraction, for temperatures above 1000 K the C—C cleavage forming CH_3 and CH_2OH is suggested to be the major decomposition step. However, recent studies reveal that the unimolecular decomposition of ethanol towards C_2H_4 and H_2O is more important than the methyl abstraction [38, 45].

In the present work, the ethanol combustion was simulated using a detailed kinetics model from Marinov [38]. Kiecherer et al. [45] revised the main decomposition reactions of ethanol in the Marinov mechanism based on statistical reaction theory. These recommendations were also used for the simulation of the ethanol-based mixtures. For additional simulations of the ethanol oxidation, the model from Saxena and Williams [39] was used.

2.3. Chemiluminescence

Figure 2.1 shows exemplarily a simplified reaction pathway for methane oxidation starting from the CH_4 molecule to the final product CO_2. The important intermediate species in the ground-state are illustrated and the underlying reaction pathways describing the chemical interaction are indicated by solid lines. Because of the immanent importance of, the focus of the combustion research is concentrated on these ground-state species while the investigation of these species usually requires sophisticated experimental equipment.

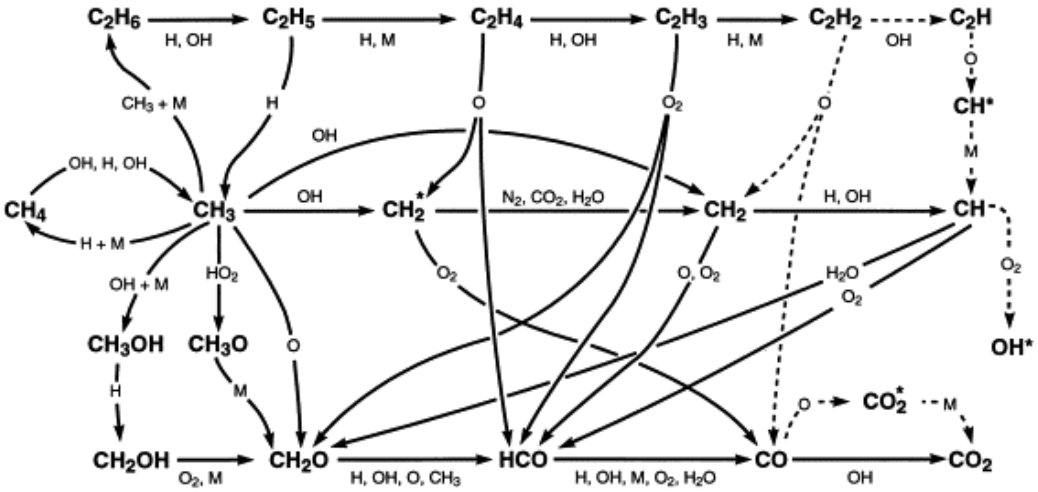

Figure 2.1: Simplified reaction pathway for methane oxidation from Najm et al. [46] including potential reaction channels leading to chemiluminescent species.

Chemiluminescence investigation has also the capability to provide fundamental information of the combustion process such as local heat release or equivalence ratios. Because the occurrence of chemiluminescence is an intrinsic feature in the combustion process, a more straightforward and cheap diagnostics tool can be developed for combustion research. For this

purpose, the main challenge which has to be overcome is the linkage of the measured chemiluminescence emission with the underlying reaction mechanism.

As illustrated by the dashed lines in Figure 2.1, chemiluminescence formation occurs aside from the global reaction process. Because chemiluminescent species are several orders of magnitude less abundant compared to their corresponding ground-state molecules, they have a negligible influence on the overall reaction process and therefore, they are typically not considered within the reaction mechanism. Based on the interaction of the ground-state mechanism, which provides the precursor molecules, with the chemiluminescence formation, the correct description of the formation reactions of chemiluminescence crucially depends on the knowledge of the underlying ground-state chemistry and the elementary reactions that quench the electronically-excited states. Therefore, the first and most challenging issue is the controversial discussion in identifying the formation reactions leading to chemiluminescence and their corresponding rate coefficients which is briefly introduced in 2.3.2 and 2.3.3. The second challenge which must be overcome is the accurate quantitative prediction of transient intermediate species such as CH molecules which are of fundamental importance for a reliable investigation of chemiluminescence kinetics. A detailed literature review and a comprehensive discussion of OH* and CH* kinetics is presented in sections 4.1.1 and 4.2.1. The present study is devoted to investigate the formation pathways of OH* and CH* chemiluminescence and to identify their rate coefficients.

2.3.1. Fundamentals of the formation of chemiluminescent species

Figure 2.2 shows a typical emission spectrum of a premixed methane-air flame at fuel-rich conditions. Four chemiluminescent species (OH*, CH* C_2* and CO_2*) in their different electronic states are frequently studied in hydrocarbon combustion.

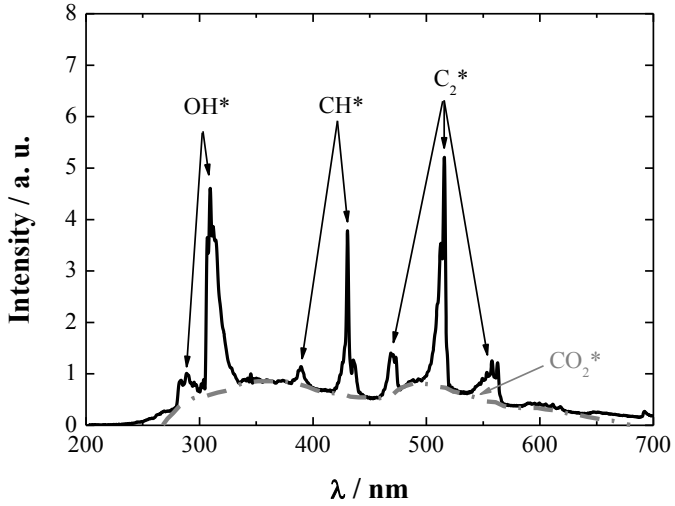

Figure 2.2: Typical flame emission spectrum of a premixed methane air flame ($\phi = 0.8$). Emission peaks from various chemiluminescent species and broadband radiation from CO_2 background [47].

While the kinetics of OH* and CH* were extensively studied in the past [48-53]. Only sparse data are available for C_2* [48, 54-56] and CO_2* [57-60]. Owing the large deviations in identifying the key reactions leading to chemiluminescent species and their corresponding kinetics data, chemiluminescence investigations are still in the focus of recent combustion research [15, 61-65].

Although they are thermodynamically disadvantageous compared to their corresponding ground-state reactions, chemical reactions of intermediate ground-state atoms and molecules can also lead to the formation of electronically-excited species. Figure 2.3 exemplarily show the enthalpy change for reactions producing ground-state products and their corresponding excited-state products.

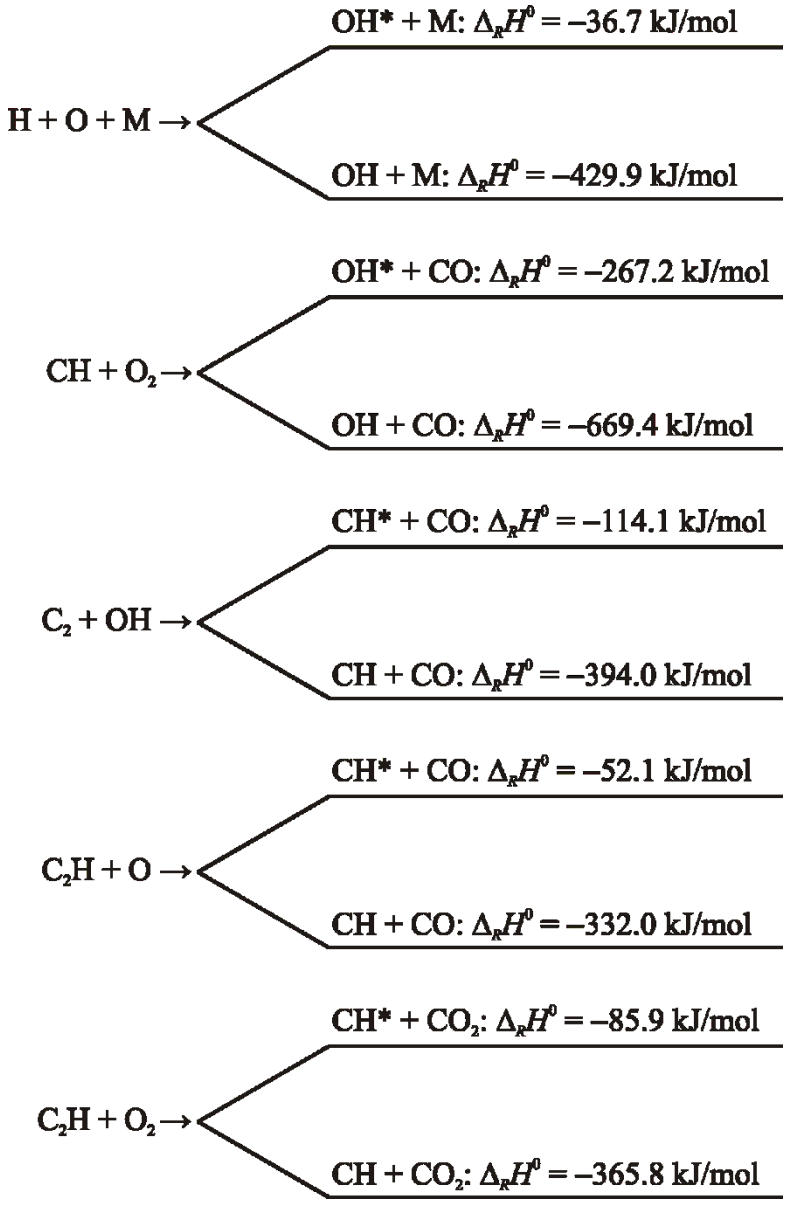

Figure 2.3: Comparison of the enthalpy change of potential OH* and CH* formation reactions and their corresponding ground-state reactions.

The excitation of chemiluminescent species is attributed to chemical excitation instead of thermal excitation [66]. Aside from the chemical excitation, thermal activation can also occur. However, thermal excitation of ground-state molecules is usually considered as negligible for common experimental conditions because of energetic considerations. Thermal excitation must be considered especially for high temperatures above 2000 K [66-67]. Due to the energy excess of the excited-state species, these chemiluminescent species are short-lived and the energy is partially removed by photon emission which can be characterized by the photon energy release $h\nu = E_2 - E_1$. However, chemiluminescent species commonly are de-excited to the electronic ground state via collisional quenching [68].

The dynamic of chemiluminescence can be described by means of the potential energies surface illustrated in Figure 2.4. The educts E are thermally activated during the chemical reaction and form an activated complex in the transition state (TS). Typically, most reactions occur in the electronic ground state and therefore the activated complex is directly transferred to the products P (refer to pathway *a*). This type of reaction is characterized in the literature as adiabatic reaction [69]. However, in non-adiabatic reactions the activated complex can be transferred to the electronic excited state (refer to pathway *b*) which finally leads to the formation of electronically-excited state products P*. The excess energy is then removed by photon emission or collisional quenching forming the electronic ground state P. These reactions are subject of combustion and photochemistry processes.

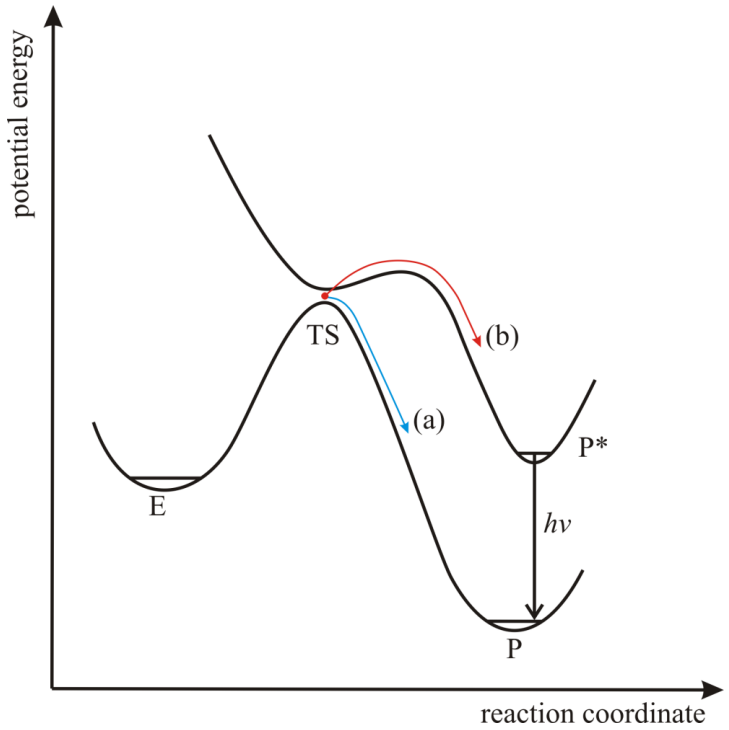

Figure 2.4: Principle reaction pathway in a potential energy diagram (a) for a conventional chemical reaction and (b) for a chemiluminescent reaction [69].

Radiative de-excitation of chemiluminescent species is characterized by A_{21}, denoted as Einstein coefficient of spontaneous emission. Compared to radiative decay of excited-state species, the energy transfer by collisional quenching is more likely to occur. Through non-reactive collisions with ambient molecules, excited species return to a lower state by transferring their excess energy to the collision partner.

In addition to non-radiative energy transfer of an excited-state molecule by collision quenching, reactive collisions can also occur and are exemplarily reported in [70-72]. Due to lowering effects of the endoergic reaction barrier, the chemical reactivity of electronically excited molecules is several hundreds of times faster than their corresponding ground-state species [73-74]. Recently, Starik and co-workers [75] studied the influence of vibrationally and electronically excited O_2 as a combustion accelerator for hydrogen oxidation. They demonstrated that the supersonic flow of H_2/O_2 mixture can be ignited within short exposure distances even for low temperatures when excited molecules were available whereas for cases without electronic activation an ignition could not be observed. Furthermore, the reactive consumption of OH* via the reaction OH* + H_2 = H + H_2O was in the scope of several studies [70-72]. For CH* chemiluminescence, ground-state CH molecules were suggested to be more reactive compared to excited-state CH [76] . Based on the short lifetimes of CH*, the de-excitation of CH* towards CH is more likely than the reactive consumption of CH*. However, due to the lack of consistent information, the consumption of chemiluminescent species via reactive collisions is commonly neglected in excited-state mechanisms.

2.3.2. OH* chemiluminescence

OH* chemiluminescence is abundant in hydrogen and hydrocarbon combustion. The UV emission at 306 nm is attributed to the OH($A^2\Sigma^+ \rightarrow X^2\Pi$) transition. Other potential transitions from the B and C states are not identified in flame experiments. The key reactions responsible for OH* in the combustion are under debate. Chemical build-up of OH* via reactions H + O + M = OH* + M and H + OH + OH = OH* + H_2O are frequently considered to be responsible for the production of OH* chemiluminescence in hydrogen combustion. Whereas in hydrocarbon combustion, there is accordance in identifying the formation channel of OH* chemiluminescence as CH + O_2 = OH* + CO [51, 77-78]. A detailed discussion of the OH* kinetics is given in section 4.1.1. In addition, thermal excitation must be considered also as potential pathway transferring ground-state OH molecules into its A state for temperatures above 2800 K. In a recent study based on an opposed oxy-methane diffusion flame from De Leo et al. [67], 35% of the OH* was attributed to thermal excitation. It was reported that this ratio further shifts towards thermal formation of OH* for increasing temperatures. In the present study, the equilibrium of OH molecules was used to calibrate the optical detection system with regard to absolute OH* concentration [79]. Based on this procedure, the chemical excita-

tion pathway of OH* CL at lower temperatures was investigated and model-based reconstructed. A detailed description will be presented in section 4.1.1.

2.3.3. CH* chemiluminescence

CH* is also an important emitter in hydrocarbon combustion. The strongest transition with an emission in the blue-violet range at 430 nm is assigned to the $CH(A^2\Delta \rightarrow X^2\Pi)$ transition. Additionally, CH* emission around 390 nm due to the $CH(B^2\Sigma^- \rightarrow X^2\Pi)$ transition was recently investigated in flames [65]. Kathrotia et al. [65] pointed out that the A–X transition contributes about 80% of the total chemiluminescence emission whereas the residual amount is attributed to the B–X transition. In previous work, various reactions were suggested to be responsible for CH* formation. However, the available kinetics data varies in several orders of magnitude. Recent studies presumed, that three potential reactions $C_2 + OH = CH^* + CO$, $C_2H + O = CH^* + CO$ and $C_2H + O_2 = CH^* + CO_2$ must be considered for CH* chemiluminescence. Large deviations have been reported in determining the dominating formation reaction and their corresponding rate coefficients. Similar to OH* chemiluminescence, thermal excitation of CH* also occurs especially for high temperatures and was reported in a recent diffusion flame study [67]. The authors stated that for temperatures around 3000 K thermal excitation contributes up to 30% to the total excited state CH*. A detailed discussion of CH* kinetics will be given in section 4.2.1.

2.3.4. C_2* chemiluminescence

C_2* chemiluminescence in the blue-green spectrum between 436 and 564 nm from the $C_2(d^3\Pi \rightarrow a^3\Pi)$ transition, also denoted as Swan bands, especially occurs under fuel-rich conditions. Therefore, it can provide information about areas susceptible to soot formation. Gaydon [48] suggested the reaction $^1CH_2 + C = C_2^* + H_2$ as formation reaction of C_2*. Later on, Savadatti and Broida [54] proposed the reaction $C_3 + O = C_2^* + CO$. Smith and coworkers studied C_2* formation in various premixed hydrocarbon flames by laser-induced fluorescence (LIF) imaging measurements [56]. They developed a sub-mechanism for C_2* kinetics and recommended rate coefficients for the two formation reactions stated above. More recently, Kathrotia et al. [65] studied C_2* formation amongst others in various premixed methane air flames. They found that their flame experiments can be reproduced when considering the two above-mentioned recommended reactions from [48] and [54]. However, their results suffer from simulation uncertainties due to the lack of reliable precursor concentrations.

2.3.5. CO_2* chemiluminescence

Flame spectra of hydrocarbons typically show a significant background emission caused by CO_2* chemiluminescence. In contrast to the narrow emission bands of OH* and CH*, CO_2* emission occurs in a broad spectral range from 300 to 650 nm. Therefore, quantitative measurements of chemiluminescence under flame conditions require the knowledge of CO_2* formation and its contribution to the different emission band from the other chemiluminescent species. Jachimowski [80] and later on Baulch et al. [57] observed a proportionality of CO_2* chemiluminescence and the product of [CO] and [O]. Based on this finding, they concluded that the reaction CO + O (+ M) = CO_2* (+ M) is the main formation pathway of CO_2* which was already postulated by Broida and Gaydon [81] early in 1953. Hall et al. [53] also identified the reaction above as the main source of CO_2* chemiluminescence and showed that the emission is proportional to the CO and O concentrations. They reported that the broadband CO_2* radiation interferes with the CH* emission for temperatures below 1700 K and a correction of the initial CH* signal was applied. In the present work, interference of CH* and CO_2* chemiluminescence was not observed which is attributed to lower initial concentrations of the reactants compared to the experiments of [53]. This is potentially attributed to the lower initial concentrations of the reactants in the present work. More recently, Kopp et al. [60, 82] studied the broadband emission of CO_2* in shock-heated H_2, N_2O, CO and Ar mixtures by recording the emission signals at two wavelengths by means of separate interference filter and photomultiplier setups. The experiments were compared with simulations considering CO_2* and CH_2O* as potential sources of the background radiation. Based on this comparison, they concluded that the broadband emission is mainly attributed to CO_2*. However, the agreement between experiment and simulation was poor and they pointed out that further improvement of the CO_2* formation mechanism and the underlying rate coefficient is required.

2.3.6. Spectroscopic properties of chemiluminescent species

Brockhinke and co-workers [64] extensively studied rotationally-resolved chemiluminescence spectra of OH*, CH* and C_2* chemiluminescence under flame conditions. While their measured emission spectra for CH* and C_2* are close to the computed results using LIFBASE [83] and LASKINv^2 [84] assuming thermal equilibrium, the spectral shape of OH* chemiluminescence could not be described by assuming thermal distribution. This observation was already reported in [85-87]. Based on the high excess energy when generating OH(A) via chemical reaction from CH + O_2 = OH* + CO, high vibrational and rotational levels (v" = 6) are also accessible. However, for high vibrational states pre-dissociation of OH* is more likely to occur, therefore, v" ≤ 2 can be considered as an upper limit of the chemical excitation of OH. In general, higher vibrational and rotational levels are internally transferred to lower

states via both rotational (RET) and vibrational energy transfer (VET) indicated illustrated in Figure 2.5.

The de-excitation from the electronic excited state to the ground state occurs primarily via non-radiative transfer due to molecular collisions with ambient colliders. According to Kasha's rule, photon emission due to the vibrational transition from the excited state to the ground state occurs predominantly from the lowest vibrational level in the electronic excited state. Recently, Brockhinke et al. [64] reported that the A→X (1,0) and (0,0) transitions are responsible for the OH* emission spectrum in a low-pressure and atmospheric flames.

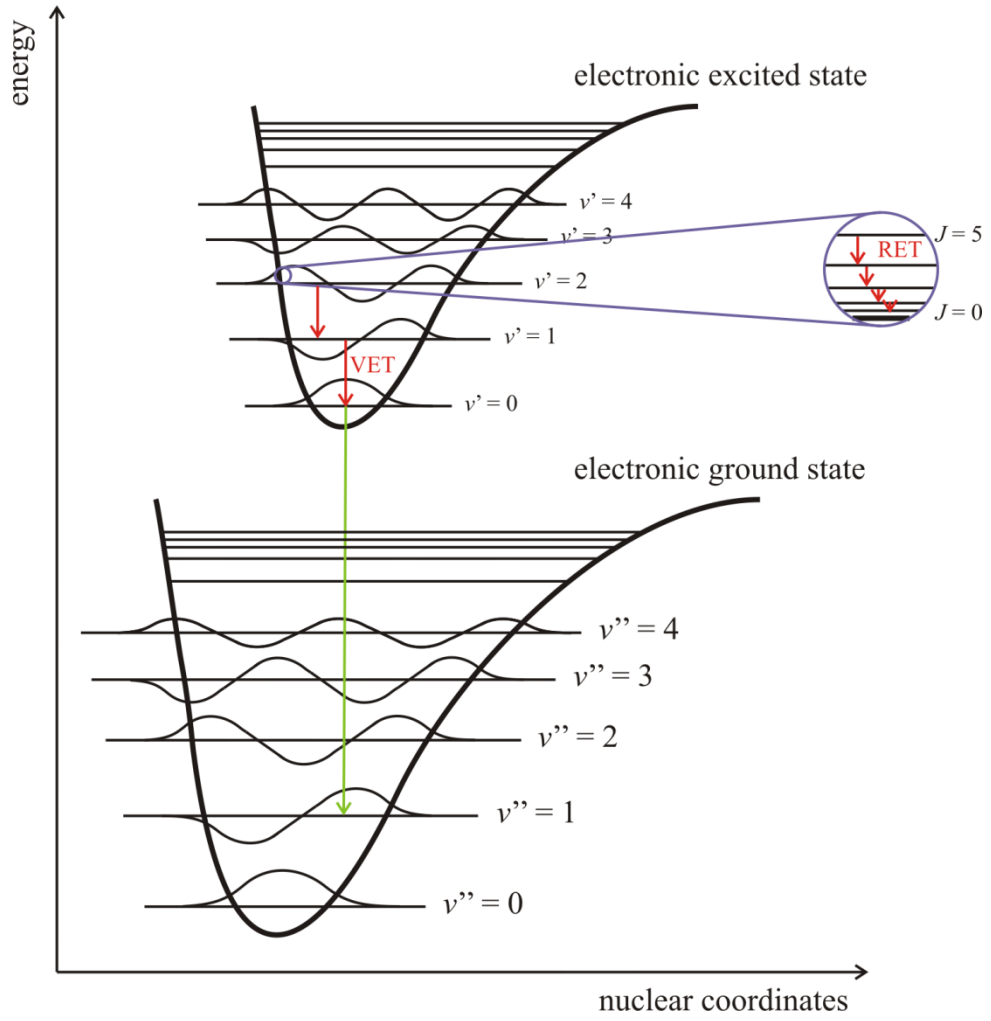

Figure 2.5: Schematic energy diagram of the electronic ground state and the excited state for a diatomic molecule. The red lines represent vibrational energy transfer (VET) and rotational energy transfer (RET). The green line represents one possible channel of the cumulated de-excitation (collisional quenching and radiative decay).

2.4. Shock-tube fundamentals

Shock tubes are suitable and powerful tools for the investigation of chemical kinetics and ignition delay times since more than 50 years [88-89]. In principle, a shock tube consists of two

sections divided by a diaphragm. The high-pressure section, also denoted as driver section, is filled with the driver gas, typically hydrogen or helium. Based on the different speed of sound for both driver gases and depending on the shock-tube design, hydrogen is used for high-temperature experiments for temperatures above 1400 K and for lower temperatures, helium is typically used. The low-pressure section, designated as driven section, is filled with the sample gas and provides optical ports for spectroscopic applications and potential additional sampling ports near the end flange. Because of the rapture of the aluminum diaphragm, a shock wave is formed induced by the pressure pulses that build a shock front. The wave front propagates through the test gas and causes an instantaneous pressure and temperature increase behind the incident shock wave. At the end wall, the shock wave reflects and passes the test gas again and induces to a second pressure and temperature increase (conditions behind the reflected shock wave).

The thermodynamic variables density ρ, pressure p and temperature T behind shock waves can be calculated by gasdynamics theory. Detailed literature to shock-tube characteristics can be found in [88-90]. For ideal gases, the step increase of pressure, density and temperature behind the incident shock wave (T_2, p_2 and ρ_2) can be described by using the conservation equations (mass flux, flux of momentum and energy per mass) with regard to the initial conditions T_1, p_1, and ρ_1:

$$\rho_1 u_1 = \rho_2 u_2 \tag{2.8}$$

$$\rho_1 u_1^2 + p_1 = \rho_2 u_2^2 + p_2 \tag{2.9}$$

$$\frac{1}{2}u_1^2 + h_1 = \frac{1}{2}u_2^2 + h_2 \tag{2.10}$$

Assuming that the behavior of the gas in the shock tube is ideal and the heat capacity is temperature independent, the upper equations can be transferred to Rankine-Hugoniot equations:

$$\frac{p_2}{p_1} = \frac{2\kappa \mathrm{Ma}_1^2 - (\kappa - 1)}{\kappa + 1} \tag{2.11}$$

$$\frac{\rho_2}{\rho_1} = \frac{(\kappa + 1)\mathrm{Ma}_1^2}{(\kappa - 1)\mathrm{Ma}_1^2 + 2} \tag{2.12}$$

$$\frac{T_2}{T_1} = \frac{p_2}{p_1} \times \frac{\rho_1}{\rho_2} \tag{2.13}$$

For ideal gases, the Mach number Ma can be determined from the shock-wave velocity:

$$\mathrm{Ma}_1 = \frac{v_s}{\sqrt{\kappa R T_1 / M}} \tag{2.14}$$

The molar mass M and the heat capacity ratio κ depend on the mixture composition of the test gas and can be calculated with regard to the initial conditions. Therefore, the shock-tube con-

ditions behind the incident shock wave only depend on the shock-wave velocity v_S. Hence, for the prediction of the shock-tube conditions the velocity is required only. This value is typically measured based on the pressure traces in the driven section due to the pressure jump behind the shock wave.

The conditions behind the reflected shock wave (T_5, p_5 and ρ_5) can be deduced based on the ideal shock assumption:

$$\frac{p_5}{p_2} = \frac{\frac{\kappa+1}{\kappa-1} + 2 - \frac{p_1}{2}}{1 + \frac{\kappa+1}{\kappa-1}\frac{p_1}{p_2}} \tag{2.15}$$

$$\frac{T_5}{T_2} = \frac{p_5}{p_2}\left(\frac{\frac{\kappa+1}{\kappa-1} + \frac{p_5}{p_2}}{1 + \frac{\kappa+1}{\kappa-1}\frac{p_5}{p_2}} \right) \tag{2.16}$$

The equations above consider ideal shock-tube conditions only. However, real-gas effects with regard to temperature, pressure and density deviations can influence the experimental conditions. Depending on the experimental conditions, they must be taken into account as well.

A schematic time-distance diagram of the shock-wave propagation is presented in Figure 2.6. The driven section is filled with the test gas and the initial conditions are designated as T_1 and p_1 in Figure 2.6a. The shock front is formed after the diaphragm ruptures by filling the high-pressure section with driver gas. The incident shock wave propagates into the low-pressure section and compresses the gas mixture adiabatically (cf. Figure 2.6b and c). The conditions behind the incident shock wave are denoted as T_2 and p_2. Simultaneously to the formation of the incident shock wave, a contact surface is generated and propagates with a lower velocity into the driven section. Furthermore, additional expansion waves are formed and propagate to the opposite direction into the driver section. The end wall of the low-pressure section reflects the shock front and the sample gas is compressed again (Figure 2.6d and e). After the reflection of the shock wave, conditions T_5 and p_5 are reached and the test gas remains static. As illustrated in Figure 2.6f, the sampling time Δt for a shock-tube experiment is limited by the arrival of the contact surface and its interaction with the reflected shock wave. The test gas is disturbed by the back reflection of the shock front which leads to unsteady conditions in terms of temperature and pressure. In the present study, the shock-tube design provides an observation time with steady experimental conditions of about 1.5 ms.

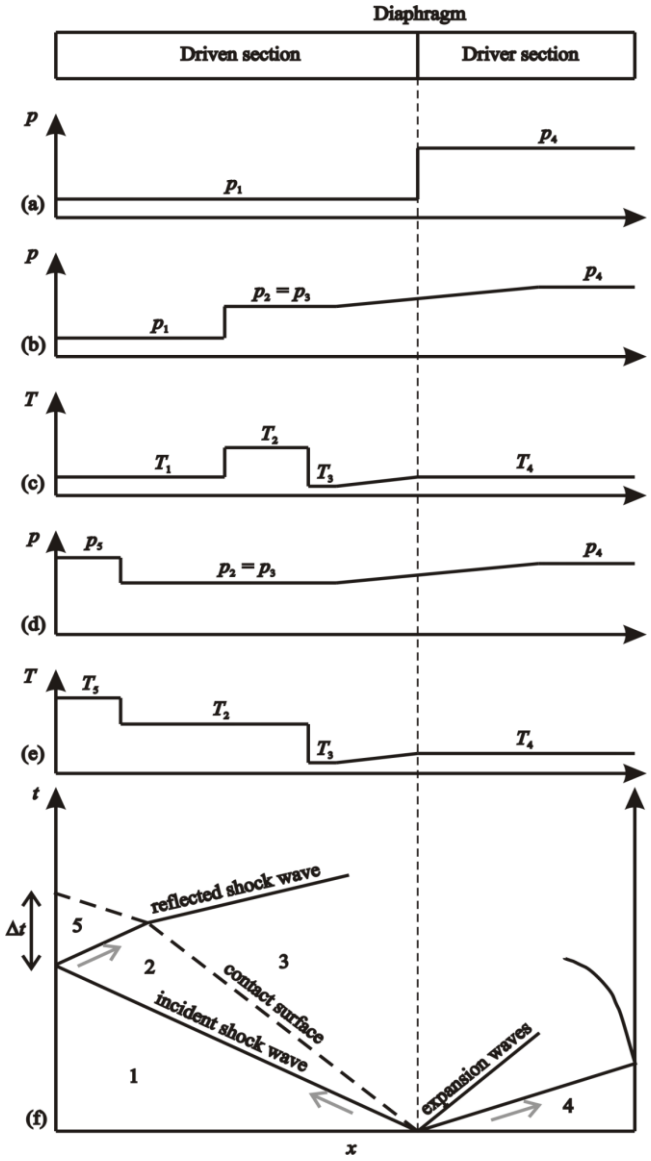

Figure 2.6: Schematic time-distance diagram of the shock-wave propagation according to [89].

3. Experimental

The step-wise increase of the temperature and the homogeneous heat up of the test gas in a shock tube within 1 μs allows studying the kinetics of fast gas-phase reactions without the influence of transport processes. Ideally, shock-tube conditions are characterized by a homogenous temperature distribution and a homogenous gas mixture. This prevents diffusion and transport processes, which enables to decouple the chemical processes from physical ones and allows studying chemistry under well-defined conditions. A suitable design of the shock tube and a large diameter can significantly reduce undesired wall and boundary layer effects.

Typical experimental conditions behind shock waves of $500\ \mathrm{K} \leq T_5 \leq 4000\ \mathrm{K}$ and $0.1\ \mathrm{bar} \leq p_5 \leq 150\ \mathrm{bar}$ offer the potential to study chemical process under conditions relevant for combustion. Nevertheless, there are some disadvantages of the shock-tube technique that must be considered. The observation time is limited by the impact of the contact surface and the shock wave which is depending on the shock-tube design, in particular by the length of the shock tube. Typical experimental time scales are in the range of few milliseconds. This time frame is typically sufficient for the investigation of many elementary reactions in conventional low-pressure shock tubes. Longer observation times are required for determining the ignition-delay times of practical fuels at low temperatures. This can be achieved by tailoring the driver gas [91] by conditioning the acoustic impedance to avoid a back-reflection of the contact surface. Thus, the experimental observation time can be extended up to 30 ms [91]. Furthermore, shock-tube experiments are single-shot type experiments and thus, averaging results from a series of experiments is not feasible which otherwise would increase the signal-to-noise ratio. Therefore, fast as well as sensitive measurement methods are required. Spectroscopic methods with laser-based diagnostics are usually applied which can fulfill the previous-mentioned requirements.

3.1. Shock-tubes for kinetics studies in highly diluted systems

The investigation of elementary reactions requires high experimental standards. Contamination of the shock tube affects the reliability of the experiments and must be prevented by the shock-tube design. The initial pressure before conducting an experiment was below 1×10^{-7} mbar. The high-vacuum requirement and the low concentration commitment together with the high purity of gases and the choice of highly-sensitive diagnostics aim at reducing the effect of secondary reactions and enable to isolate one or two reactions and to study ultrafast reactions. Due to the very high sensitivity and selectivity of direct absorption spectroscopy, the detection limits were ranging in the ppm-range depending on the spectroscopic properties of the absorbing species.

3.1.1. Chemiluminescence emission detection

Time-resolved chemiluminescence experiments were carried out in a stainless-steel shock tube (shock tube I) with a constant inner diameter of 79 mm. The shock-tube facility is equipped with turbo-molecular pumps to reach pressures for UHV purpose. An aluminum diaphragm (thickness: 50 µm) divides the shock tube into a driver section (length: 3.5 m) and a driven section (length: 5.7 m). Hydrogen was used as driver gas. The driver section was pumped down to 10^{-2} mbar. Prior to each experiment, the driven section was turbo-pumped to final pressures below 3×10^{-8} mbar. A schematic setup of the shock tube is shown in Figure 3.1.

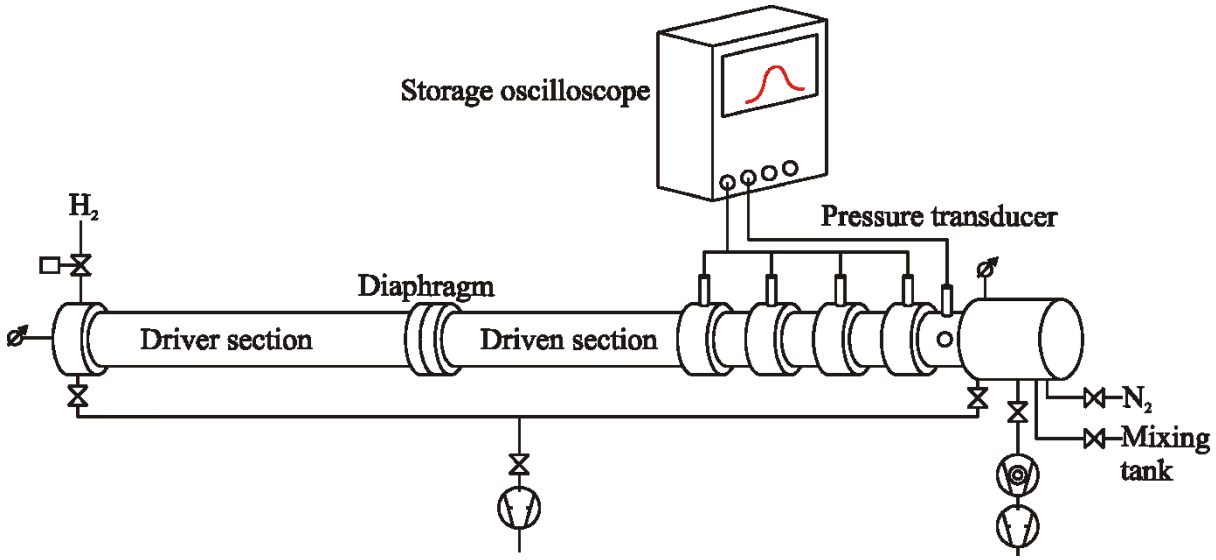

Figure 3.1: Schematics of shock tube I.

The incident shock speed was measured over three equidistant intervals using four piezo-electric pressure transducers (PCB 113A21) with a time resolution of 0.1 µs. Additionally, another pressure gauge (PCB 113A21) was placed close to the end-wall (distance: 40 mm) to localize zero-time for the ignition measurements. The temperature T_5 and pressure p_5 behind the shock wave were computed from the measured incident shock-wave velocity and attenuation using a one-dimensional shock model (shock tube code of the CHEMKIN Package [92]) with respect to the initial conditions p_1 and T_1. The estimated uncertainty in reflected shock temperature was less than ±15 K in the temperature and time range of our measurements. Four optical ports were located 40 mm upstream of the end flange that allows the detection of chemiluminescence.

Gas mixtures diluted in argon were prepared in a stainless-steel cylinder using the partial-pressure method. The cylinder was also evacuated by a separate turbo-molecular pump in between experiment series. The gas purities are stated in Table 3.1. In case of experiments with ethanol was injected into a separate tank and the desired partial pressure in the shock tube was controlled manometrically.

Table 3.1: Stated purities of the substances

Substance	**Purity / %**
Argon (Ar)	≥ 99.9999
Hydrogen (H_2)	≥ 99.999
Nitrous oxide (N_2O)	≥ 99.999
Oxygen (O_2)	≥ 99.998
Methane (CH_4)	≥ 99.999
Acetylene (C_2H_2)	≥ 99.6
Ethylene (C_2H_4)	≥ 99.995
Ethanol (C_2H_5OH)	≥ 99.9
Ammonia (NH_3)	≥ 99.998

The schematics of the CL detection system for OH* and CH* is illustrated in Figure 3.2. Measuring chemiluminescence with high temporal resolution requires the limitation of the detection to a narrow zone within the shock tube. Hence, two vertical slits were placed at 15 and 45 mm in front of each detector to narrow the detection solid angle. Their widths of 0.2 mm and 1 mm, respectively, were selected to provide an optimal balance between signal strength and time resolution. This setup provided a time resolution of 1 μs as determined from the light collection angle and the passing velocity of the reflected shock wave. Interference filters with center wavelengths of $\lambda_{OH^*} = 307$ nm and $\lambda_{CH^*} = 430$ nm, respectively, (both 10 nm FWHM) limited the emission spectra of OH* and CH* chemiluminescence to the transitions in the A–X systems. The chemiluminescence radiation was detected by two separate photomultipliers (OH*: Hamamatsu 1P28, CH*: Hamamatsu R955) with constant amplification voltage for all presented measurements. To achieve sufficient time resolution, appropriate signal intensity and linearity between measured intensity and PMT current, 10 kΩ and 3.8 k Ω resistors were connected in parallel to the amplifiers for the OH* and CH* detectors, respectively. The time resolution of each setup was investigated for various resistors by investigating the signal recorded from the input of short square pulses (duration: 1 μs) of an LED. A compromise between time resolution and signal intensity was chosen with selecting a time resolution of 2 μs that matched the time resolution of the optical arrangement. Care was taken not to change the optical configuration during one set of experiments.

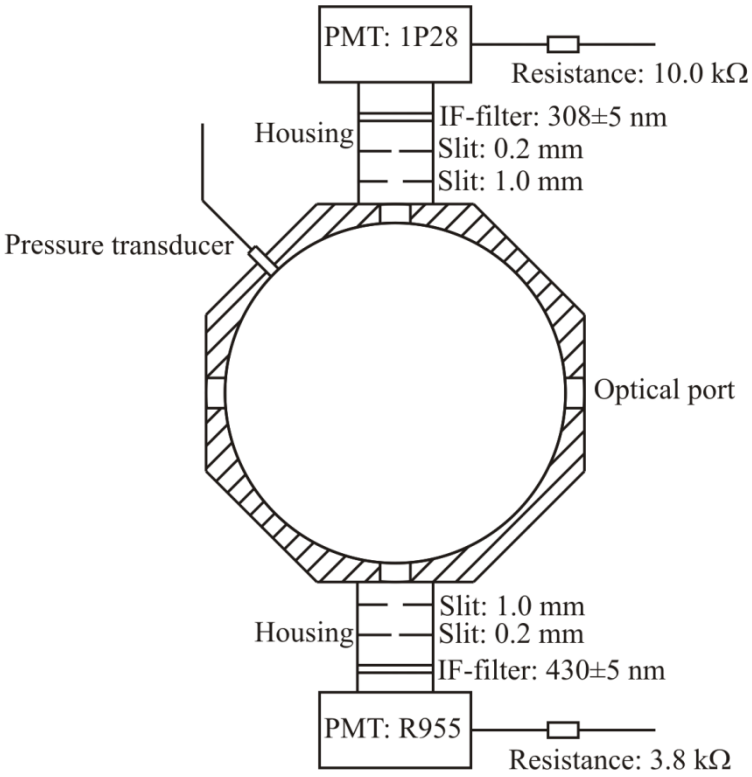

Figure 3.2: Schematics lateral cut of the shock tube II with the two separate OH* and CH* CL detection setups.

3.1.2. Ring-dye laser absorption measurements

Time-resolved ring-dye laser absorption spectroscopic (RDLAS) experiments were carried out in a stainless-steel shock tube (shock tube II) with a constant inner diameter of 80 mm. The driver section has a length of 3.5 m and the driven section has a length of 6.0 m. Again, hydrogen was used as driver gas. The driver section was pumped down to 10^{-2} mbar. Prior to each experiment the driven section was turbo-pumped to final pressures below 1×10^{-7} mbar. The schematic setup of the shock tube is in principle similar to the shock tube shown in Figure 3.1.

The shock speed was measured over three equidistant intervals using four piezo-electric pressure transducers (PCB 113A21) with a time resolution of the data acquisition of 0.1 µs. Additionally, another pressure gauge (PCB 113A21) was placed close to the end-wall (distance: 10 mm). Four optical ports with each two on opposite site were located 10 mm upstream of the end flange and allow to direct the laser beam through the center of the tube with an absorption length equal to the inner diameter of the driven section.

The combination of high spectral resolution of $\Delta\nu / \nu \leq 10^{-8}$, wide spectral tunability (200 – 900 nm) make ring-dye lasers with optional frequency doubling attractive for spectroscopic applications. Their continuous emission with low fluctuation allows for time-resolved absorption measurements. For typical experimental conditions, the linewidth of the laser is 500 kHz

compared to the molecular transitions (10 MHz). Thus, defined transitions can be probed without bandwidth effect. The high sensitivity of the differential laser absorption technique consists of the detection probe and a reference beam allows a fractional absorption of 0.1% which corresponds to a minimum detectivity less than 1 ppm (e. g. OH). Therefore, highly diluted mixtures can be used to separate the reaction of interest by eliminating interfering secondary reactions.

The species concentration can be directly determined from an absorption measurement according to the Beer-Lambert law:

$$\frac{I}{I_0} = \exp\left(-\alpha_\nu l[X]\right). \tag{3.1}$$

The concentration of interest [X] is derived from the transmitted intensity I and the reference intensity I_0 simultaneously monitored by the detection system, the absorption path length l and the absorption coefficient $\alpha_\nu(T, p, \nu)$

3.1.2.1. RDLAS setup in the VIS range

The stability of the laser and the sensitivity of the detection are fundamental requirements for selective absorption measurements. For this purpose, ammonium (NH_3) pyrolysis was chosen for testing the laser stability and the instrumental accuracy. The ring-dye laser absorption spectroscopy (RDLAS) setup for NH_2 absorption (see Figure 3.3) used in the present work consisted of a continuous wave (cw) diode-pumped solid-state (DPSS) laser (Coherent Verdi V10) with a fixed wavelength at 532 nm and a variable output power up to 10 W. The cw laser was used as pump laser for the frequency-stabilized ring dye laser (Coherent CR 699-21). The frequency stabilization ensured single-mode operation and a narrow linewidth of 500 kHz. A small portion of the laser beam was coupled into a reference cavity consisting of a Fabry-Perot interferometer which detects instabilities of the fundamental wavelength. If the laser shows frequency fluctuation, the reference cavity gives a feedback signal and the control unit readjusts the tweeter, the etalons and the Brewster plate in order to lock the fundamental wavelength and to ensure single frequency. Based on this active stabilization, a linewidth of $\Delta\nu < 500$ kHz can be achieved, which is significantly below the typical molecular linewidth of 10 MHz in the visible spectrum. In order to avoid mode-hopping due to mechanical vibrations, the pump laser and the ring dye laser were build up on an active air-suspended breadboard which is placed under a flow box to ensure a dust-free atmosphere.

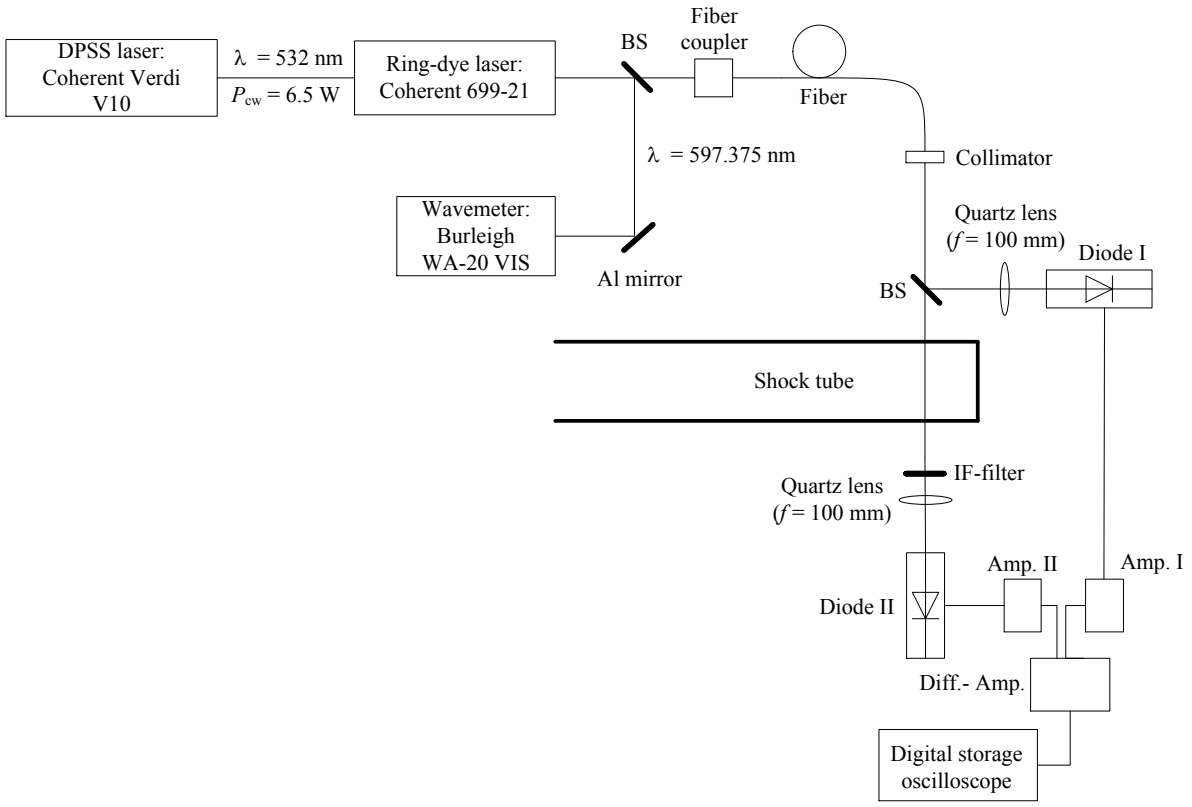

Figure 3.3: Schematics of the RDLAS setup for VIS absorption measurements.

For wavelength determination, a beam splitter coupled a small portion of the output laser beam into a vacuum wavemeter (Burleigh WA-20 VIS) with a stated accuracy of $\Delta\nu / \nu = 10^{-6}$. The laser beam was coupled into an optical fiber (Thorlabs BFH22-200) transferring the laser beam to the shock-tube facility. A collimator (Thorlabs PAF-X-18-PC-A) was used to shape and couple the laser beam into the detection pathway. To increase the sensitivity and to reduce the effect of intensity fluctuations, the detection system was designed with separate probe and reference beams. Half of the output power was directed towards the reference detector and the other half was sent through the shock tube. Two UV-enhanced silica photodiodes (Hamamatsu S1722-02) with a wide spectral bandwidth from 190 to 1100 nm were used to monitor the laser intensity. Quartz lenses were placed in front of the detectors to focus the laser beams onto the active surfaces of the photodiodes. To block emission from the gas mixture, an interference filter with a center wavelength at 600 nm and a bandwidth of 50 nm was placed in front of the probe detector. A high signal-to-noise ratio was achieved by differentially amplifying the probe and the reference signals. The signals were balanced at 6 V, thus, fractional absorption of around 0.1% can be detected. The temporal resolution of the difference amplification was less than 1 μs. Based on the beam diameter of 4 mm and typical shock velocities, a temporal resolution of 4 μs was achieved.

3.1.2.2. Characterization and validation of the RDLAS setup in the VIS range

For the characterization of the RDLAS setup, Ar-diluted NH_3 mixtures were shock-heated to generate defined NH_2 concentrations. Colberg [93] and Friedrichs et al. [94] extensively characterized the above-mentioned NH_2 transition by means of frequency modulation spectroscopy behind shock waves and cavity ring down measurements at room temperature, respectively. Kohse-Höinghaus et al. [95] quantitatively studied the absorption coefficient of NH_2 by means of photolysis and pyrolysis experiments behind reflected shock waves and provided temperature-dependent absorption coefficients. Davidson et al. [96] studied NH_3 pyrolysis by measuring both NH and NH_2 and developed a reaction mechanism for NH_3 pyrolysis. The results of the present work were compared with simulations using the pyrolysis mechanism documented in [96]. The model consists of 21 reactions incorporating 9 species. No modifications were done in the reaction set and their corresponding rate coefficients. In analogy with [95-96], the $A^2A_1 \leftarrow X^2B_1(090 \leftarrow 000)\Sigma^P\ Q_{1,N}(7)$ transition at 16739.90 cm^{-1} was selected in the present work for quantitative evaluation.

In the present work, NH_2 absorption was monitored in shock-heated NH_3/argon mixtures. The absorption of NH_2 was recorded by a difference signal which is subsequently converted into species concentration by fitting the corresponding absorption coefficient with regard to the NH_2 peak concentration. The fitted absorption coefficients were compared with the recommendations for σ_{NH_2} determined by $3.322\times10^{10}/T^3 + 3.130\times10^5/T^2 - 1.302\times10^3/T$ (T in K) from [95]. The measured and the simulated data agree within the stated error limits of ±30%.

Figure 3.4a shows a typical concentration-time history of NH_2 behind the reflected shock wave. The sharp peak at $t = 0$ µs is attributed to the beam deflection caused by the passing of the reflected shock wave (schlieren effect). NH_2 is formed and reaches its peak concentration of 250 ppm within 90 µs. Afterwards, NH_2 is slowly consumed. The simulation was performed using the pyrolysis mechanism from Davidson et al. [96]. There is good agreement between experimental and simulated results in terms of the absolute concentration and the temporal behavior of NH_2. The formation is governed by the reactions (i) $NH_3 + M = NH_2 + H + M$ and (ii) $NH_3 + H = NH_2 + H_2$. In order to demonstrate the sensitivity of the considered model with regard to both reactions, the rate coefficients were changed by a factor of 0.5 and 2. Small changes in the corresponding rate coefficients k_i and k_{ii} lead to significant deviations in the NH_2 peak concentration. Based on a rate-of-production (ROP) analysis (not shown here), the model reveals that the consumption of NH_2 is mainly attributed to the reactions (iii) $NH_2 + H = NH + H_2$, (iv) $NH_2 + NH_2 = NH_3 + H$ and (v) $NH_2 + NH = N_2H_2 + H$. The comparison of the experimental and the simulated NH_2 concentrations for higher temperatures (not shown here) shows that the model can accurately predict the formation behavior and the concentration at peak maximum whereas a slight overprediction of the NH_2 consumption was observed. This fast decay was already reported by Davidson et al. [96] and can be monitored

for temperatures above 2700 K. Due to the high initial concentration of NH_3, subsequent reactions can occur which additionally consume NH_2.

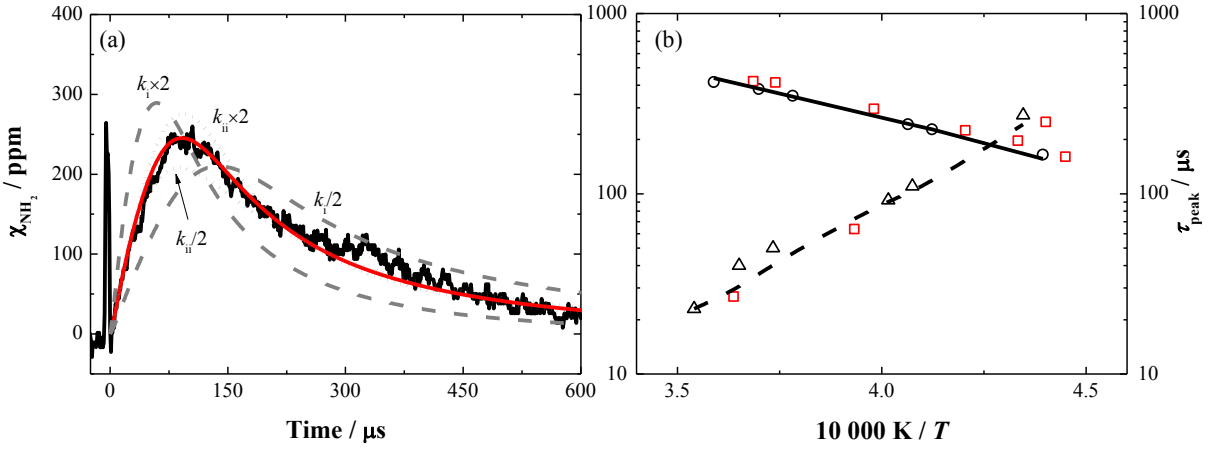

Figure 3.4: (a) Comparison of the experimental (black line) and simulated (red line) time-resolved NH_2 concentration for T_5 = 2490 K and p_5 = 1.64 bar. (b) Comparison of the experimental (symbols) and simulated NH_2 peak concentration (open circles and solid line) and peak times (open triangles and dashed line). Additional experimental results from Davidson et al. [96] (open squares). Mixture composition: 2740 ppm NH_3 in Argon.

The experimental peak times and the peak concentrations of NH_2 from the present work and the corresponding simulations were compared and good agreement was found (see Figure 3.4b). Furthermore, the results from the present work were compared with the results of Davidson et al. [96]. Good consensus is found for both results. These results represent a benchmark test for further investigation of the RDLAS system, in particular in the UV range.

3.1.2.3. RDLAS setup in the UV range

The detection setup for UV is shown in Figure 3.5 and the design is similar to the VIS setup presented above. Instead of a narrow band pass filter, a UV-enhanced narrow-band mirror (Edmund Optics mirror #47-986) with high reflectivity around 308 nm behind the second window of the shock tube in front of the probe photodiode was used for elimination of the background emission.

The frequency doubling of the fundamental wavelength of the ring-dye laser was realized by an external frequency doubling unit (Coherent MBD-200). Typically, straightforward single-pass doubling provides a conversion efficiency of less than 0.01%. The present doubling unit based on resonant enhancement achieves a conversion efficiency of 10% which is several orders of magnitude higher. The fundamental beam enters an enhancement cavity (Fabry-Perot resonator) with highly reflective mirrors. The fringes occurring due to proper alignment of the enhancement cavity have a finesse greater than 200. One of the cavity mirrors is mounted on a piezo actuator and can be driven with a sawtooth function in order to vary the cavity length. In case of instabilities, the electronic control system locks the cavity to the peak

of one of those fringes and therefore, to the maximum intensity of the fundamental power. This enhancement ensures a high conversion efficiency.

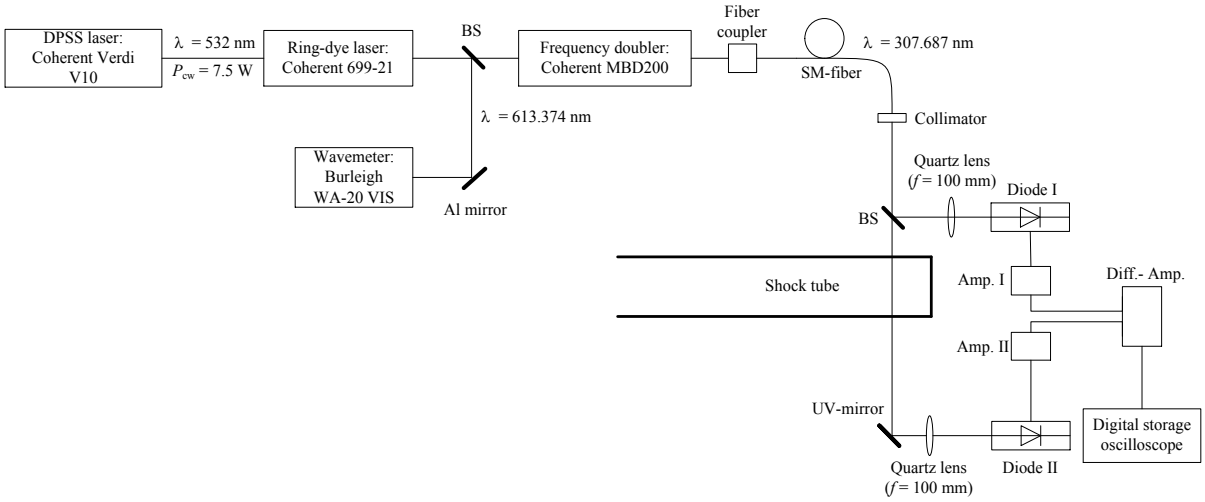

Figure 3.5: Schematics of the RDLAS setup for UV absorption measurements.

OH absorption from the $A^2\Sigma^+ \leftarrow X^2\Pi(0,0)$ transition of the $R_1(5)$ line at 32,606.56 cm^{-1} was studied in the well-known combustion systems of hydrogen and methane under shock-tube conditions. The chosen line is well separated from neighbors and provides strong absorption at high temperatures. Thus, it has been frequently employed for low-pressure shock-tube experiments and was documented elsewhere [97-99]. The absorption coefficient was calculated using the homemade program based on [100]. The impact of the pressure and temperature increase on the absorption cross section due to temperature variation in the shock tube was found to be negligible. The absence of radiation of the test gas was confirmed by conducting experiments without laser illumination.

3.1.2.4. Characterization and validation of the RDLAS setup in the UV range

The ring-dye laser and the frequency doubling setup were characterized with regard to the H_2/O_2 and CH_4/O_2 systems, which are well-described sources of OH to ensure reliable experimental results before investigating the formation of OH in ethanol-based mixtures.

OH radicals were monitored at 306 nm using shock-heated methane and oxygen mixtures. The RDLAS setup is presented in section 3.1.2.1. The entire experimental conditions and the mixture compositions are summarized in Table 3.2. Simulations of the OH concentration both for methane and hydrogen were performed using the GRI3.0 mechanism [27] with respect to the experimental conditions. For the hydrogen experiments, additional calculations were done based on the Warnatz mechanism [21, 29] described in section 2.2.1.

Table 3.2: Mixture composition and experimental conditions of $H_2/O_2/Ar$ and $CH_4/O_2/Ar$ experiments.

Mixture	% CH_4	%H_2	% O_2	% Ar	ϕ	T_5 / K	p_5 / bar
I	0.1	–	0.2	99.7	1.00	2090 – 2725	1.68 – 1.87
II	–	0.2	0.1	99.7	1.00	2075 – 2493	1.78 – 1.84

A typical time-resolved OH-concentration profile in an argon-diluted stoichiometric hydrogen and oxygen mixture is presented in Figure 3.6a. The OH concentration-time history (black line) was compared with two simulations using the mechanisms from Warnatz [21, 29] (red line) and GRI3.0 [27] (green line), respectively. Both mechanisms predict a slightly faster OH concentration rise compared to the experiment, whereas the GRI3.0 mechanism shows a better performance with regard the temporal behavior. The plateau concentration is well reproduced by the Warnatz mechanism within the experimental error [21, 29] implying the high experimental accuracy. Figure 3.6b shows a typical temporal OH-peak concentration profile for a stoichiometric methane and oxygen mixture (black line). The schlieren caused by the passage of the shock wave is indicated as a small peak at $t = 0$ µs. The formation of OH shows an induction time of 125 µs and forms a plateau at 250 µs. OH is slowly consumed at longer reaction times. The simulation of OH based on the GRI3.0 mechanism [27] (green line) predict well the temporal behavior in terms of induction and rise time for the presented conditions. However, the predicted plateau concentration is lower than in the experiment. Depending on the experimental conditions the differences in the peak values can reach up to 20%. In general, one has to point out that the underlying mechanism systematically underpredicts the induction time and the peak concentration of OH within the entire experimental conditions especially for stoichiometric conditions. These observations were also reported in [27] where deviations in the predicted time to half OH maximum and in the peak concentration were reported. OH concentrations were measured under shock-tube conditions by Chang et al. [101], their experiments were conducted under similar conditions with regard to the present work. The comparison of these experiments with the simulations performed with the GRI3.0 mechanism show a significant underestimation of the OH peak concentration of up to 15%. Special care was taken to determine the uncertainties that arise from errors in the absorption cross-section which was found to be negligible. Recently, Herbon et al. [99] remeasured the heat of formation of OH which was identified as a reason for the deviations in the OH plateau concentration shown above. An elimination of experimental error was reported when using their recommendation in [99].

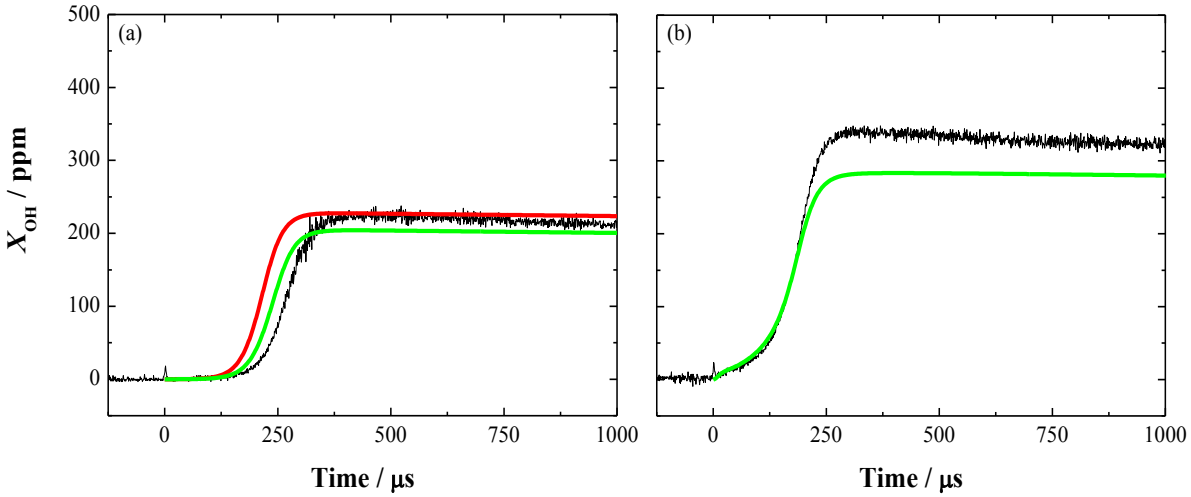

Figure 3.6: Typical experimental (black line) and simulated (colored lines) temporal OH concentration-time history behind the reflected shock wave. (a) Mixture II at T_5 = 2075 K and p_5 = 1.84 bar and (b) mixture I at T_5 = 2201 K and p_5 = 1.76 bar.

3.2. Shock-tube facility for the validation of reaction mechanism at percent-level concentrations

Unlike laser spectroscopic methods, the validation of complex reaction mechanisms using mass spectrometry requires relatively high initial concentrations of the corresponding species which is attributed to the lower sensitivity of the detection system. Therefore, initial concentrations of 5,000 ppm and more are required to measure time-resolved concentration profiles of multiple species with a tolerable signal quality. Compared to optical diagnostics with a concentration sensitivity in the range of 10^{-13} mol cm^{-3} for two-atomic molecules and a time resolution of less than 1 µs, mass spectrometry can only resolve concentrations in the range of 10^{-10} mol cm^{-3} with a reduced time resolution of 10 µs.

3.2.1. Time-of-flight mass spectrometry

The advantage of optical diagnostics is the potentially high selectivity and sensitivity. However, the detection is typically limited to one or two species with small molecular size at the same time and therefore, is not always sufficient for the development of complex reaction mechanisms. A high-repetition-rate time-of-flight mass-spectrometer (HRR-TOF-MS) coupled with a conventional shock tube (shock tube III) was used to study ethanol pyrolysis and oxidation. The combination of shock tube and mass spectrometry has the advantage to simultaneously detect multiple species in real-time. A detailed description of the shock tube and the TOF-MS with the corresponding modular sampling unit is given by Dürrstein et al. [102]. Therefore, only a brief introduction of the shock-tube facility is given.

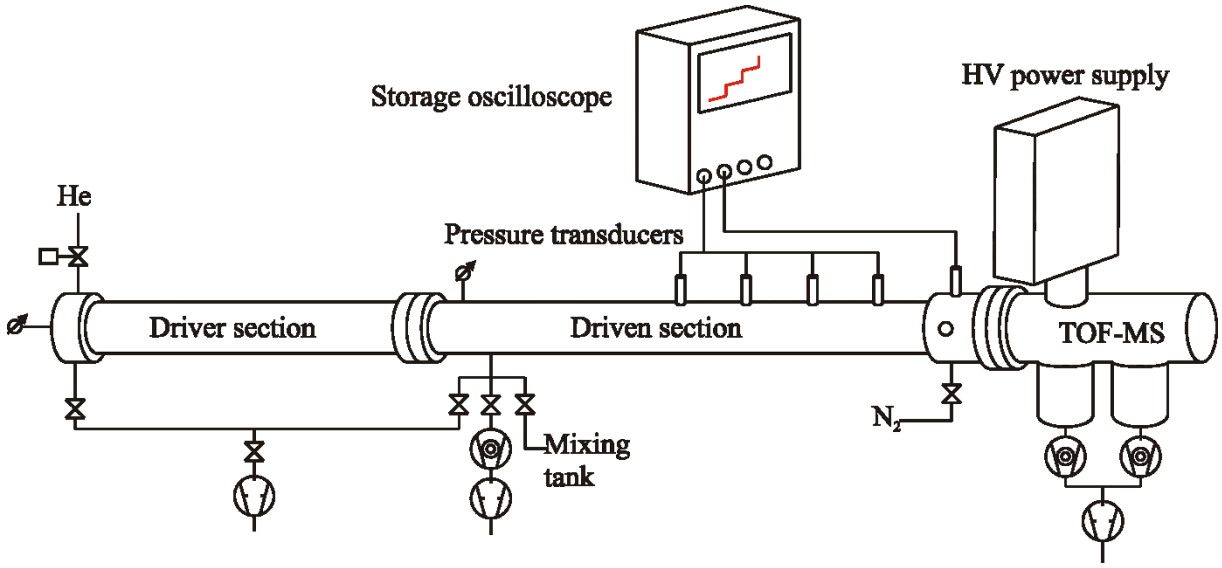

Figure 3.7: Schematics of shock tube III with time-of-flight mass spectrometry.

The experiments were conducted in a conventional stainless steel diaphragm-type shock tube. A schematics of the shock-tube facility is shown in Figure 3.7. The driver and the driven section have a constant inner diameter of 80 mm. The driver section has a length of 2.5 m and the driven section has a length of 6.3 m. The setup is devoted to investigations in the field of combustion research as well as to studying the kinetics of reaction systems relevant to nanoparticle formation from the gas phase using metal-organic substances. Hence, to avoid condensation in the shock tube due to low vapor pressures of the substances, the driver and the driven section and the mixing vessel are temperature-controlled and can be heated up to 150 °C. Both shock-tube sections can be evacuated with a dry vacuum pump (Edwards Drystar QDP 80) which enables pumping the tube down to 5×10^{-4} mbar. This pump was also used for pumping the mixing vessel of the shock tube using a bypass line. Aluminum sheets with a thickness in the range of 50 – 90 µm were used as diaphragms. Helium was used as driver gas. The shock tube is equipped with an equidistant set of four pressure transducers (PCB model 112A05) with a distance of 150 mm between the transducer centers. The last transducer of this set is located in a distance of 150 mm from the end plate of the driven section. A fifth pressure transducer located close to the end plate is used to measure the post reflected-shock pressure. The signals of all pressure transducers are amplified with charge amplifiers (Kistler Kiag Swiss 5001) and detected by an oscilloscope to determine the shock wave velocity using the standard approach [103].

A home-made modular sampling unit consisting of a nozzle (diameter 30 – 300 µm) in the end wall is permanently mounted and separates the driven section of the shock tube from the TOF-MS. Additionally, a skimmer can be placed downstream of the nozzle to form a molecular beam which then enters the TOF-MS and enters the ionization chamber.

For fast kinetics studies, the TOF-MS must be operated at high repetition rates. Therefore, the HRR-TOF-MS (Kaesdorf) was designed for repetition rates up to 150 kHz by combining a compact design (short flight distance) with high transmission energies (high flight velocities). This avoids the overlap of signals caused by ions from consecutive ionization cycles. Typically, repetition rates of approximately 100 kHz are used and there is no overlap of consecutive spectra up to masses up to 170 u. The present mass spectrometer is an advantageous compared to the facility described by Tranter et al. [104] that shows overlap of successive spectra at a repetition rate of 105 kHz. The TOF-MS is equipped with an electron impact ion source with two-stage ion extraction. A two-stage reflectron compensates for differences in flight time due to different initial energies of the ions up to a second-order correction of approximately 8 – 10% of the ensemble mean energy. The energy of the ionizing electrons can be tuned from 5 to 85 eV. The ionization energy was set to 45 eV to reach a tradeoff between signal intensities and minimization of fragmentation due to the electron bombardment. It is possible to ionize under field-free conditions as ionization and extraction can be pulsed independently. The maximum kinetics energy of the ions is 10 keV which is high enough to generate detectable signals for molecular weights up to 1,000 u. The HRR-TOF-MS is equipped with two micro-channel plate (MCP) detectors: one that is used in the reflectron mode and one that can be used in the linear TOF-mode. To eliminate the influence of chemically ionized species from the shock tube, a positively charged lens shields the ion source against the shock tube.

4. Results and discussion

4.1. Shock-tube measurements of OH* chemiluminescence

The major emission band of OH* chemiluminescence is attributed to the reaction-induced population of the OH(A) state . Aside from the strong A–X transition at 306 nm, much weaker emission from OH(B) and OH(C) states are accessible. However, these bands are very weak in flames and could not be identified yet. Therefore, all studies consider the strong A–X transition.

4.1.1. Review of OH* kinetics

Formation of OH* chemiluminescence in hydrogen combustion was first reported by Kaskan [105] and was widely studied since [49, 106-107]. Several potential reactions in hydrogen combustion have been suggested to be responsible for OH* formation. Kaskan [105] studied the UV emission of OH* in rich $H_2/O_2/N_2$ flames and found a proportionality of OH* with the cube of the ground-state OH concentration. Based on this finding, he postulated the reactions H + O + M = OH* + M as well as H + OH + OH = OH* + H_2O to be responsible for OH* chemiluminescence. Marques et al. [108], amongst others, studied the OH* formation in spark-ignited C_2H_2/O_2 mixtures in a closed chamber. Based on a comparison of their measured time-resolved emission profiles with computed normalized concentration profiles, they suggested H + O_2 = OH* + O as the main channel forming 90% of the OH*. More recently, Skrebkov et al. [109] analyzed the OH* formation channel by *ab initio* calculations and proposed the reaction H_2 + HO_2 = OH* + H_2O to be the main OH* formation pathway.

While different reaction pathways of the OH* formation were suggested, early and recent studies predominantly agree in identifying the three-body reaction (R1) as the main formation reaction in hydrogen combustion. This was first proposed by Gaydon [48] and Charton and Gaydon [110]:

$$H + O + M = OH^* + M \qquad (R1)$$

Based on flame experiments in various $H_2/O_2/N_2$ mixtures measuring OH* emission intensities, Kaskan [105] studied the formation of OH* chemiluminescence and recommended a rate coefficient for the above-mentioned reaction. Koike and Morinaga [66] provided the rate coefficient of reaction (R1) by correlating the emission intensity at various temperatures and calculated OH* concentrations. Similarly, Hidaka and co-workers [111] identified reaction (R1) as the main source of OH* from shock-tube experiments with diluted H_2/O_2/Ar mixtures and derived a reaction rate coefficient of 1.2×10^{13} exp(−29 kJ mol^{-1}/RT) cm^{6}mol^{-2}s^{-1}. Among

recent studies, Smith et al. [112] examined rich hydrogen/air premixed flames. Based on simulated and experimental OH* number densities, they recommended the rate coefficient of the reaction (R1) to be 5.5×10^{12} $cm^6mol^{-2}s^{-1}$. Petersen and co-workers [113] applied a calibration procedure to convert measured OH* chemiluminescence intensities into absolute species concentrations by relating the measured PMT voltage with the corresponding simulated OH* concentrations. The OH* kinetics were optimized based on ignition delay times and concentration time histories of OH* chemiluminescence. Later on, Hall and Petersen [78] derived a rate coefficient for (R1) to be 3.1×10^{14} $\exp(-41.8\text{ kJ mol}^{-1}/RT)$ $cm^6mol^{-2}s^{-1}$ based on a shock-tube study. This was done by fitting the temperature dependence of the OH* peak intensity in various H_2/O_2 mixtures. In all these studies, the recommended rate coefficient varies by two orders of magnitude from each other.

While OH* chemiluminescence is weak in hydrogen oxidation, it is strong in hydrocarbon combustion. OH* chemiluminescence in hydrocarbon combustion has been studied by several groups [55, 114-116]. There is accordance in the identified key reaction that leads to OH* emission to be:

$$CH + O_2 = OH^* + CO \qquad (R2)$$

Some early work on OH* chemiluminescence in hydrocarbon combustion was done by Porter et al. [114]. Based on the correlation of CH, O_2 and OH* profiles in various acetylene and methane flames, they suggested reaction (R2) to be responsible for the OH* formation and recommended a rate coefficient $k_2 = 6.0\times10^{10}$ $cm^3mol^{-1}s^{-1}$. Grebe and Homann [55] measured time-resolved OH* concentration profiles in a low-pressure discharge flow system with reactive C_2H_2/O/H mixtures at room temperature. Based on this study, they derived a rate coefficient of 4.8×10^{10} $cm^3mol^{-1}s^{-1}$. More recently, Carl et al. [117] showed that there is a proportionality between OH* formation and the product of CH and O_2 concentrations by molecular-beam-sampling threshold-ionization mass spectrometry (MB-TIMS). Based on this observation, they deduced that reaction (R2) is responsible for OH* emission and recommended a rate coefficient of $k_2 = 4.8\times10^{10}$ $cm^3mol^{-1}s^{-1}$ in a temperature range of 298 and 511 K. Smith et al. [51] measured absolute OH* and CH* concentrations in laminar premixed CH_4/air flames with different equivalence ratios. They calibrated their spatially-resolved and Abel-inversed images by Rayleigh scattering with respect to computed excited-state species concentrations and determined a rate coefficient $k_2 = 1.8\times10^{11}$ $cm^3mol^{-1}s^{-1}$. Hall and Petersen [78] performed a series of shock-tube experiments with H_2/O_2 and $H_2/O_2/CH_4$ mixtures. By fitting their computed results with regard to their experimental observations, they also identified reaction (R2) as the main channel with a temperature-dependent value for k_2 of 3.2×10^{14} $T^{-0.4}$ $\exp(-17.4\text{ kJ mol}^{-1}/RT)$ $cm^3mol^{-1}s^{-1}$. Recently, Kathrotia et al. [65] studied OH* chemiluminescence in premixed low-pressure flames for various methane-based mixtures. Based on their flame calculations, they supported reaction (R2) to be responsible for

OH* CL using the rate coefficient from Smith et al. [51]. There is accordance in literature on the determined k_2 to be in the range of 4×10^{10} and 1.8×10^{11} $cm^3mol^{-1}s^{-1}$.

OH* is short lived and returns to the ground state via two channels. In the first channel, it emits its excess energy in the form of light in a radiative decay reaction (R3) OH* = OH + *hv*. The rate coefficient of this reaction has been proposed by several authors [48, 111, 118]. The second channel is the non-reactive collisional quenching reaction OH* + M = OH + M (R4). Here, the excess energy of OH* is transferred to the collision partner M. The effect of various collision partners has been studied at various temperatures ranging from room temperature to flame temperature by several authors. Becker et al. [119] provided quenching rate coefficients for M = H_2, H, and Ar at room temperature. Fluorescence excitation by a dye laser was applied to measure the OH* lifetime in presence of H_2, H, and Ar. Fairchild et al. [120] measured thermally-averaged collisional quenching with H_2O, O_2, and H_2 by laser-induced fluorescence (LIF) at about 1100 K. OH* quenching with H_2O and atomic H was studied by Jeffries et al. [121] in low-pressure stoichiometric $H_2/O_2/N_2O$ flames also using LIF. Recently, Bailey et al. [122] investigated the temperature dependence of OH* quenching for collision partners such as N_2 and O_2 at room temperature. Hemming et al. [123-124] studied the influence of N_2, O_2, and H_2 at and below room temperature. Heard and Henderson [125] determined the OH* quenching rate coefficient with H_2 at low temperatures (200 – 344 K) in a flash-photolysis system. All these quenching rate coefficient data are in good agreement with each other from room to flame temperature. For collision partners such as H, O, and OH, limited information is available due to the complexity of the measurement. The compilation of data for major collision partners is given by Tamura et al. [68] and recommendations are made for the 300 – 2500 K range. Depending on temperature, these coefficients differ by up to three orders of magnitude.

4.1.2. Strategy of investigating OH* chemiluminescence

In the present study, OH* formation was investigated in various shock-heated hydrogen and hydrocarbon mixtures. By using a calibration approach, which will be presented in detail in section 4.1.3, the corresponding OH* production pathway in hydrogen oxidation was identified and was subsequently applied for the investigation of OH* chemiluminescence in hydrocarbon combustion systems. A discussion of the results for hydrocarbon combustion will be given in sections 4.1.4 – 4.1.8.

Due to the well-known hydrogen ground-state chemistry, the present work started with a systematic investigation of OH* chemiluminescence based on hydrogen oxidation [79]. Established mechanisms for hydrogen oxidation (see section 2.2.1) were used. In order to link the light emission of OH* and the corresponding species concentration, a calibration approach was derived based on thermal excitation of ground-state OH radicals at high temperatures

(around 3000 K). The determined calibration factor was then transferred to describe the chemical activation via (R2). In this manner, a model-based calibration procedure was developed to quantify the OH* concentrations and measure the rate coefficient of the underlying reaction.

Based on the calibration approach, the OH* formation reaction in hydrocarbon oxidation was characterized. Due to the increasing complexity of hydrocarbon combustion with increasing chain length, OH* chemiluminescence was initially studied in methane systems. Akin to hydrogen combustion, the oxidation of CH_4 is well-known and has been extensively studied in the past. The ground-state chemistry is accurately modeled using the GRI3.0 mechanism (see section 2.2.2) which was widely validated. For this purpose, the OH* kinetics model adopted from the hydrogen study was extended for the oxidation of methane. Subsequently, the OH* model was validated with regard to more complex hydrocarbons (C_2H_2, C_2H_4 and C_2H_5OH).

In order to extend the validation database of the OH* sub-mechanism from the present work, the model was compared to flame calculations from literature. For this purpose, additional simulations were done according to recent studies dealing with OH* formation in various premixed flames [51, 63, 65].

4.1.3. OH* chemiluminescence in H_2/O_2/Ar systems

Four series of shock-tube experiments with various hydrogen mixtures were conducted. OH* chemiluminescence was observed in a wide temperature range around atmospheric pressures (see Table 4.1). Because the measured OH* intensities cannot be directly related to the corresponding species concentrations, a high-temperature calibration approach was derived for the conversion of the signal into absolute concentrations. Based on this approach, the chemical excitation pathway for temperatures below 2800 K was studied by combining the shock-tube data with numerical modeling.

Table 4.1: Mixture compositions, temperature and pressure ranges of the shock-tube experiments.

Mixture	ϕ	Composition	T_5 / K	p_5 / bar
A	0.5	1% H_2 + 1% O_2 in Ar	1400 – 3300	0.85 – 1.50
B	1.0	2% H_2 + 1% O_2 in Ar	1440 – 3180	0.90 – 1.40
C	0.5	1% H_2 + 1% O_2 + 5% N_2 in Ar	1400 – 3200	0.90 – 1.40
D	1.0	2% H_2 + 1% O_2 + 5% N_2 in Ar	1450 – 3200	0.90 – 1.45

Thermal excitation of ground-state OH radicals was early reported in [66, 111]. Furthermore, in a recent opposed flow methane oxy-flame De Leo and co-workers [67] attributed more than 35% of the OH* formation in the thermal equilibrium due to the high temperatures that went up to 3000 K. For calibration purpose, three important aspects have to be clarified before rely-

ing on this strategy. (i) The approach of using thermal excitation of ground-state OH molecules in order to generate defined OH* concentrations and correlating them with the corresponding light emission requires an accurate prediction of the absolute OH concentration at the present experimental conditions. (ii) Additional reactions (for example collisional induced decomposition of OH*) must have a negligible effect. (iii) It must be clarified that the measured peak intensity does not suffer from insufficient temporal resolution of the detectors (thus, reduced sensitivity due to the convolution with the signal transfer function). (iv) The influence of emission trapping due to ground-state OH must be considered and estimated.

(i) The underlying ground-state mechanism was used to predict the thermal excitation of OH towards OH*. Thus, the OH* concentration depends directly on the computed OH concentrations. In order to relate experimental and simulated absolute OH concentrations at elevated temperatures, additional RDLAS experiments in a stoichiometric $H_2/O_2/Ar$ mixture were performed and the agreement of measured and computed OH concentration was demonstrated (accuracy ±3%) in section 3.1.2.4. Thus, the predicted OH* concentrations depend mainly on the accuracy of the excitation reactions (–R4) OH + M = OH* + M which are stated with an error up to 15% [68].

(ii) Figure 4.1 exemplarily shows the normalized sensitivity analysis of OH* formation at 3000 K for mixture A. For temperatures above 2800 K, the OH* formation is overwhelmed by thermal excitation via the reverse reaction (–R4) OH* + M = OH + M whereas the contribution of chemical excitation (R1) is found to be negligible. A reaction flow analysis revealed that the contribution of OH* formation is attributed to the collisions with M = H_2O (37%) + OH (23%) + Ar (16%) + O_2 (10%) + H_2 (5%) + H (4%). In comparison, the reverse of the chemical excitation reaction (–R1) contributes about to 5% to the OH* peak concentration only. Therefore, one can neglect the contribution of reaction (–R1) at our calibration conditions.

(iii) The time resolution of the experiment is on one hand determined by the passage of the shock wave associated with the observed solid angle and on the other hand to the electronic responses of the PMT system. Both values are in the range of 1 µs which is short enough to be considered as not influencing the signal traces.

(iv) Signal emitted from OH* chemiluminescence detected at ~307 nm is partially trapped by ground-state OH which is homogenously present in the reaction mixture. A simple analytical approach was used to quantify signal trapping for the experimental conditions that accounts for the homogeneous luminous and homogeneously absorbing gas mixture within the shock tube for all the mixtures used in this study. To quantify signal trapping two OH lines $R_1(7)$ and $R_1(11)$ for the R-branch bandhead of the OH A–X (0,0) band were investigated. For both lines, the peak maximum leads to a reduction in the detected OH* signal by ~10%. For all measured conditions the calculated attenua-

tion was almost constant. For the calibration condition, the higher OH concentration that is related to the higher temperature is compensated by lower absorption cross sections, also resulting in an overall ~10% signal trapping at the peak maxima. Therefore, the signal trapping effect is covered by the calibration. The error of the calibration caused by signal trapping due to slight variations between calibration and measurement and due to variations in the time profile is estimated to be in the ±3% range.

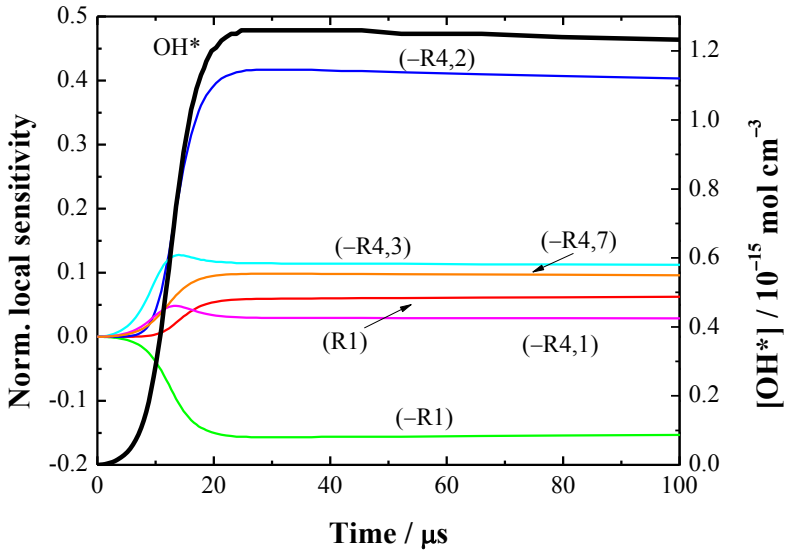

Figure 4.1: Sensitivity analysis of the OH* formation and destruction at T_5 = 3000 K and p_5 = 1 bar for mixture A showing the dominance of the thermal excitation through reaction (–R4).

Taking this into account and by knowing that the OH* chemiluminescence formation is overwhelmed by thermal excitation (–R4) for $T > 2800$ K, a calibration factor was obtained by relating the peak OH* intensity measured to the peak OH* concentration at data points above 3000 K. The calibration procedure was performed for four mixture conditions with 19 data points and an average value was taken. On this basis, a calibration factor of 2.62×10^{-18} $cm^3mol^{-1}mV^{-1}$ was determined. The calibration was then used to interpret the measured chemiluminescence intensities throughout the full temperature range of our experiments. This allows quantitative comparison of measured intensities that are attributed to the formation paths (R1) H + O + M = OH* + M and (R4) at temperatures lower than 2800 K and the calculated concentrations throughout the temperature range of interest.

A typical temporal variation of the OH* concentration for a lean $H_2/O_2/Ar$ mixture consists of an initial rapid formation of OH* from reaction (R1) followed by slow depletion mainly due to the radiative decay (R3) and collisional quenching by reaction (R4) (see Figure 4.2a). The simulated profile is well reproduced when compared to the experiment. The measured absolute concentrations based on the calibration method described before were well-reproduced by the model throughout the wide range of experimental conditions.

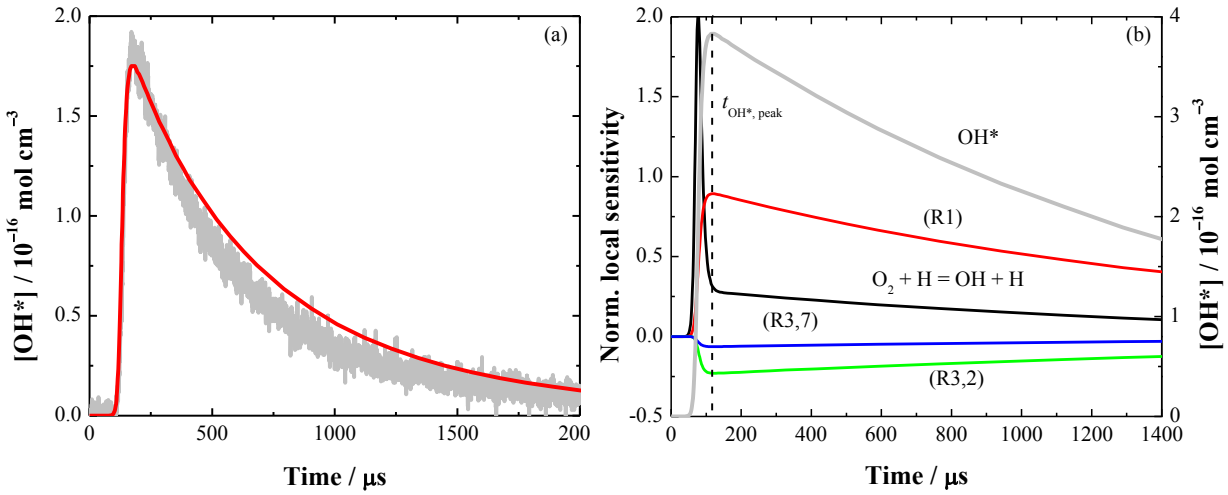

Figure 4.2: (a) Comparison of the temporal variation of the measured and simulated OH* chemiluminescence concentration for mixture A at T_5 = 1592 K and p_5 = 1.27 bar. (b) Normalized sensitivity analysis with respect to OH* over reaction time for mixture A at 1900 K and 1 bar. Only the main quenching reactions are shown for clarity.

As shown in Figure 4.2b which present the normalized local sensitivity coefficients over the reaction time for $\phi = 0.5$, the rise in OH* concentration in the induction phase is determined by ground-state chemistry. During the rise in [OH*] the chain branching reaction H + O_2 = OH + O has the maximum sensitivity. However, when the OH* concentration reaches its maximum, the most influential reaction is (R1). The reaction H + OH + OH = OH* + H_2O has 10 times reduced sensitivity compared to (R1). In addition, the maximum sensitivity of the quenching reactions (M = H_2O) at the OH* peak is only 26%. Thus, the maximum OH* concentration is mostly determined by the rate coefficient of reaction (R1). Therefore, the peak height was used to obtain the rate coefficient of the reaction (k_1) by accounting for the quenching reactions using kinetics data from the literature.

Figure 4.3 shows the temperature dependence of the OH* signal and simulations for all the mixtures studied. The dual-stage formation behavior of OH* CL is clearly observed for all mixture compositions. For temperatures above 2800 K where thermal excitation is the main formation channel of OH*, there is a sharp increase in the OH* concentration as a function of temperature. On the other hand, for temperatures below 2800 K where chemical excitation is the dominating formation pathway of OH*, the OH* peak concentrations show a very weak temperature dependence. Overall, the OH* concentration from thermal excitation relevant for temperatures above 2800 K is more than one order of magnitude higher than for chemical excitation.

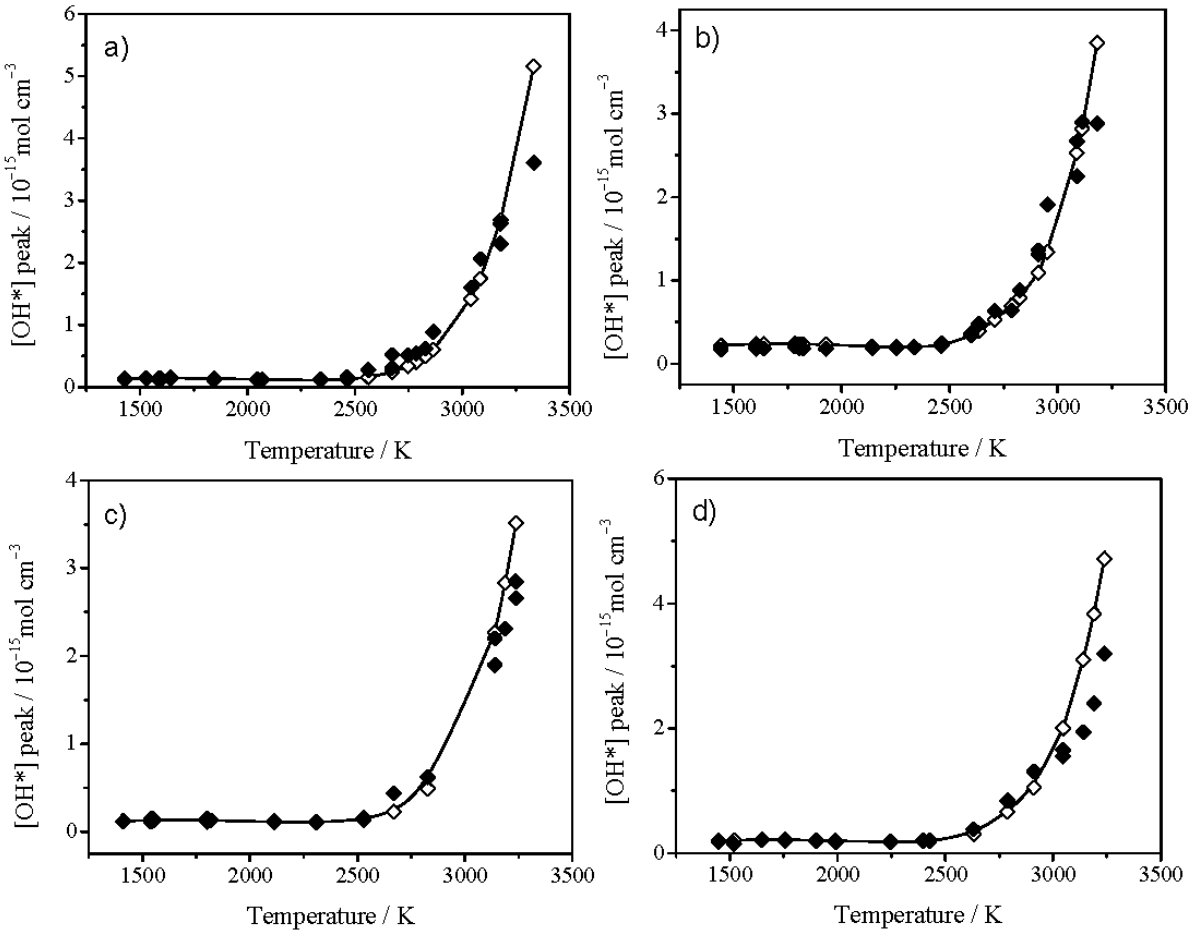

Figure 4.3: Measured and simulated peak OH* concentration as function of temperature for (a) mixture A, (b) mixture B, (c) mixture C, (d) mixture D. Closed symbols represent experimental data. Open symbols with lines represent the simulations at corresponding experimental points with the rate coefficient k_1 of reaction (R1) from the present work.

The OH* concentrations predicted using various k_1 values were compared to the measured converted concentrations at different temperatures. In the first stage of data evaluation, the reaction rate coefficient k_1 was varied by taking values from literature [66, 111-112]. Later, to obtain better agreement with the experiments, the reaction rate coefficient k_1 was varied by keeping values of either A or E fixed. A rate coefficient equal to 1.5×10^{13} $cm^6mol^{-2}s^{-1}$ with an activation energy of 25 kJ mol^{-1} was found to give the best representation of the experimental data. As seen in Figure 4.3, the experimentally obtained peak concentrations vary almost linearly with temperature within the 1400 – 2600 K range. The temperature dependence of all four mixtures is very well reproduced by the simulations in the entire temperature range. As shown in Figure 4.3 at lower temperatures, where the agreement between the experimental values and simulation are not clearly seen on this scale, the calculated OH* concentration is within 10% compared to the measured value.

The various rate coefficients for k_1 from different references are shown in an Arrhenius plot in Figure 4.4. Our rate coefficient is slightly higher than the rate coefficient suggested by Hidaka et al. [111] and lower than others. The plot also shows data from literature, experimental

measurements of k_1 over the temperature range of 1000 – 2000 K. The highest rate coefficient from [78] and the lowest one (Hidaka et al. [111]) differ by two orders of magnitude. The determination of rate coefficients is affected by the uncertainty of the kinetics model in addition to the measurement errors described previously. The calibration of the OH* measurements is based on predicting the concentrations of the intermediates such as H and O atoms from which OH* is formed. The uncertainty of the different kinetics models is reported to be below 20% [126]. Uncertainties of the ground-state precursors of OH* impact the prediction of OH* and, therefore, affect the determination of k_1. As an example, a change in the rate coefficient of reaction H + O_2 = OH + O by $\Delta \log k = \pm 0.2$ (maximum recommended limit in [30]) altered the OH* peak concentrations by ±10% in a lean H_2/O_2/(98%) Ar mixture at 1200 K and 1.4 bar. Although this uncertainty would not affect the temperature dependence corresponding to the activation energy E_a, it would influence the determination of the pre-exponential factor which is adjusted to achieve the best fit with the measurements to obtain k_1. The recommended reaction rate coefficient k_1 in the present work was further tested against shock-tube measurements of the ignition delay based on OH* and will be discussed below.

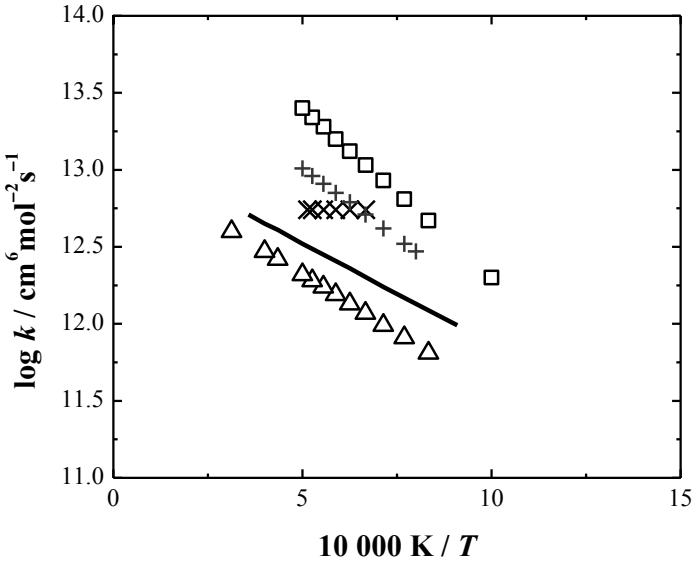

Figure 4.4: Arrhenius plot for the reaction H + O + M forming OH* (R1). Symbols: + Koike et al. [66]; Δ Hidaka et al. [111]; × Smith et al. [112]; □ Hall et al. [78]; — present work.

The uncertainty in the rate coefficient k_1 can be divided into systematic and statistical contributions. The determination of k_1 depends on the absolute OH* concentrations and thus on the calibration factor. An evaluation showed that any error in the calibration factor affects the resulting k_1 values by the same magnitude. The ±20% error in the calibration strategy, therefore, leads to a systematic error in k_1 of ±20%. Additional systematic errors can be connected to the quenching rate coefficients. The quenching rate with argon as a main collider has a small effect on the prediction of the OH* concentrations, while the uncertainty in the quenching cross section of H_2O causes an additional systematic error of 3% on k_1. This value was obtained by varying k_3 (for M = H_2O) within the ±8% uncertainty of the quenching cross sec-

tion stated by Cattolica and Mataga [127]. In the data analysis, each individual experiment leads directly to the determination of a k_1 value. A statistical error of ±15% (1–σ) was derived from the scatter in k_1 results that are evaluated from the total of 20 individual measurements at different temperatures and mixture compositions. The influence of the 5 – 15 K uncertainty in the determination of the gas temperature was considered and it was found to be negligible compared to the other uncertainties. The errors are combined as the square root of the sum, including all of the uncertainties in the determination of the k_1 values. The overall uncertainty in k_1 could be as high as ±30%.

A homogeneous reactor model (0-D) allows the simulation of time-dependent processes in a homogenous reaction system that reproduces the induction time and the temporal variation of chemiluminescence signals in a shock tube [128]. In order to validate the mechanism of OH* formation discussed in the present work in hydrogen combustion, a well established procedure of comparing simulated and experimentally determined ignition delay time is performed. In the present work the ignition delay time τ corresponds to the time when the tangent to the maximum slope of the OH* concentration profile intersects the time axis. Clearly, the ignition delay times is governed by the kinetics of the ground state chemistry and does not depend on (R1). The most sensitive reactions affecting the ignition delay times were the chain branching reactions $O_2 + H = OH + O$ and $H_2 + O = OH + O$. However, when reaction pathways other than (R1) that lead to OH* are considered, no consensus between simulation and experiment is observed in terms of ignition delay times. Therefore, the ignition delay time measurements will serve mainly as an additional check for the ground-state chemistry.

Calculations of ignition delay times are performed for the given set of experimental conditions for H_2/O_2 mixtures diluted in argon and nitrogen. The experimental data correspond to lean ($\phi = 0.5$) and stoichiometric conditions. In our experiments the reflected shock temperature T_5 ranges from 1100 – 3000 K with pressure p_5 ranging from 0.85 to 1.40 bar. Although few literature data can be found for these experimental conditions, comparable ignition delay time measurements can be found in Skrebkov et al. [129]. They investigated the ignition delay times of various highly diluted, stoichiometric hydrogen/oxygen mixtures in a shock tube within a comparable pressure range. One of their mixtures, namely 0.93% O_2 + 1.87% H_2 in Ar, is quite comparable to the measurements presented in this paper. The measurements in [129] cover a wider pressure range (0.5 bar < p_5 < 1.7 bar) than the measurement presented here.

Figure 4.5 shows the comparison of simulated and experimental ignition delay times at the above-mentioned conditions. The simulated ignition times are in very good agreement with the measurements at corresponding conditions. The ignition delay times obtained from Ar-diluted and Ar + N_2-diluted mixtures are very close to each other. The activation energy of the experimental and simulated data matches very well.

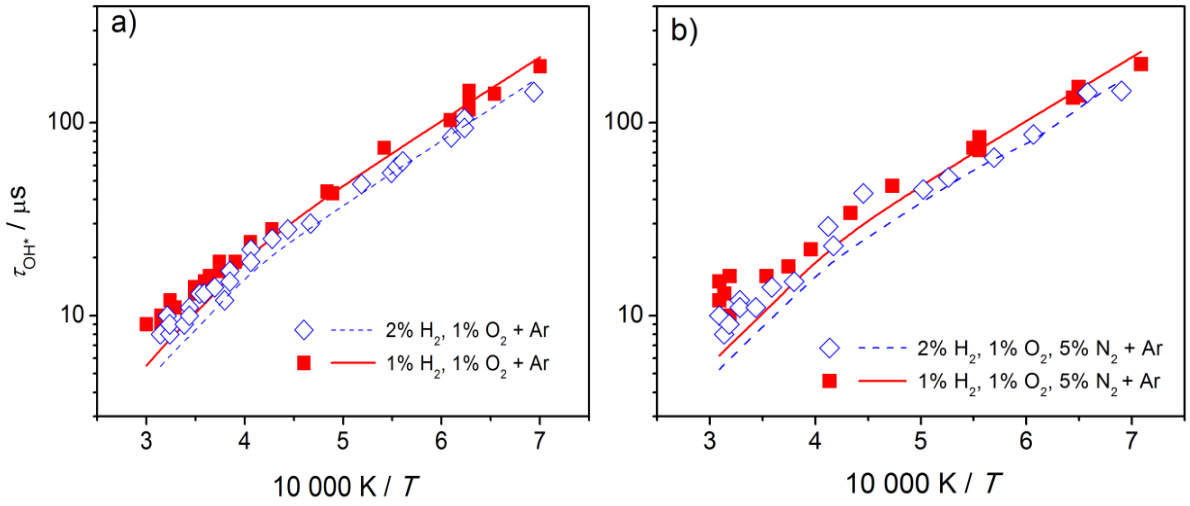

Figure 4.5: Ignition delay time with respect to [OH*] for stoichiometric and lean H_2/O_2 mixtures with (a) Ar dilution and (b) Ar + N_2 dilution. Symbols: shock-tube experiments from the present work, lines: simulations for the experimental conditions [79].

As discussed earlier, the peak concentrations of OH* are a function of the OH* formation reaction (R1) whereas the ignition delay time depends on the ground state chemistry. It is then assumed that the selection of the rate coefficient of reaction (R1) has no influence on the calculation of ignition delay. However, we have observed that the choice of the formation reaction of OH*, other than (R1), may result in differences between the simulated [OH*] compared to the OH* signal variation that is used to derive τ. For example, formation of OH* from reaction $H_2 + HO_2 = OH^* + H_2O$ [109] was discussed earlier in this thesis. We incorporated this reaction in the mechanism along with reaction (R1). Figure 4.6a shows the OH* concentration profile with and without the above mentioned reaction incorporated in the calculation along with the reaction (R1) at three different temperatures for $\phi = 0.5$. Implementing reaction $H_2 + HO_2 = OH^* + H_2O$ with reaction (R1) in the OH* sub-scheme forms a dual peak in the OH* profile. The first peak results from the reaction $H_2 + HO_2 = OH^* + H_2O$ and the second peak is caused by reaction (R1). OH* resulting from reaction $H_2 + HO_2 = OH^* + H_2O$ is formed in the induction phase where H_2 and HO_2 concentrations are high. At temperatures below 1600 K, the recombination reaction (R1) is dominant. However, the first peak is prominent at temperatures above 1600 K which is also true at stoichiometric and fuel-rich conditions. With the reaction $H_2 + HO_2 = OH^* + H_2O$ included in the mechanism (shown in Figure 4.6b), above 1600 K the simulated ignition delay times (obtained at the first rise in OH* profile) were much shorter than the measured ones. In [130] dual peaks in the measured

OH* emission were observed in only three experiments. In addition, the geometric mean of the two calculated OH* maxima of the dual peaks in [130], similar to that depicted in Figure 4.5 (open squares), were compared with the measurements. In the present work, no dual peaks were observed in the measured emission profiles. Thus, this result supports the fact that reaction (R1) is a dominant source for OH* formation.

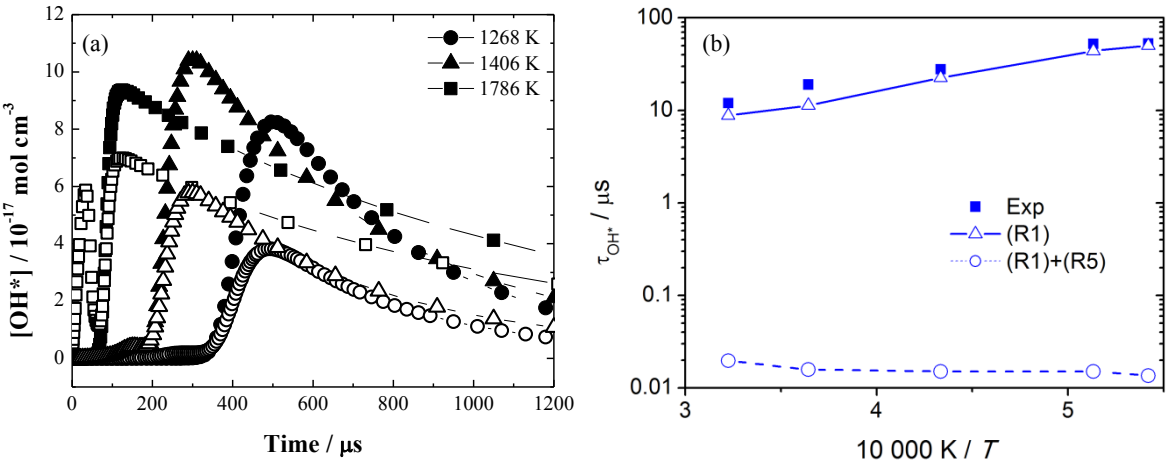

Figure 4.6: (a) Comparison of simulated OH* concentration profiles (b) measured and simulated ignition delay times obtained by incorporating reaction (R1), with (open symbols) and without (closed symbols with line) reaction $H_2 + HO_2 = OH^* + H_2O$ at different temperatures [79]. Mixture composition is 1.0% H_2 and 1.0% O_2 diluted in Ar at 1.2 bar.

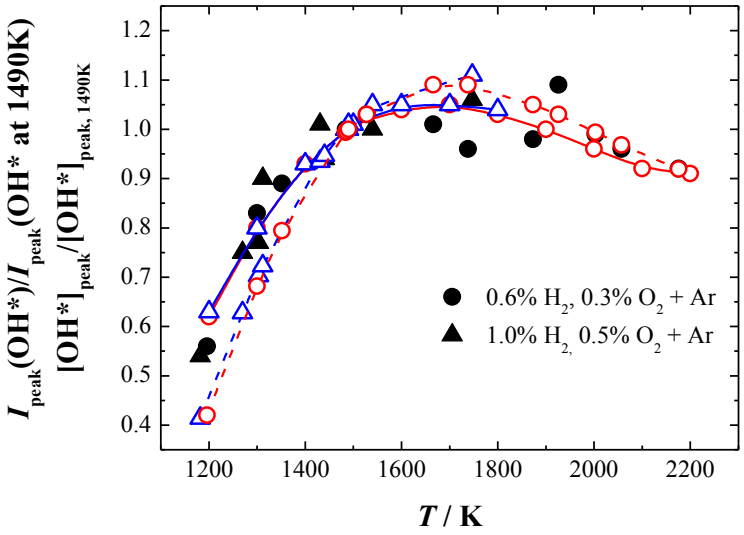

Figure 4.7: Peak value of OH* emission (experiment from [78]) and simulated concentration normalized to the corresponding value at 1490 K for stoichiometric H_2/O_2/Ar mixtures at 0.97 bar [79]. Closed symbols: experiments from Hall and Petersen [78]. Open symbols with solid lines: Simulation with k_1 derived in the present work. Open symbols with dashed lines are simulations with GRI-mech 3.0 [27] as base mechanism.

In order to validate our rate coefficient k_1, additional simulations were done with the measured maximum OH* intensity plotted against temperature from Hall and Petersen [78]. A good agreement is achieved with the rate coefficient (cf. Figure 4.7) determined in this work. This figure also shows a similar comparison with simulations based on the GRI mechanism

version 3.0 [27] as a base mechanism for hydrogen oxidation using k_1 from this work. Although the results deviate slightly from the simulation based on the present hydrogen mechanism they are nonetheless in agreement with the measurements.

4.1.4. OH* formation in $H_2/O_2/CH_4$/Ar systems

Based on the calibration approach derived in the previous study of OH* chemiluminescence in hydrogen systems, OH* chemiluminescence was studied in methane systems. For this purpose, mixtures containing both hydrogen and methane (see Table 4.2) were shock-heated, and time-resolved OH*- intensity profiles were recorded, evaluated for [OH*], and compared with simulation results.

Table 4.2: Mixture composition and experimental conditions of shock-heated methane-blended hydrogen/oxygen experiments.

Mixture	% H_2	% O_2	ppm CH_4	% Ar	T_5 / K	p_5 / bar
E	2.000	1.000	-	97.000	1440 – 3180	0.90 – 1.40
F	2.000	1.000	250	96.975	1384 – 2251	1.22 – 2.34
G	2.000	1.000	500	96.950	1410 – 2249	1.74 – 2.11

To account for the methane chemistry in the initial mixture composition, the GRI3.0 mechanism [27] was chosen to simulate the ground-state chemistry. This mechanism was previously developed for methane combustion and is extensively validated for a wide of experimental conditions. A quantitative study of OH* requires accurate knowledge of the time-dependent concentration of the corresponding precursor species leading to the formation of OH*, such as CH. The prediction of GRI3.0 mechanism of CH concentrations was previously demonstrated for premixed low-pressure methane/air flames at various equivalence ratios by Berg et al. [131]. Especially for near-stoichiometric conditions, an almost perfect agreement of CH concentration and peak position as function of the height above the burner (HAB) was found.

Figure 4.8a shows a typical temporal variation of the OH* concentration for an experiment with a pure H_2/O_2/Ar mixture (red line). It shows rapid formation of OH*, which is exclusively initiated by (R1) followed by slow depletion via radiative decay (R3) and collisional quenching (R4). For the CH_4-blended H_2/O_2/Ar mixture (black line), one can see a similar temporal behavior of the OH* CL with a slow depletion phase. However, the formation is significantly different compared to the pure H_2/O_2/Ar case. It shows a characteristic two-stage behavior. In the first stage, the concentration of the CH_4-containing mixture shows a first steep increase of OH* forming a peak, which afterwards rapidly declines. In the second stage, the OH* concentration merges into the slower depletion phase via reactions (R3) and (R4), as

it also occurs in pure $H_2/O_2/Ar$ mixtures. This two-phase behavior is attributed to the kinetics of the two reaction channels forming OH*, (R1) H + O + M = OH* + M and (R2) CH + O_2 = OH* + M.

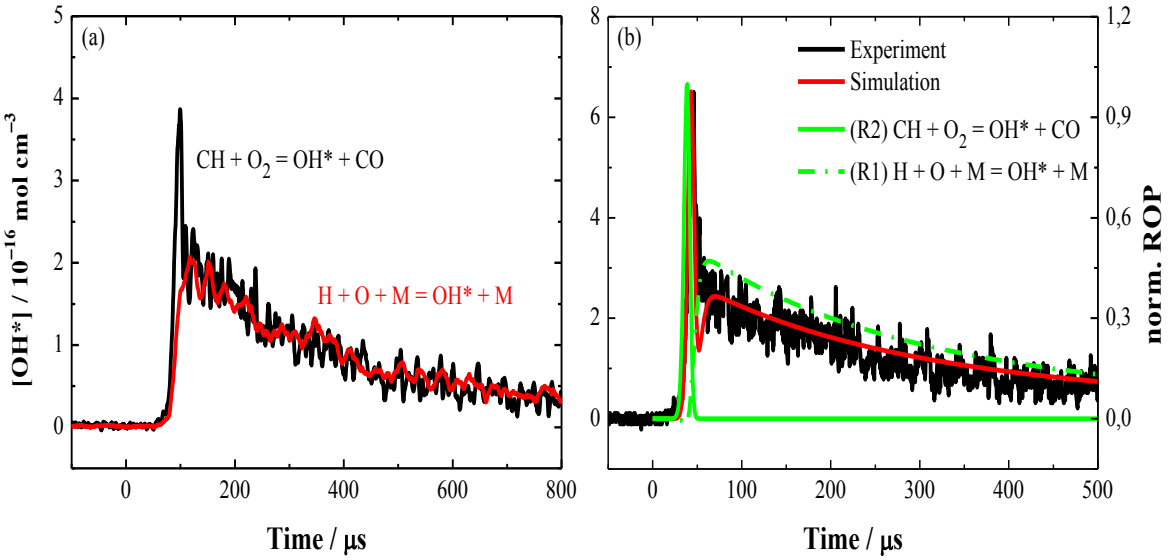

Figure 4.8: (a) Comparison of the temporal variation of the OH* concentration from two shock-tube experiments at T_5 = 1621 K and p_5 = 1.49 bar with mixture E (red line) mixture F (black line). (b) Absolute OH* concentration (simulation: solid red line, experiment: solid black line) with regard to the normalized rate-of-production (ROP) of reaction (R1) (dash dot line) and reaction (R2) (solid green line) forming OH*. Initial modeling conditions: T_5 = 1884 and p_5 = 1.76 bar for mixture F.

Figure 4.8b shows comparison of an experimental (solid black line) and simulated (solid red line) OH* concentration profile. The simulation was performed using the GRI3.0 mechanism [27] and the OH* kinetics model from the present work. The computed data can accurately predict the two-stage formation of OH*, which is primarily formed via CH + O_2 = OH* + CO (R2) and then later by H + O + M = OH* + M (R1). A good agreement was achieved in terms of profile shapes and peak positions throughout the entire range of experimental conditions.

The rate-of-production (ROP) analysis (green lines shown in Figure 4.8b) supports the experimentally observed dual-channel behavior. Under the present experimental conditions, reaction (R2) dominates the OH* formation and contributes almost three times more OH* than (R1). This is the case even though the initial concentration of methane is 80 times lower compared to hydrogen. The consumption of OH* in the first phase, where reaction CH + O_2 = OH* + CO (R2) dominates, is mainly attributed to the depletion of the CH concentration. Thus, OH* stringently follows the temporal behavior of [CH]. Therefore, [CH] and [OH*] profile shapes and peak positions perfectly match each other. Afterwards, when the contribution of reaction (R2) reaches its peak maximum and starts to decline, reaction (R1) via H + O + M = OH* + M arises and also contributes to the OH*-CL emission with a long decay time similar to the pure-hydrogen case (red line) presented in Figure 4.8a above. The ROP analysis also reveals that quenching of excited-state OH* in both stages is mainly attributed to collisions with H_2, H_2O and O_2. Compared to collisional quenching, OH* de-excitation via

radiative decay is of minor importance where only less than 10% is attributed to reaction (R3).

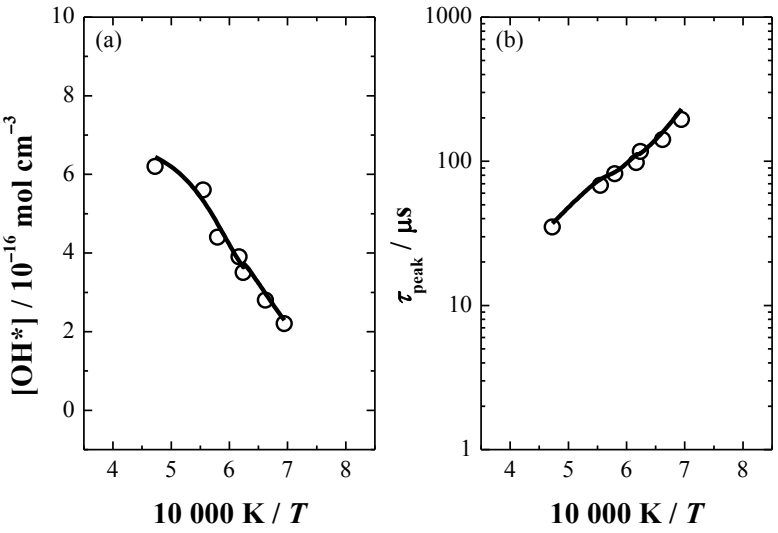

Figure 4.9: Measurement (symbols) and simulation (lines) of (a) OH* concentration and (b) peak times of OH* emission maximum for mixture F.

The reaction rate coefficient of the OH* formation reaction (R2) was optimized with regard to the absolute OH* concentrations measured in the present work, while keeping the other reaction rates constant. An initial value for k_2 was originally adopted from Smith et al. [51]. This value was varied for each shock-tube experiment for mixtures F and G until the experimental and computed concentration profiles matched for the first peak. A rate coefficient equal to 8.0×10^{10} $cm^3mol^{-1}s^{-1}$ without activation energy was found to give the best fit throughout the entire set of experimental data. Based on the calibration and the determined rate coefficient k_2 above, measured and simulated OH* concentrations and peak times were compared (see Figure 4.9). Good agreement was found in terms of absolute species concentrations, peak times and the time interval between the arrival of the reflected shock wave and the maximum of the chemiluminescence emission, for a wide range of experimental conditions.

Based on a sensitivity analysis in conjunction with a rate-of-production analysis (not shown here) one can summarize that OH* chemiluminescence shows strong sensitivity towards the ground-state chemistry. In particular the chain-branching reaction $H + O_2 = O + OH$ strongly influences the formation of OH*. This reaction promotes the generation of a radical pool by the consumption of CH_4 and which subsequently forms CH_3, $^1CH_2$ and $^3CH_2$. These latter species are important intermediates for the formation of CL-relevant CH radicals. At the peak time of [OH*], the sensitivity of the chain-branching reactions reverse and only reaction (R2) has a positive impact towards [OH*] while the OH* formation reaction via (R1) has a low sensitivity.

The rate coefficients for k_2 that are available in literature are shown in an Arrhenius representation in Figure 4.10. Our suggested rate coefficient is slightly higher than the value given by

Porter et al. [114] and Grebe and Homann [55]. The rate coefficient from Smith et al. [51] is about two times higher than our value. With regard to the underlying experimental and modeling uncertainties, there is an agreement for the range of k_2 to be around 10^{11} $cm^3mol^{-1}s^{-1}$. However, the recommendations from Hall and Petersen [78] are more than two orders of magnitude higher and lead to strong overprediction of the absolute OH* concentrations. The error consideration according to the procedure discussed in the previous section 4.1.3, where statistical and systematic errors were taken into account, revealed that the overall uncertainty in k_2 is ±32%.

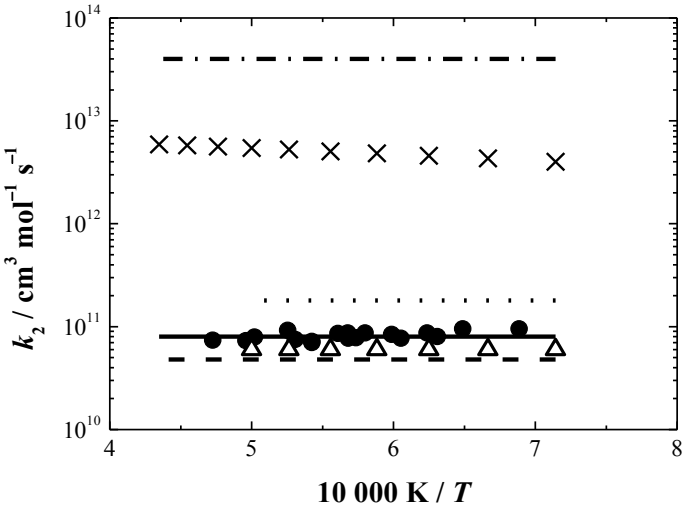

Figure 4.10: Arrhenius plot of the rate coefficients for the reaction CH + O_2 = OH* + CO (R2). ··· Smith et al. [51]; — · — Hall and Petersen [52]; × Hall and Petersen [78]; Δ Porter et al. [114]; – – Grebe and Homann [55]; • (experimental data) and — (fit) from present work.

4.1.5. OH* chemiluminescence in CH_4 systems

Methane oxidation is the simplest and frequently studied hydrocarbon combustion system and therefore, it is often investigated by chemiluminescence. One goal of the present study was to improve the knowledge of the chemiluminescence processes in methane combustion. For this purpose, additional shock-tube experiments with various argon-diluted CH_4/O_2 and CH_4/N_2O mixtures were performed. While the oxidation of methane with molecular oxygen provides low O/O_2 ratios, blending N_2O increases this ratio. Based on the almost instantaneous decomposition of N_2O which provides high amounts of atomic oxygen which affect the ground-state chemistry and hence the further progress of the chemiluminescence. The reaction time scales are much shorter compared to the oxidation with O_2 and other potential formation channels of chemiluminescence reactions can be tested. Investigating the influence of various O/O_2 ratios is especially important for the formation of CH* (cf. further discussion in 4.2.3).

The GRI3.0 mechanism [27] was used, which can precisely predict the precursors leading to OH* chemiluminescence. The experimental conditions are tabulated in Table 4.3.

Table 4.3: Mixture compositions and experimental conditions of CH_4 experiments.

Mixture	% CH_4	% O_2	% N_2O	% Ar	ϕ	T_5 / K	p_5 / bar
1	0.10	0.16	-	99.74	1.25	1779 – 2410	1.51 – 1.95
2	0.10	0.20	-	99.70	1.00	1956 – 2379	1.59 – 1.75
3	0.10	0.27	-	99.63	0.75	1861 – 2290	1.59 – 1.93
4	0.10	-	0.32	99.58	1.25	1889 – 2421	1.73 – 1.95
5	0.10	-	0.40	99.50	1.00	1837 – 2440	1.75 – 1.99
6	0.10	-	0.53	99.37	0.75	1900 – 2427	1.75 – 1.93

The formation of OH* in various $CH_4/O_2/Ar$ and $CH_4/N_2O/Ar$ mixtures proceeds analogous to the reaction pathway described in section 4.1.4, where CH_4 breaks to CH which finally forms OH*. Figure 4.11a shows a typical time-resolved OH* concentration profile for a fuel-lean $CH_4/O_2/Ar$ mixture.

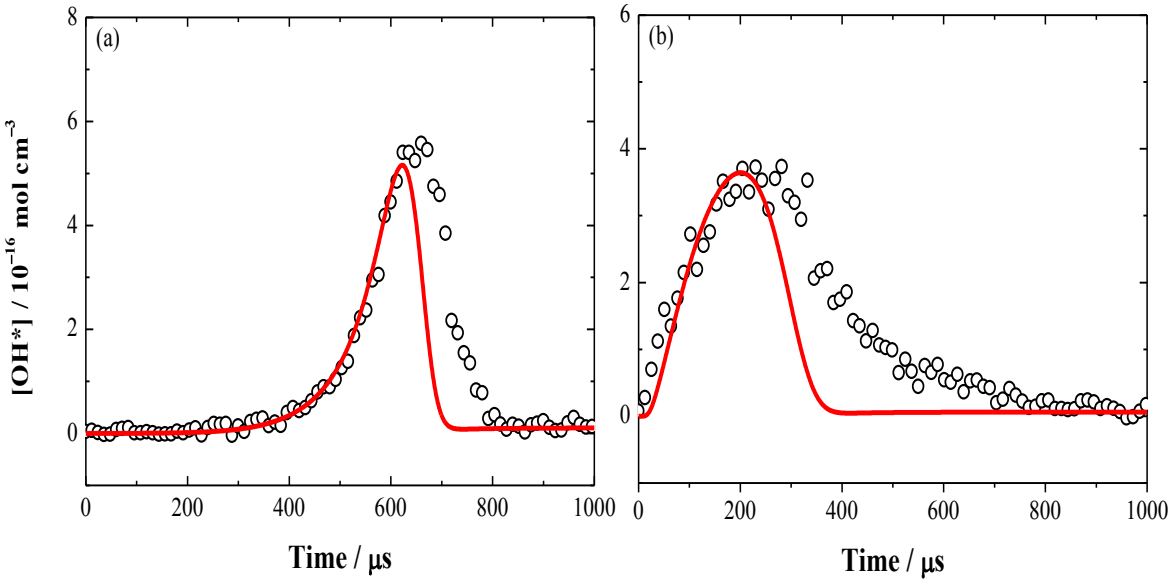

Figure 4.11: Comparison of the temporal variation of the OH* concentration profile from shock-tube experiments (symbols) and simulation (line) at T_5 = 1900 K and p_5 = 1.90 bar (a) with mixture 3 and (b) with mixture 5.

The experimental [OH*] trace shows a distinct induction time which is typical for methane combustion and is attributed to the slow formation of CH radicals at lower temperatures. The simulation predicts the formation behavior and the absolute peak concentration with the corresponding peak position fairly well. However, discrepancies exist in the temporal decay behavior of OH*. Figure 4.11b shows a typical time-resolved OH* concentration profile for a lean $CH_4/N_2O/Ar$ mixture. The formation of OH* CL in N_2O-based mixtures starts significantly faster compared to the cases with molecular oxygen. While the peak concentration and

the formation behavior is predicted very well, the decay of OH* is predicted to be faster than it is observed in the corresponding experiment. These deviations are attributed to an overprediction of the temporal CH removal for the simulations where the measured OH* concentration stringently follows the fast removal of CH radicals.

The temperature dependent OH* concentration and peak times for fuel-rich conditions are given in Figure 4.12. Both parameters show an exponential behavior as a function of the inverse temperature. The simulations represent the temperature dependence of the absolute OH* concentrations as well as peak times within the entire experimental temperature range.

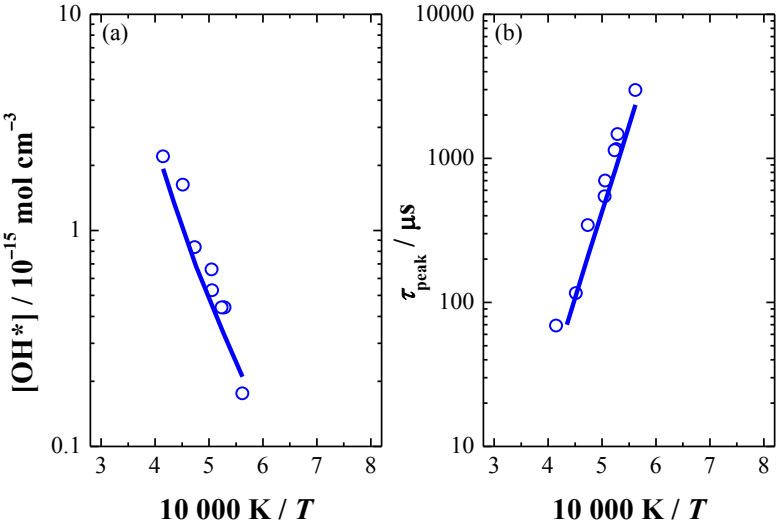

Figure 4.12: Measurement (symbols) and simulation (lines) of (a) OH* concentration and (b) peak times of OH* for mixture 1.

Compared to CH_4/O_2-based mixtures, shock-heated CH_4/N_2O/Ar mixtures show stronger temperature dependence with regard to the OH* concentration. However, the peak times for both oxidizers show similar temperature dependence. While there is accordance in reproducing the peak times, the computed OH* peak concentrations tend to be slightly overpredicted especially for low temperatures. The predicted OH* concentrations are up to two times higher compared to the experimental results which can be attributed to potential errors in determining the absolute CH concentrations and related kinetics. This assumption is also supported by the fact, that there are no validation data in terms of absolute CH concentrations in CH_4/N_2O available for the base mechanism GRI3.0 which would be useful to localize the deficiencies between experiment and simulation. The simulations show a weaker slope and therefore, lower temperature dependence than the experiments show (see also Figure 4.13a). Berg et al. [131] measured the absolute CH concentration for methane and oxygen mixtures and found out that there is good agreement between the experiment and model. However, CH in N_2O-blended mixtures was not studied yet, therefore, differences can be mainly attributed to uncertainties in the ground-state model.

The temperature-dependent concentrations and peak times in Figure 4.12 were described empirically by an Arrhenius-like equation ([OH*] = $A\times\exp(-E_a/RT)$ and $\tau = A\times\exp(-E_a/RT)$, respectively). Hence, the temperature dependent OH* concentration and peak times can be described by the corresponding activation energy. The activation energies of OH* concentration and peak times in various CH_4/O_2/Ar (black lines and symbols) and CH_4/N_2O/Ar (grey lines and symbols) mixtures are summarized in Figure 4.13. While there is good agreement between experiments and simulations for the peak times (see plot b) in cases of O_2 and N_2O oxidation, respectively, the activation energy of the OH* concentration in the N_2O case (see plot a) tends to be underpredicted with regard to the experiments. The activation energy for O_2-based mixtures shows only minor differences which is caused by an overprediction of OH* at low temperatures. The different temperature dependencies of the O_2 and N_2O cases in methane are not distinct especially for the peak times (cf. Figure 4.13b). However, the absolute peak times for N_2O-based mixtures are more than three times lower than for the oxygen cases.

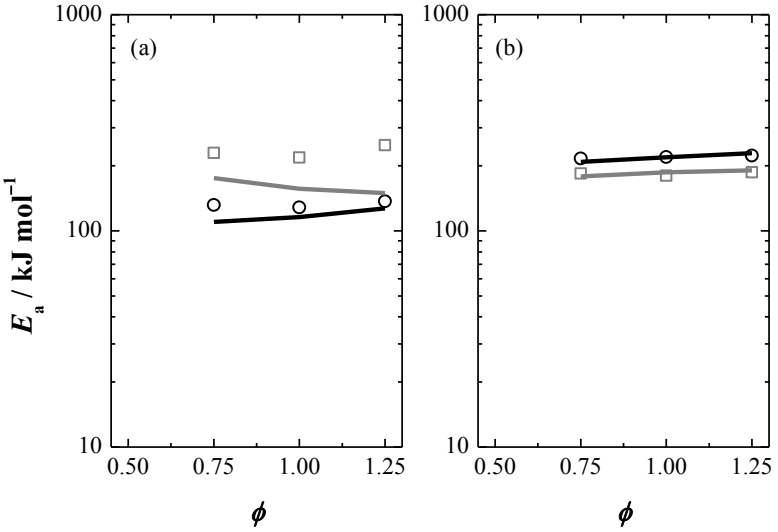

Figure 4.13: Measured (symbols) and simulated (lines) activation energy E_a of (a) OH* concentrations and (b) OH* peak times as a function of equivalence ratio ϕ. The open circles and black lines represent the mixtures containing CH_4/O_2/Ar (mixtures 1 – 3) and the open squares and grey lines represent the mixtures containing CH_4/N_2O/Ar (mixtures 4 – 6).

4.1.6. OH* chemiluminescence in C_2H_2 systems

For further validation of the OH* reaction mechanism in more complex hydrocarbon systems, OH* chemiluminescence was studied in various C_2H_2-based combustion cases. Hence, over 120 shock-tube experiments with Ar-diluted C_2H_2/O_2 and C_2H_2/N_2O mixtures were carried out from lean to fuel-rich conditions around atmospheric pressure (see Table 4.4).

Table 4.4: Mixture compositions and experimental conditions of C_2H_2 experiments.

Mixture	% C_2H_2	% O_2	% N_2O	% Ar	ϕ	T_5 / K	p_5 / bar
7	0.10	0.20	-	99.70	1.25	1470 – 2266	1.74 – 1.95
8	0.10	0.25	-	99.65	1.00	1346 – 2504	1.18 – 2.01
9	0.10	0.33	-	99.57	0.75	1721 – 2507	1.19 – 1.44
10	0.10	0.50	-	99.40	0.50	1772 – 2535	1.10 – 1.47
11	0.10	-	0.50	99.40	1.00	1886 – 2497	1.13 – 1.46
12	0.10	-	0.67	99.23	0.75	1783 – 2455	1.18 – 1.40
13	0.10	-	1.00	98.90	0.50	1739 – 2449	1.18 – 1.42

The OH* sub-mechanism developed based on the previous H_2/O_2/Ar and CH_4-doped H_2/O_2/Ar experiments was applied to acetylene oxidation experiments. The underlying C_2H_2 ground-state chemistry was modeled based on the Wang and Laskin mechanism [35] described in section 2.2.3. The acetylene ground-state mechanism was originally developed for the high-temperature oxidation of acetylene with molecular oxygen. To account for oxidation with N_2O, additional NO_x reactions from the GRI3.0 mechanism [27] were implemented in the present work from Wang and Laskin [35]. The OH* sub-mechanism was primarily tested with regard to the C_2H_2/O_2/Ar experiments in order to demonstrate the accuracy of the original ground-state mechanism. Afterwards, the C_2H_2/N_2O/Ar experiments were simulated with the extended mechanism. The time-resolved OH*-emission profiles from the shock-tube experiments were converted into absolute species concentrations, by means of the calibration procedure derived in section 4.1.3 and tested for hydrocarbon oxidation as presented in section 4.1.4 and 4.1.5. Thus, simulations were compared with time-resolved OH* concentration profiles and their corresponding peak times.

Figure 4.14 shows a typical experimental time-resolved OH*-concentration profile (symbols) for a stoichiometric C_2H_2/O_2/Ar mixture. An almost symmetric peak shape of the [OH*] profile is observed for C_2H_2/O_2/Ar mixtures where the formation and the consumption of OH* occur on similar time scales which is typical for O_2-containing mixtures. The experimental peak time is around 200 µs and the respective OH* concentration is 3×10^{-15} mol cm^{-3}. While the corresponding simulation (solid line) can almost perfectly predict the peak position and the peak concentration of OH* CL, small deviations in the temporal profile shape of OH* during its formation and the consumption can be observed. These deviations are potentially attributed to inaccuracies in the formation behavior of the predicted precursor concentration. The underlying ground-state model from Wang and Laskin [35] was originally not validated regarding CH species. Therefore, the temporal deviations are attributed to modeling errors

rather than reduced experimental time-resolution. Overall, the model was found to be capable to predict the temporal behavior of OH* chemiluminescence and the absolute concentration within the entire experimental range and for all equivalence ratios (cf. Figure 4.16 and Figure 4.19).

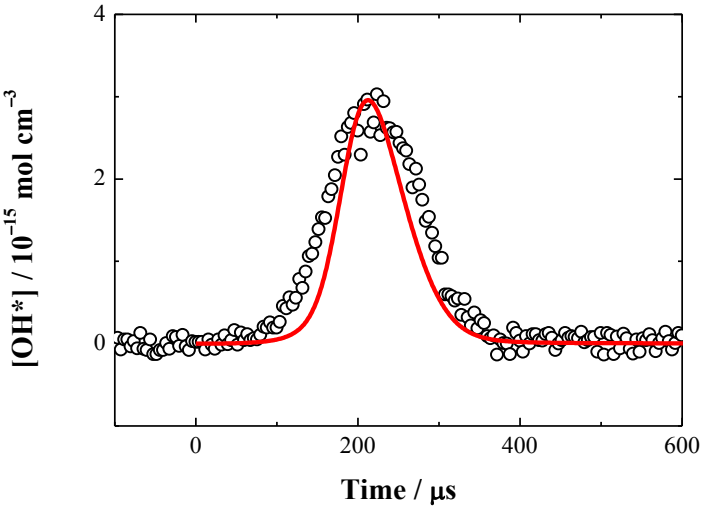

Figure 4.14: Comparison of the temporal variation of the OH* concentration from shock-tube experiment (symbols) and simulation (line) at T_5 = 1900 K and p_5 = 1.32 bar with mixture 8.

Similar to the results for methane oxidation, the rate-of-production analysis for the C_2H_2 system (not shown here for the sake of brevity) confirms that the formation of OH* chemiluminescence in $C_2H_2/O_2/Ar$ mixtures is solely attributed to the reaction (R2) via CH + O_2 = OH* + CO. On the other hand, reaction (R1) via H + O + M = OH* + M reverses and consumes OH*. Again, the further consumption of OH* is mainly caused by quenching with the bath gas argon and by O_2. Moreover, radiative decay is also an important consumption pathway of OH*, however, it is of minor importance compared to collisional quenching.

As expected, OH* chemiluminescence shows significant dependence on the ground-state chemistry shown by the local sensitivity analysis in Figure 4.15. During the induction phase, OH* formation is dominated by the chain-branching reaction (i) H + O_2 = O + OH. This reaction controls the formation of the radical pool predominantly consisting of O, OH and H radicals which are finally required for the formation of CH radicals. The formation of CH molecules relevant for chemiluminescence proceeds from the fuel decomposition of C_2H_2 towards $^3CH_2$ and HCCO. Both species are formed via chain-initiation reactions incorporating acetylene molecules and O atoms. CH is a product of secondary chain-branching reactions of $^3CH_2$ and HCCO. Additionally, CH is directly formed from the intermediate species $^1CH_2$ and C_2H, however, their contribution is found to be of minor importance compared to the $^3CH_2$ and HCCO routes. Reactions CH + CO (+ M) = HCCO (+ M) and C_2H_2 + O_2 = HCCO + H show a strong impact on OH*. At the peak maximum of OH*, only reaction CH + O_2 = OH* + CO contributes to the chemiluminescence formation. After passing the peak concentration of OH*, the sensitivity of the reactions H + O_2 = O + OH, CH + CO (+ M) = HCCO (+ M)

and $C_2H_2 + O_2 = HCCO + H$ reverse and show negative sensitivity towards OH* CL. Reaction $CH + O_2 = HCO + O$ as a direct consumption pathway of CH molecules permanently shows a negative sensitivity. The sensitivity analysis reveals that the peak concentration of OH* is solely determined by the rate coefficient k_2 and therefore, a good knowledge of absolute CH concentration is strongly required. Based on the good concordance between experiment and simulation, one can conclude a good performance of the ground-state mechanism in predicting the formation pathway towards CH.

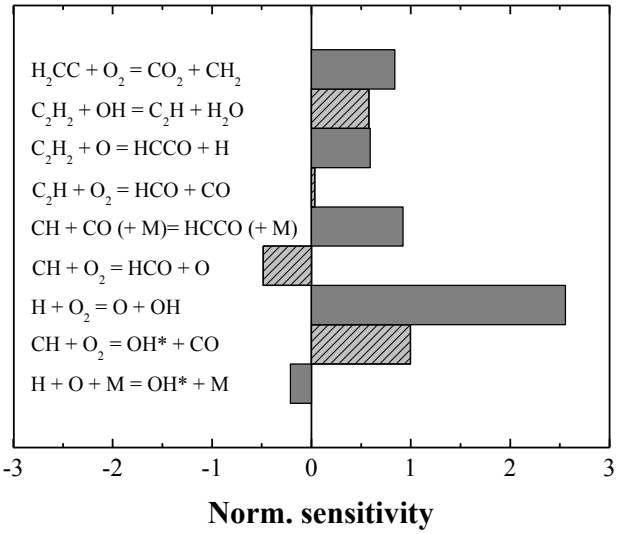

Figure 4.15: Normalized sensitivity of OH* formation for mixture 8 at T_5 = 2100 K and p_5 = 1.32 bar at t = 186 µs.

The measured and simulated OH* peak concentrations and peak times for a fuel-rich $C_2H_2/O_2/Ar$ mixture as a function of the inverse temperature are shown in Figure 4.16. Both, absolute OH* concentrations and peak times show an exponential behavior. While the OH* concentration increases exponentially with increasing temperature, the peak times show an opposite trend. There is good agreement between the modeling results and the experimental observation in terms of absolute OH* concentration and peak times. This good correlation can be observed for all mixture compositions throughout the entire experimental conditions.

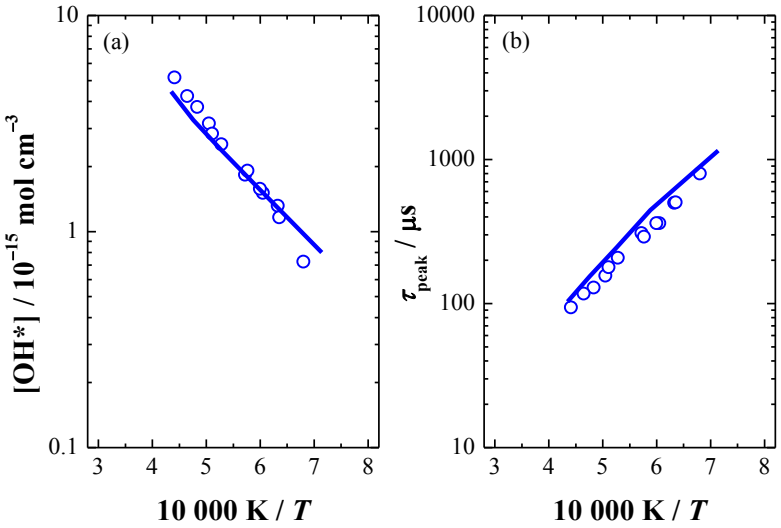

Figure 4.16: Measurement (symbols) and simulation (lines) of (a) OH* concentration and (b) peak times of OH* for mixture 7.

The OH* sub-mechanism determined in the present work was used as before without further changes. The profiles of OH* in C_2H_2/N_2O mixtures are significantly different to the experiments with molecular oxygen. The fast decomposition of N_2O, even for low temperatures, produces a high amount of O atoms that enhance the build-up of the radical pool and subsequently promote OH* formation. This is also reflected in the significantly faster ignition delay compared to the $C_2H_2/O_2/Ar$ system.

Figure 4.17 shows a typical time-resolved OH* concentration profile for a N_2O-based mixture. In contrast to the almost symmetric [OH*] profiles in $C_2H_2/O_2/Ar$ mixtures (cf. Figure 4.14), OH* formation in $C_2H_2/N_2O/Ar$ mixtures occurs much faster than it decays. The reaction begins quasi instantaneously at $t = 0$ µs. For $C_2H_2/O_2/Ar$ mixtures an induction time between reaching the experimental conditions and the formation of OH* is observable. On the other hand, OH* CL in mixtures with N_2O does not show an induction phase even at lower temperatures. Some discrepancies between the simulation and the experiment are seen at the peak position and the decay. This is mainly due to inaccuracies in the CH kinetics that controls OH* formation via the reaction CH + O_2 = OH* + CO. However, there is good agreement in determining the OH* peak concentration. A detailed validation of the ground-state mechanism incorporating the NO_x chemistry is mandatory to increase the simulation performance.

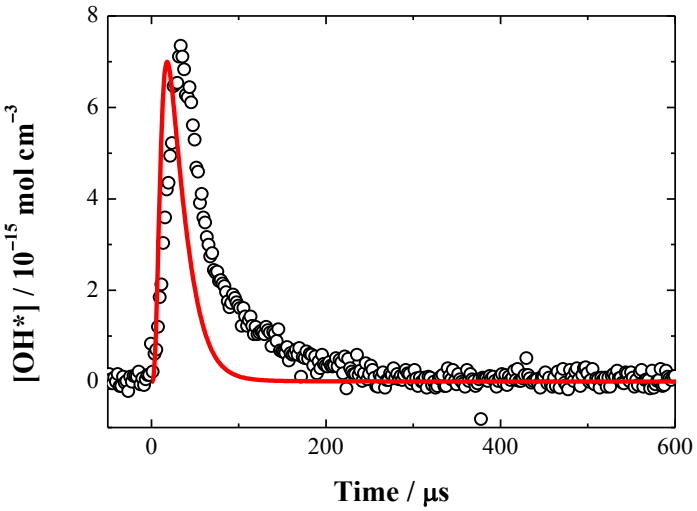

Figure 4.17: Comparison of the temporal variation of the OH* concentration profile from shock-tube experiment (symbols) and simulation (line) at T_5 = 2100 K and p_5 = 1.32 bar with mixture 13.

The peak concentrations of OH* and the peak times show exponential behavior with strong temperature dependence (see Figure 4.18). Compared to the C_2H_2/O_2/Ar data, OH* CL in C_2H_2/N_2O/Ar mixtures show a stronger temperature dependence, by more than a factor of two (see Figure 4.19).

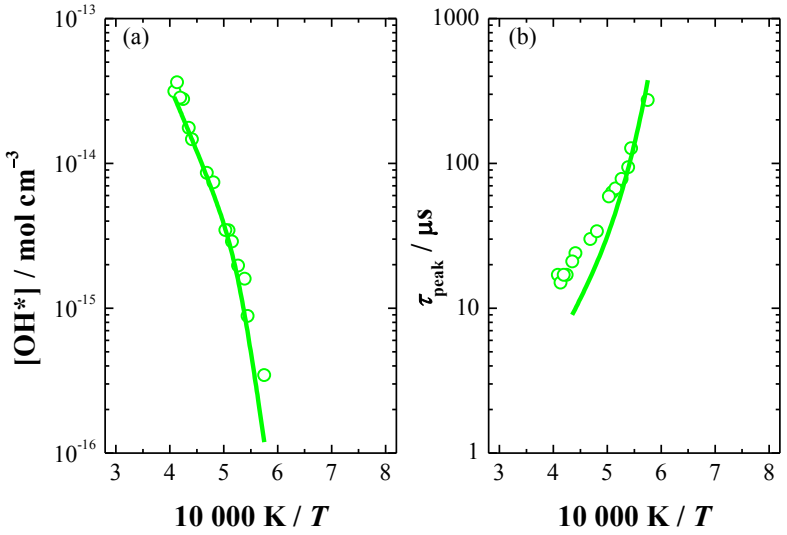

Figure 4.18: Measurement (symbols) and simulation (lines) of (a) OH* concentration and (b) peak times of OH* for mixture 13.

The activation energies of the OH* concentrations and peak times for acetylene with O_2 and N_2O oxidation are summarized in Figure 4.19 For the molecular case, the values vary around 70 kJ mol^{-1} while the experiments for N_2O show a two times higher temperature dependence. Overall, there is a good agreement between the experimental and simulated data.

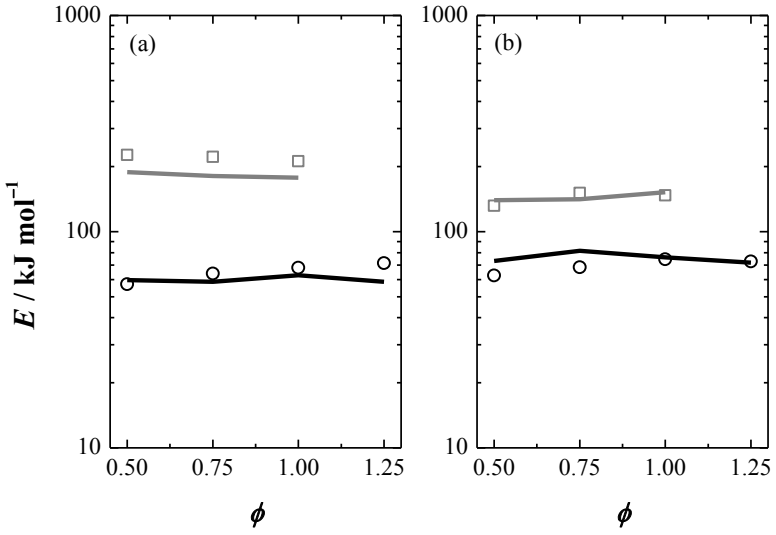

Figure 4.19: Measured (symbols) and simulated (lines) activation energy E_a as a function of equivalence ratio ϕ. The open circles and black lines represent the mixtures containing $C_2H_2/O_2/Ar$ (mixtures 7 – 10) and the open squares and grey lines represent the mixtures containing $C_2H_2/N_2O/Ar$ (mixtures 11 – 13).

Overall, the comprehensive model consisting of C_2H_2, NO_x and OH* chemistry can almost perfectly predict the temperature dependence of the OH* concentrations for a wide range of conditions and for both oxidizers. However, some discrepancies between simulations and experiments are found for the peak times for N_2O-based mixtures where the simulated OH* peak times tend to be too fast. In particular, the experimental peak times for high temperatures are about two times higher than the respective simulations predict. This discrepancy could be attributed to the interaction of the acetylene ground-state model and the implemented NO_x model, owing to the fact that the NO_x mechanism was originally validated for CH_4, not acetylene, combustion. Therefore, the extended model is in principle capable to represent the global oxidation of acetylene and N_2O but detailed validation with regard to the corresponding species of interest would improve the accuracy of the modeling.

4.1.7. OH* chemiluminescence in C_2H_4 systems

The OH* chemiluminescence sub-mechanism was also applied to C_2H_4 oxidation. Because the ground-state mechanism from Wang and Laskin [35] is also optimized for ethylene oxidation, further shock-tube experiments with various $C_2H_4/O_2/Ar$ and $C_2H_4/N_2O/Ar$ mixtures for OH* chemiluminescence were performed. The experimental conditions are given in Table 4.5.

Table 4.5: Mixture compositions and experimental conditions of C_2H_4 experiments.

Mixture	% C_2H_4	% O_2	% N_2O	% Ar	ϕ	T_5 / K	p_5 / bar
14	0.10	0.24	-	99.66	1.25	1548 – 2452	1.75 – 2.05
15	0.10	0.30	-	99.60	1.00	1441 – 2288	1.86 – 2.11
16	0.10	0.40	-	99.50	0.75	1484 – 2248	1.66 – 2.08
17	0.10	0.60	-	99.30	0.50	1485 – 2339	1.70 – 2.16
18	0.10	-	0.48	99.42	1.25	1785 – 2401	1.62 – 1.98
19	0.10	-	0.60	99.30	0.00	1779 – 2406	1.74 – 2.07
20	0.10	-	0.80	99.10	0.75	1719 – 2365	1.68 – 2.01

The OH* chemiluminescence profiles of C_2H_4 show similarities to those of acetylene, thus, the results will only be briefly discussed. The reaction pathway analysis shows that C_2H_4 primarily decomposes to C_2H_3 and due to subsequent H-abstraction C_2H_2 is formed. At this stage, the reaction scheme proceeds analogous to the formation of OH* in acetylene combustion as described in 4.1.6.

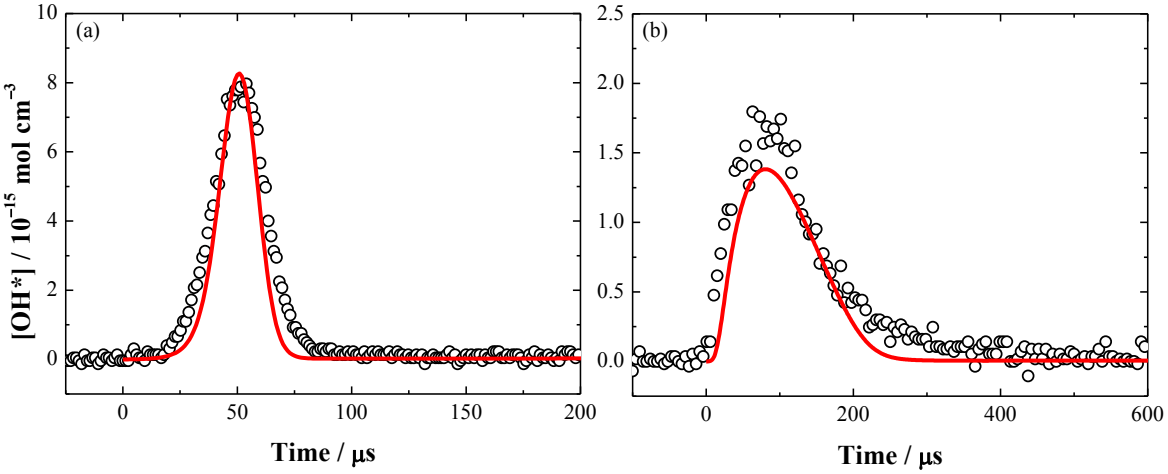

Figure 4.20: Comparison of the temporal variation of the OH*-concentration profile from shock-tube experiment (symbols) and simulation (line) for (a) $C_2H_4/O_2/Ar$ mixture 17 at T_5 = 2100 K and p_5 = 1.90 bar and (b) $C_2H_4/N_2O/Ar$ mixture 19 at T_5 = 1900 K and p_5 = 1.90 bar.

Figure 4.20a shows a typical temporal OH* concentration profile for a fuel-lean $C_2H_4/O_2/Ar$ mixture. Similar to the acetylene data, OH* formation in $C_2H_4/O_2/Ar$ mixtures shows an induction time for the rise in the OH* concentration. The formation of OH* CL shows an ignition delay of 25 µs and the signal peak is located at 50 µs. OH* chemiluminescence is subsequently quenched within 25 µs. Here again, the simulation reproduces all the features of the measured OH* fairly well. Figure 4.20b shows a typical temporal OH*-concentration pro-

file for a stoichiometric $C_2H_4/N_2O/Ar$ mixture at 1900 K with an instantaneous formation and slow decay of OH*. When considering the experimental error limits, the modeling performance is fairly satisfying in the temporal behavior as well as in the absolute OH* concentration throughout the experiments

The absolute OH* concentration and peak times as a function of inverse temperature for a fuel-lean $C_2H_4/O_2/Ar$ mixture are shown in Figure 4.21. Here again, a good agreement between simulated and experimental results of both parameters within the entire temperature range is illustrated. In general, the simulations show good performance with regard to the experimental data for all $C_2H_4/O_2/Ar$ mixtures in terms of absolute OH* concentration and peak times. Analogous to the previous results for C_2H_2, peak concentrations and peak times in $C_2H_4/N_2O/Ar$, the modeling results are in good agreement with the experimental data for a wide range of conditions.

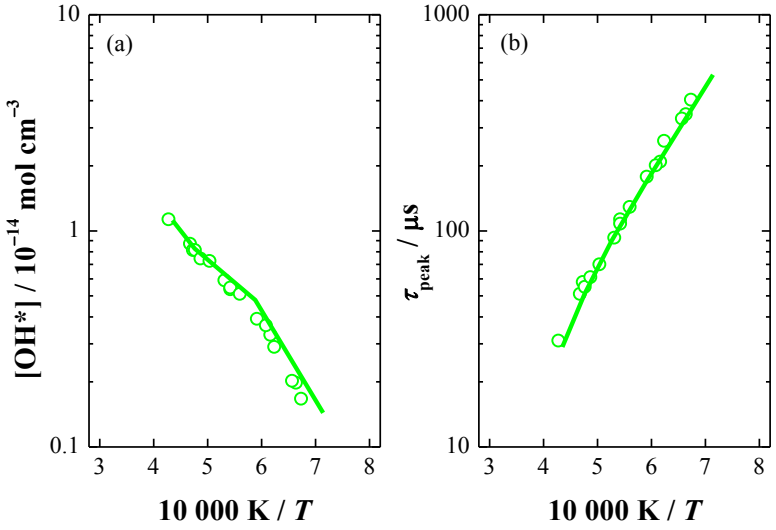

Figure 4.21: Measurement (symbols) and simulation (lines) of (a) OH* concentration and (b) peak times of OH* for mixture 17.

The temperature dependence of the OH* concentration and the peak times are evaluated by means of the activation energy as illustrated in Figure 4.22. For blends with molecular oxygen as oxidizer (see black lines and symbols) there is good agreement between the experimental and simulated activation energy, around 70 kJ mol^{-1} for OH* peak concentrations and around 80 kJ mol^{-1} for OH* peak times respectively. For mixtures with N_2O as oxidizer the activation energy for OH* peak concentration varies around 200 kJ mol^{-1} and for OH* peak times around 150 kJ mol^{-1}. These values are in agreement with the acetylene case presented in the previous section. Again, there are deviations in the activation energies of OH* peak concentrations in N_2O-containing mixtures (see grey line and symbols). These discrepancies can be observed for all hydrocarbon/N_2O mixtures and are attributed to inaccuracies in the precursor kinetics when incorporating NO_x chemistry. The calculated activation energies of the peak concentrations for N_2O-doped mixtures are 30% lower than the experiments show. Nonethe-

less, the mechanism can still reproduce the temperature behavior of the peak times fairly well as shown in Figure 4.22b.

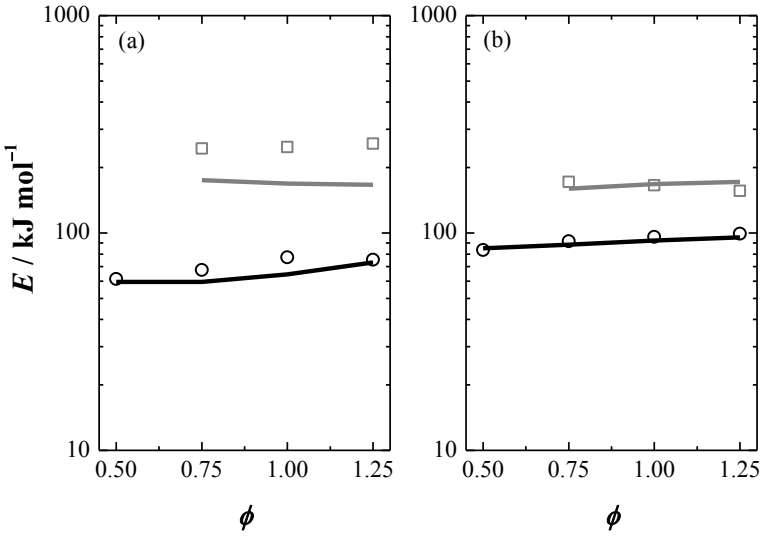

Figure 4.22: Measured (symbols) and simulated (lines) activation energy E_a of (a) OH* concentrations and (b) OH* peak times as a function of equivalence ratio ϕ. The open circles and black lines represent $C_2H_4/O_2/Ar$ mixtures (14 – 17) and the open squares and grey lines represent $C_2H_4/N_2O/Ar$ mixtures (18 – 20).

4.1.8. OH* chemiluminescence in C_2H_5OH systems

Ethanol-blending is frequently employed to increase the regenerative bio-fuel compound in conventional fuels. However, the fundamental oxidation process of ethanol for high temperatures is still under-researched and the present kinetics mechanisms are limited with regard to the experimental conditions. Therefore, the generation of OH* chemiluminescence was used in order to provide additional validation data in terms of ignition delay times and time-resolved OH* concentration profiles. For this purpose, a comprehensive mechanism describing the high-temperature kinetics of ethanol oxidation from Marinov [38] was adopted and was tested against shock-tube experiments from the present work. The experimental conditions are presented in Table 4.6.

Table 4.6: Mixture compositions and experimental conditions of shock-heated C_2H_5OH/O_2-based mixtures.

Mixture	% C_2H_5OH	% O_2	% Ar	ϕ	T_5 / K	p_5 / bar
21	0.10	0.24	99.66	1.25	1484 – 2483	1.71 – 2.16
22	0.10	0.30	99.60	1.00	1473 – 2500	1.62 – 2.11
23	0.10	0.40	99.50	0.75	1530 – 2466	1.75 – 2.06

Figure 4.23 shows a typical concentration-time history of OH* chemiluminescence for a stoichiometric ethanol/oxygen mixture behind the reflected shock wave. In contrast to the OH* formation in small hydrocarbons (CH_4, C_2H_2 and C_2H_4), OH* in ethanol oxidation arises quasi instantaneously without induction time. This is attributed to the fast decomposition of ethanol which is finished within several microseconds. On the other hand, the conversion of the other hydrocarbons can last several hundreds of microseconds in comparable conditions.

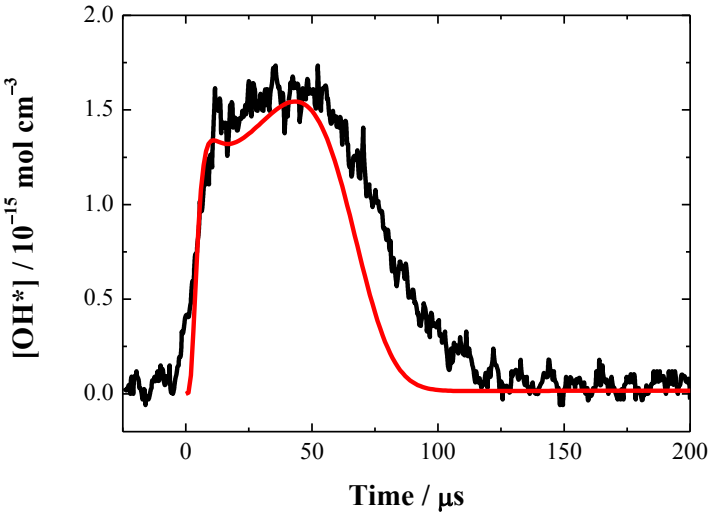

Figure 4.23: Comparison of the temporal variation of the normalized OH* chemiluminescence (black line) and the OH* concentration (red line) simulated with the rate coefficients k_1 and k_2 from this work. The mixture composition is 22 at T_5 = 1900 K and p_5 = 1.90 bar.

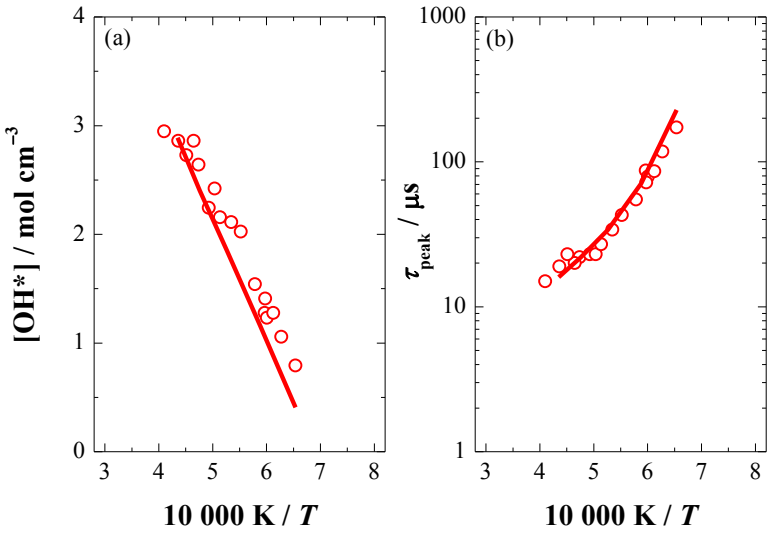

Figure 4.24: Measurement (symbols) and simulation (lines) of (a) OH* concentration and (b) peak times of OH* for mixture 23.

The measured and simulated OH* peak concentrations and peak times are shown in Figure 4.24 for a fuel-lean mixture. Good agreement between the simulated and experimental data was found. There are small discrepancies in the OH* concentration at lower temperatures while the predicted peak times of OH* chemiluminescence are in good agreement with the

experimental observations in terms of absolute values and the temperature dependence is exemplarily shown for the fuel-lean case in Figure 4.24b.

Figure 4.25 summarizes the temperature dependence of the OH* concentration and the peak times by means of the activation energy E_a as function of the equivalence ratio. The peak times can be predicted with an accuracy of ±10% throughout all equivalence ratios (see Figure 4.25b). However, small deviations in the computed temperature dependence of OH* peak concentration (see Figure 4.25a) still exist. In particular, the simulated activation energy of the OH* peak concentration shown below is about 50% lower than the experimental data for the other hydrocarbon/oxygen mixtures.

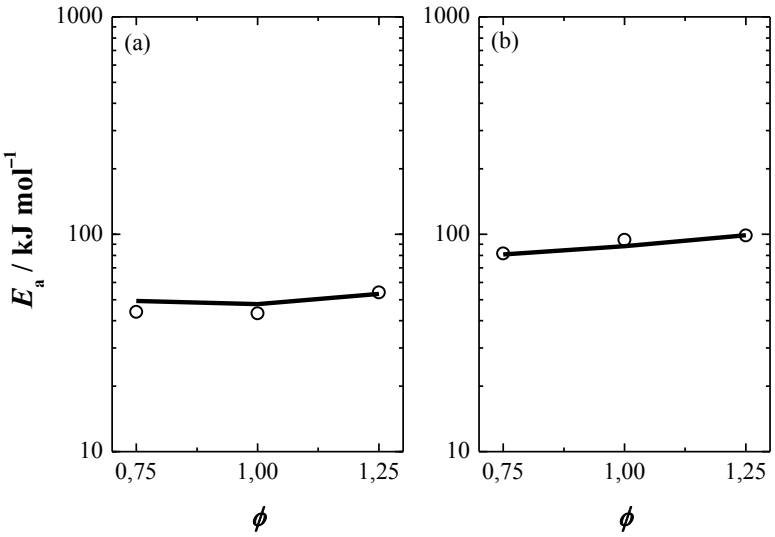

Figure 4.25: Measured (symbols) and simulated (lines) activation energy E_a of (a) OH* concentrations and (b) OH* peak times as a function of equivalence ratio ϕ for mixtures containing C_2H_5OH/O_2 (mixtures 21 – 23).

4.1.9. OH* kinetics model

Based on the literature review described in section 4.1.1, an initial kinetics mechanism describing the OH* chemistry was compiled where different recommendations for potential formation reactions of OH* were considered. This initial OH* sub-mechanism was implanted in the base mechanisms and the simulations were tested against extensive shock-tube experiments (see sections 4.1.3 – 4.1.8) and additional flame experiments from literature (see section 4.1.10). Quenching reactions with their corresponding rate coefficients were adopted from [68], whereas the formation reactions and the rate coefficients were derived based on the present experimental data.

The high-temperature calibration where OH* is mainly thermally produced was used to calibrate the optical setup. Based on this approach the formation of OH* for low temperatures where chemical formation is the only source for OH* was investigated. These shock-tube experiments with different $H_2/O_2/Ar$ mixtures revealed that the hydrogen oxidation reaction

(R1) via H + O + M = OH* + M is the major pathway leading to OH* chemiluminescence. The measured temporal OH* concentration profiles and their corresponding ignition delay times were used to determine the underlying rate coefficient k_1 which is tabulated in Table 4.7.

OH* chemiluminescence in hydrocarbon combustion was primarily studied in methane combustion. Again, the comparison between experimental and simulation results in terms of absolute OH* concentrations and ignition delay times showed that OH* is formed via reaction (R2) CH + O_2 = OH* + CO. The corresponding rate coefficient k_2 was determined by varying the rate coefficients within the OH* kinetics mechanism in order to reproduce the experimental observations. The final rate coefficients for k_1 and k_2 were derived based on the hydrogen and the methane studies. The final mechanism that incorporates the formation and consumption reactions considered in the present work is presented in Table 4.8.

Table 4.8: Reaction kinetics scheme of OH* species. Reaction rate coefficient $k = AT^n \exp(-E/RT)$.

No.	Elementary reaction	A (cm mol s)	n	E_a / kJ mol^{-1}	Reference
R1	H + O + M = OH* + M	1.50E+13	0.0	25.0	Present work
R2	CH + O_2 = OH* + CO	8.00E+10	0.0	0.0	Present work
R3	OH* = OH + $h\nu$	1.45E+06	0.0	0.0	[51]
R4,1	OH* + O_2 = OH + O_2	2.10E+12	0.5	–2.0	[68]
R4,2	OH* + H_2O = OH + H_2O	5.93E+12	0.5	–3.6	[68]
R4,3	OH* + H_2 = OH + H_2	2.95E+12	0.5	–1.9	[68]
R4,4	OH* + N_2 = OH + N_2	1.08E+11	0.5	–5.2	[68]
R4,5	OH* + OH = OH + OH	6.01E+12	0.5	–3.2	[68]
R4,6	OH* + H = OH + H	1.31E+12	0.5	–0.7	[68]
R4,7	OH* + Ar = OH + Ar	1.69E+12	0.0	17.3	[118]
R4,8	OH* + CO = OH + CO	2.76E+12	0.5	–4.1	[68]
R4,9	OH* + CO_2 = OH + CO_2	3.23E+12	0.5	–3.3	[68]
R4,10	OH* + CH_4 = OH + CH_4	3.36E+12	0.5	–2.7	[68]

With M = [H_2] + 6.5[H_2O] + 0.4[O_2] + 0.4[N_2] + 0.35[Ar].

4.1.10. Additional validation of the OH*-chemiluminescence mechanism with laminar premixed flames

The present OH* kinetics mechanism in combination with the GRI 3.0 mechanism was used to simulate the measured OH* chemiluminescence for various flame experiments from the literature. Primarily, the results for OH* from Smith and co-workers [51] in a premixed CH_4/air low-pressure flame were compared with simulations based on the OH* model from the present work.

Figure 4.26 shows the measured OH* concentrations as a function of the height above the burner (HAB) for three different flame stoichiometries from lean to rich conditions. The OH* sub-mechanism developed in the present work from H_2/O_2 and $H_2/O_2/CH_4$ oxidation was implemented. Compared to the experimental observation, the simulated spatial position of the OH* peak concentration is shifted towards the burner surface. Except for the fuel-rich conditions, the experiments show a higher location of the maximum signal of OH* CL. These spatial deviations were also reported by Smith et al. [51] though the reason for these deviations is still unknown. The computed OH*-peak concentrations are underpredicted by up to 60% compared to the experimental data. For the fuel-lean and fuel-rich cases one must consider that the predicted CH concentrations show deviations of about ±25% with regard to the experimentally determined CH concentrations presented by Berg et al. [131]. CH is the most important precursor for OH* chemiluminescence. Therefore, errors in predicting the absolute CH concentration would directly affect the predicted OH* concentration by the same order of magnitude. Hence, when considering the experimental and modeling error limits of ±42% and ±32%, respectively, the discrepancies in the OH* concentrations are covered by the stated errors. Apart from the peak positions, the simulated profiles are thinner than the experiments show. These deviations are attributed to the erroneous OH* concentration based on scaling effects. When normalizing the profiles with respect to their corresponding peak values, there is good agreement between the experiment and simulation.

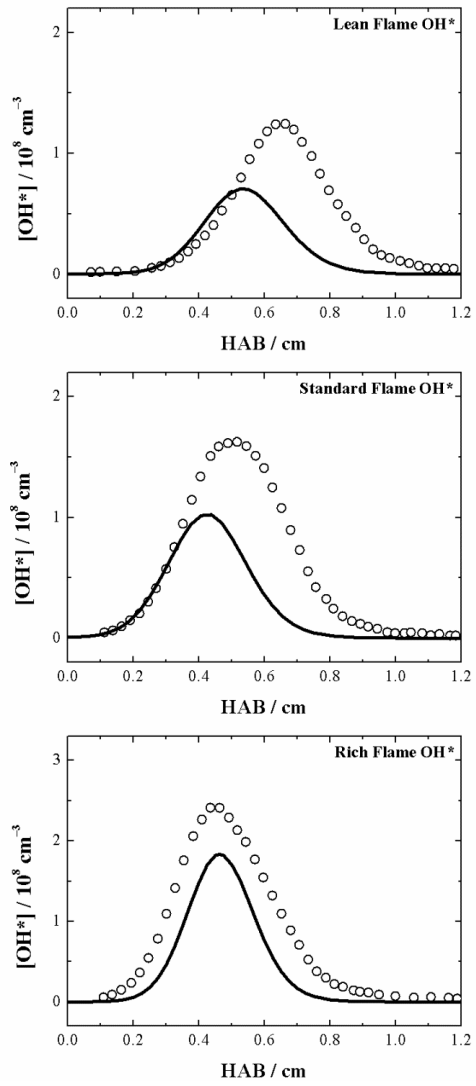

Figure 4.26: Experimental (symbols) and simulated (line) chemiluminescence profiles for OH* for three low-pressure methane-air flames of $\phi = 0.81$, 1.07 and 1.27 adopted from Smith et al. [51].

Recently, Nau and co-workers [63] presented a study of OH*, CH*(A), CH*(B) and C_2* chemiluminescence in two $CH_4/O_2/Ar$ low-pressure flames. Similarly to the approach of Smith et al. [51], they calibrated their detection systems by Raman and Rayleigh scattering and translated measured emission intensities into absolute species concentration. The simulations were done using the CL model from the present work in conjunction with the GRI3.0 ground-state mechanism. Figure 4.27 shows the experimental and the simulated OH* concentrations as a function of the height above the burner. Here also, the computed peak position of OH* chemiluminescence for the stoichiometric case was found to be slightly shifted towards the burner. However, for the fuel-rich case the model can reproduce the spatial position of OH* CL. The profile for the fuel-rich case is in agreement with the experimental data. However, for the stoichiometric case the computed profile is thinner compared to the experimental profiles. Here also, the deviation is owed to the scaling effects previously discussed. This observation was also made by the authors using the reaction mechanism from Kathrotia et al.

[62, 65, 132]. The computed OH* concentration for the stoichiometric condition using the present mechanism is underpredicted by about 30% for the fuel-rich case whereas it is overpredicted by about 30% which is within the experimental and modeling error limits.

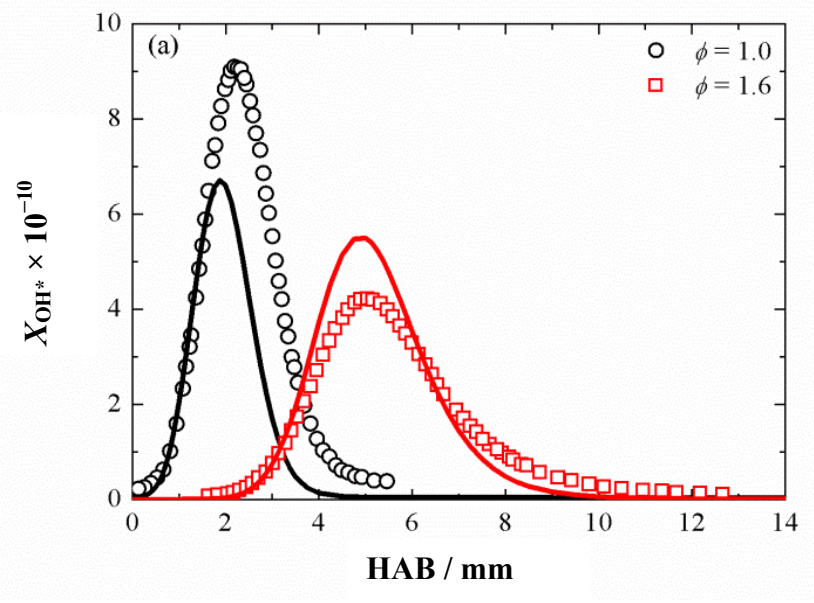

Figure 4.27: Comparison of measured (symbols) and simulated (lines) OH* concentrations for two equivalence ratios. Experimental data adopted from Nau et al. [63].

Kathrotia et al. [65] recently studied the chemiluminescence emission in various methane flames analog with the experiments of Nau and co-workers [63]. Based on the calibration procedure from [63], they converted their measured chemiluminescence into absolute species concentrations for $\phi = 1.0$ and 1.6 and compared the peak concentrations of OH*, CH*(A), CH*(B) and C_2*. Again, the experimental data from [65] were compared with simulations using the chemiluminescence mechanisms from the present study and the GRI3.0 ground-state mechanism. The predicted peak positions of OH* chemiluminescence shown in Figure 4.28, are in agreement with the experimental data. Furthermore, the computed peak concentrations of OH* agree with the measured values well. The exception is the fuel-lean case where the model predicts concentrations that are three times lower. Here again, the computed spatial OH* profiles are found to be thinner than the experimental counterpart shows. Unlike the previous results from Smith et al. [63], these spatial deviations are not attributed to scaling effects, but lower spatial resolution of the experiments are more likely to be responsible for the observed deviations.

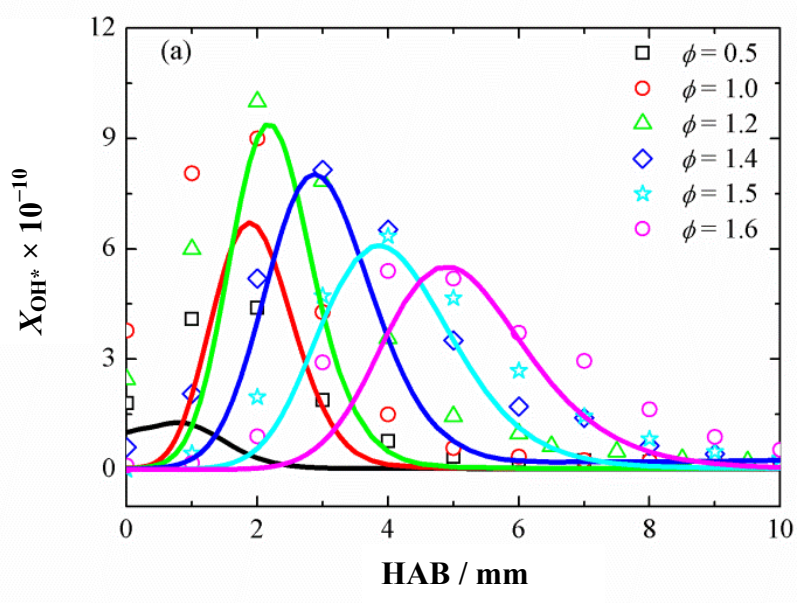

Figure 4.28: Comparison of measured (symbols) and simulated (lines) OH* concentrations for different equivalence ratios. Experimental data adopted from Kathrotia et al. [65].

4.2. Shock-tube measurements of CH* chemiluminescence

CH* chemiluminescence shows three major emission bands. The strongest one is attributed to CH(A) and emits around 431 nm. This transition contributes about 80% of the total CH* emission. The other states CH(B) and CH(C) at around 390 nm and 314 nm, respectively, are much weaker compared to the A–X transition. The B-state typically contributes around 20% to the CH* chemiluminescence, whereas reliable information for the C-state is not given. The present work is devoted to the strongest band at 431 nm.

4.2.1. Review of CH* kinetics

Aside from OH* chemiluminescence, blue-light emission from CH* chemiluminescence is frequently employed for combustion diagnostics under flame [51, 63, 116] and shock-tube conditions [53, 61, 133]. For online measurement of the local equivalence ratio, OH* as well as CH* chemiluminescence are employed at the same time [134-135]. Although CH* CL was extensively studied in various previous works, the formation reactions of CH* emission are still under debate. The present study was devoted for the systematic investigation of CH* key reactions in various hydrocarbon combustion systems. A combined experimental and numerical study was adopted to determine the contribution of the potential formation reactions leading to CH*.

For CH* CL, there is disagreement in identifying the formation reaction(s). The dominating pathway(s) and their suggested rate coefficients from literature also vary by several orders of magnitude. Broida and Gaydon [136] and Bass and Broida [137] identified CH* half a centu-

ry ago. The reaction producing CH* was suggested by Broida and Gaydon [136] and Gaydon [48] as:

$$C_2 + OH = CH^* + CO \qquad (R5)$$

Porter et al. [114] suggested a rate coefficient of (R5) to be 4.2×10^{11} $cm^3mol^{-1}s^{-1}$. Bleekrode and Nieuwpoort [138] derived from CH* lifetimes a range for k_5 between 6.0×10^{11} and 6.0×10^{12} and $cm^3mol^{-1}s^{-1}$. Bulewicz et al. [139] later supported reaction (R5) and derived a rate coefficient of $k_5 = 4.8\times10^{12}$ $cm^3mol^{-1}s^{-1}$ via absorption and emission experiments for various species in a low-pressure burner. Based on their premixed flame experiments, Smith et al. [51] recommended the value $k_5 = 1.1\times10^{13}$ $cm^3mol^{-1}s^{-1}$. They pointed out, however, that reaction (R5) plays only a minor role with a contribution less than 10%. More recently, Hall et al. [53] determined an exceptionally high rate coefficient of $k_5 = 2.0\times10^{14}$ $cm^3mol^{-1}s^{-1}$. Glass et al. [140] rejected also the relevance of reaction (R5) as dominating pathway and introduced the reaction of ethynyl (C_2H) radicals with atomic oxygen. Also Brennen and Carrington [141] and Grebe and Homann [55] privileged the following reaction as the main channel:

$$C_2H + O = CH^* + CO \qquad (R6)$$

Recently, and based on highly-resolved spectroscopic investigations of CH* CL, Brockhinke et al. [64] also excluded the role of (R5) for the formation scheme of CH*. They pointed out that this formation reaction is accompanied by a large excess of free enthalpy ($\Delta_f H$ = 676 kJ mol^{-1}) which would lead to high vibrational states, whereas the measured spectra did not show such effects. Therefore, reactions (R6) and (R7) were favored. Joklik et al. [142] showed in their low-pressure acetylene flame the dominance of the reaction (R6), but suggested a value of $k_6 = 7.0\times10^{12}$ $cm^3mol^{-1}s^{-1}$ which is one order of magnitude higher than the recommended value stated in an earlier work from Grebe and Homann [55]. Reaction (R6) was also supported by Devriendt et al. [143]. They determine the room-temperature rate coefficient by means of a pulsed laser photolysis study of the C_2H_2/N_2O system. The rate coefficient of the reaction (R6) was measured by using NO_2* chemiluminescence from NO + O as reference. The rate coefficient for reaction (R6) was found to be 1.1×10^{13} $cm^3mol^{-1}s^{-1}$. One year later, Devriendt and Peeters [144] presented a study of mixtures containing C_2H_2/O/H using an isothermal flow reactor coupled with molecular-beam-sampling threshold-ionization mass spectrometry (MB-TIMS) to quantify C_2H and oxygen atoms. Again, CH* CL signal intensities were linked to NO_2* CL as internal standard to derive absolute CH* concentrations. They found proportionality between CH* emission intensity and $[C_2H]\times[O]$. Based on this observation, they estimated a revised rate coefficient for $k_6 = 1.4\times10^{13}\exp(-1.9$ kJ $mol^{-1}/RT)$ $cm^3mol^{-1}s^{-1}$. Based on the calibration procedure of the optical detection system described in section 4.1.1, Smith et al. [51] measured a rate coefficient $k_6 = 6.2\times10^{12}$ $cm^3mol^{-1}s^{-1}$ which was considered as the main formation channel leading to CH* in premixed CH_4/air flames. Afterwards, the authors investigated CH* formation in CH_4/N_2O flames in

[112] by using the same calibration procedure stated in [51]. They found, that CH* CL cannot solely be described by reaction (R6) with their recommendation of k_6 in [51]. The CH_4/N_2O flame experiments revealed that a rate coefficient of $k_6 = 2.5\times10^{12}$ $cm^3mol^{-1}s^{-1}$ [112] was required which was slightly lower than their previous recommendation. Based on their shock-tube study where they fitted simulated and normalized CH* concentrations against their experimental data as function of ϕ, Hall et al. [53] estimated a rate coefficient of $k_6 = 5.2\times10^{11}\exp(-10.9\text{ kJ mol}^{-1}/RT)$ $cm^3mol^{-1}s^{-1}$. The study, however, revealed that the main reaction channel was attributed to the reaction (R5). Recently, Elsamra et al. [145] deduced from a pulsed laser photolysis study using He-diluted C_2H_2/O_2 mixtures a value of $k_6 = 6.0\times10^{12}\exp(-1.9\text{ kJ mol}^{-1}/RT)$ $cm^3mol^{-1}s^{-1}$. They considered (R6) as major source of CH* production especially for fuel-rich conditions.

A third CH* formation pathway was proposed in the early 1960s by Hand and Kistiakowsky [146] which was supported by Gutman and Matsuda [50] and Matsuda et al. [147]. They postulate that the reaction of C_2H radicals with O_2 strongly contribute to the production of CH*:

$$C_2H + O_2 = CH^* + CO_2 \qquad \text{(R7)}$$

Other studies were devoted to the investigation of reaction (R7). A laser photolysis study by Renlund et al. [148] favored (R7) as important pathway for CH* formation. Hwang et al. [149] also supported this recommendation and deduced a rate coefficient $k_7 = 4.10\times10^{13}\exp(-4.5\text{ kJ mol}^{-1}/RT)$ $cm^3mol^{-1}s^{-1}$ based on shock-tube investigations. From time-resolved CH* CL after laser photolysis of C_2H_2/N_2O mixtures at room-temperature, Devriendt et al. [143] deduced a rate coefficient $k_7 = 2.2\times10^{10}$ $cm^3mol^{-1}s^{-1}$ which is 500 times lower than their recommendation of k_6. Smith et al. [51] primarily excluded the relevance of (R7) based on their modeling approach for CH_4/O_2 flames. Later on, however, they found out that the model overpredicts the monitored CH* in CH_4/N_2O flames [112] in cases where only reaction (R6) was considered. Hence, they proposed for $k_7 = 3.2\times10^{11}\exp(-6.7\text{ kJ mol}^{-1}/RT)$ $cm^3mol^{-1}s^{-1}$, which was derived from flame experiments with different $[O]/[O_2]$ ratios. Elsamra et al. [145] published a temperature-dependent rate coefficient for (R7) of $6.0\times10^{-4}\,T^{4.4}\exp(9.6\text{ kJ mol}^{-1}/RT)$ $cm^3mol^{-1}s^{-1}$. They denoted the importance of the latter reaction particularly for hot flames under fuel-lean conditions. Recently, Kathrotia [132] quantitatively investigated CH*, OH* and C_2* chemiluminescence in various premixed low-pressure flames. The modeling revealed, that the available rate coefficient k_7 from Elsamra et al. [145] strongly overpredicts the CH* concentration. Depending on the equivalence ratio they revised the recommended rate coefficients for the three potential reaction pathways (R5) – (R7). All these studies pointed out the difficulties in undertaking quantitative measurements. There is a large non-consensus not only in determining the major channel leading to CH* CL in various hydrocarbon systems, but also in providing recommendations of their respective rates. Therefore, the aim of this work was to improve the knowledge of the formation pathways leading to

CH* CL and determining their corresponding kinetics data via linking shock-tube experiments and numerical modeling.

4.2.2. Strategy of the investigation of CH* chemiluminescence

For the investigation of CH* chemiluminescence in hydrocarbon combustion, the well-known acetylene oxidation mechanism (see section 2.2.3) was used to identify the potential formation reactions leading to CH* CL. The combustion of acetylene provides high amounts of C_2H radicals as well as C_2 radicals, which are considered as potential precursors for CH* formation. Therefore, CH* chemiluminescence was initially studied for shock-heated $C_2H_2/O_2/Ar$ mixtures and based on these results, a reaction mechanism describing CH* kinetics was developed and validated. Because of the ambiguity with regard to the importance of the reaction $C_2H + O = CH^* + CO$ vs. $C_2H + O_2 = CH^* + CO_2$, additional experiments with $C_2H_2/N_2O/Ar$ mixtures were performed in order to test the CH* formation for a higher $[O]/[O_2]$ ratios. Aside from the C_2H_2 system, simulations based on the present CH* sub-mechanism were extensively compared to measurements for various C_1 and C_2 hydrocarbons (C_2H_4, CH_4 and C_2H_5OH) for O_2 and N_2O as oxidizers.

In order to extend the validation database of the CH* sub-mechanism from the present work, the model prediction was also tested with regard to flame measurements. For this purpose, additional simulations were done according to recent studies of the CH* formation for various premixed flames reported in literature [51, 63, 65].

4.2.3. CH* chemiluminescence in C_2H_2 mixtures

The acetylene reaction system was extensively studied in the past and thus, a well-validated reaction mechanism (see section 2.2.3) exists which can be used for the modeling of the present shock-tube experiments. The underlying ground-state mechanism originally did not contain formation and consumption reactions of C_2 molecule which is an important precursor for the CH* formation. Therefore, a C_2 sub-mechanism recommended by Williams and Pasternack [150] that consists of 18 reactions was incorporated. We ensured that these modifications did not affect the base mechanism by comparing the original and the extended mechanism with regard to the published validation data for the relevant species (OH and CO_2) and ignition delay times. No further modifications were done. To our knowledge, an acetylene ground-state mechanism which is validated for the oxidation with O_2 and N_2O does not exist so far. Therefore, the base mechanism was extended by an additional subset of NO_x reactions adopted from the GRI 3.0 mechanism [92] in order to reproduce the shock-tube experiments with N_2O as oxidizer. This additional nitrogen chemistry was originally implemented in a methane-combustion mechanism [92] and therefore contains cross-reactions linking nitrogen

with hydrocarbon chemistry. The formation of CH* was studied in various shock-heated C_2H_2-based mixtures (see Table 4.4).

A typical temporal variation of a normalized CH*-CL signal for argon-diluted C_2H_2/O_2 mixtures is shown in Figure 4.29. After an induction time, the CH* emission increases, reaches its maximum and afterwards decays. The temporal shape of the CH* concentration is well reproduced by the simulation using the present rate coefficients k_5 and k_6. Overall, good agreement of the temperature dependence, of the CH*-CL intensities and peak times (Figure 4.30), the CH* signal reduction for lean mixtures (Figure 4.31), and the temporal variation of the CH* emission was obtained for a wide range of conditions and for all four investigated equivalence ratios. When changing the present rate coefficients k_5 and k_6 by a factor of 2 and 0.5, respectively, the CH* peak concentration varies around by ±30%.

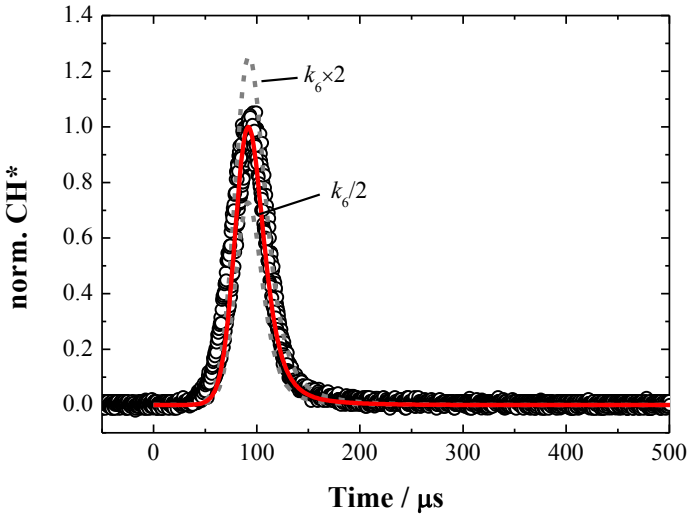

Figure 4.29: Comparison of the temporal variation of the normalized CH* chemiluminescence (symbols) and the CH* concentration (solid line) simulated with k_5 and k_6 from the present work. The dotted lines represent the modeled CH* traces for variations of k_6 by a factor of 2. The mixture composition is 0.10% C_2H_2 and 0.33% O_2 diluted in Ar at T_5 = 2300 K and p_5 = 1.32 bar.

Figure 4.30a shows the comparison of typical normalized CH* peak intensities from the experiment and simulated CH* peak concentrations. The data were normalized with respect to the corresponding value at the reference temperature of T_5 = 1900 K. The corresponding measured and simulated peak times are shown in Figure 4.30b. The CH* peak intensities increase exponentially with temperature, while the peak times show an opposed effect; namely the induction time decreases for increasing temperatures. This temperature dependence of CH* chemiluminescence can be observed for all equivalence ratios.

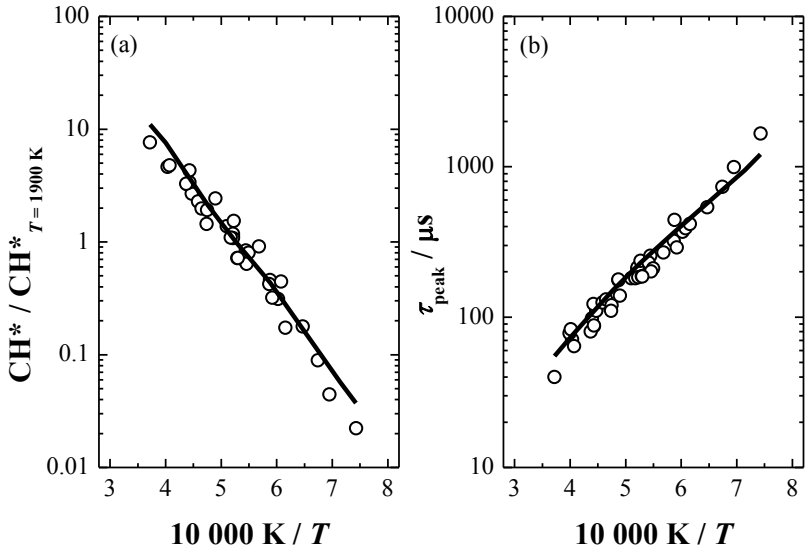

Figure 4.30: Measurement (symbols) and simulation (lines) of (a) CH* chemiluminescence intensities normalized to the corresponding value at T = 1900 K and (b) delay times for peak CH* for mixture 8.

In order to show the importance of the different pathways forming the chemiluminescence intensities (R5) – (R7), the data was evaluated by normalizing the CH*-CL intensities for lean conditions with respect to the corresponding values of the stoichiometric mixtures. These data are plotted for three different temperatures as a function of the equivalence ratio. Overall, the normalized intensities decrease with increasing O_2 concentration (cf. Figure 4.31), in particular for high temperatures, which was used to separate the impact of the three formation reactions. This effect was already stated by Hall and co-workers [53] in an earlier CH_4/O_2 shock-tube study. They observed the decrease of CH* for fuel-lean CH_4/O_2/Ar mixtures and concluded that it was impossible to match the CH* reduction with their kinetics model if the reaction $C_2H + O_2 = CH^* + CO_2$ (R7) was involved. Based on our modeling, we agree with this conclusion, because our model cannot reproduce the decreasing CH* CL in the presence of (R7). If the formation reaction of CH* via (R7) with a rate coefficient larger than 1.0×10^{11} cm^{3}mol^{-1}s^{-1} is incorporated, the CH* CL linearly increases with increasing O_2 concentration (cf. Figure 4.31), which is not consistent with our experimental observations. Furthermore, the experimental CH* peak times were slightly underpredicted when taking (R7) into account (not shown here for the sake of brevity). Generally, the kinetics model involving reactions (R6) and (R7) produced more CH* for higher O_2 concentrations. Our model revealed, that only reaction $C_2 + OH = CH^* + CO$ (R5) can account for this reduction behavior of CH* for higher O_2 fractions.

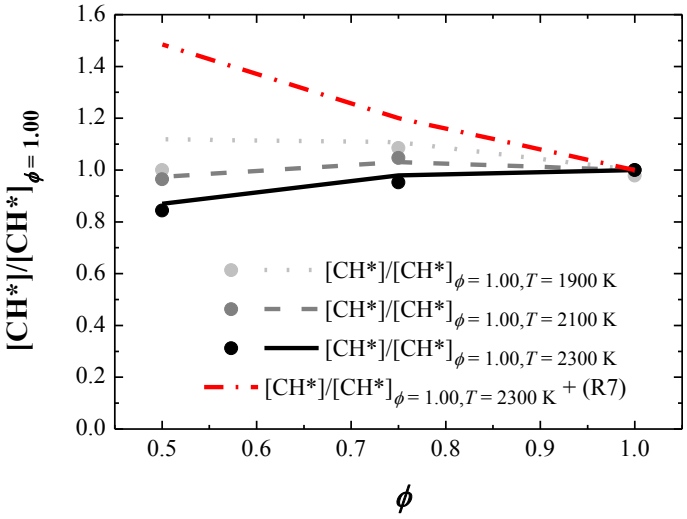

Figure 4.31: Experimental (symbols) and simulated (lines) CH* chemiluminescence normalized to the corresponding value at $\phi = 1.00$ for three different temperatures in C_2H_2, O_2, Ar mixtures. The dash-dotted line represents the modeling results when additionally incorporating reaction (R7) with the rate coefficient of 1.0×10^{11} $cm^3mol^{-1}s^{-1}$.

Neglecting the formation reaction of CH* via $C_2H + O_2 = CH^* + CO_2$ (R7) had not been considered in other recent studies except the study from Hall et al. [53]. Therefore, an extensive evaluation of the relevance of reaction (R7) was required. For this purpose, additional simulations using the CH* sub-mechanism from the present study (cf. Table 4.11) assuming (R7) with recent literature values for k_7 were performed. With the most recent rate coefficient for k_7 from Elsamra et al. [145], the reduction of the CH* CL as function of equivalence ratio seen in Figure 4.31, cannot be predicted by the model and the main chemiluminescence formation becomes controlled by (R7) which is again in contradiction with the recent study from Kathrotia et al. [65]. They observed an eightfold overprediction of CH* CL especially for fuel-rich conditions when considering the rate coefficient from Elsamra et al. [145] whereas better agreement was found when considering (R5) and (R6).

In cases when considering the corresponding rate coefficient k_7 from Devriendt et al. [143], which is about one order of magnitude lower compared to the value from [145], the simulations show a slight reduction of CH* CL for excess of O_2. However, this signal reduction is not as pronounced as in the experiments. With the values from Devriendt et al. [143], good agreement between the simulated and the measured dependence on the equivalence ratio was achieved when the rate coefficient of the quenching reaction $CH^* + O_2 = CH + O_2$ (R9,1) was multiplied by a factor of two which compensates for the slow rate of Devriendt. However, Tamura et al. [68] stated an error limit of ±15% for the corresponding quenching rate. Therefore, the given rate coefficients k_7 are still too high to account for our experimental results. Recently, Kathrotia et al. [65] also pointed out the overprediction of CH* CL when considering the available rate coefficient of k_7 from Devriendt [143].

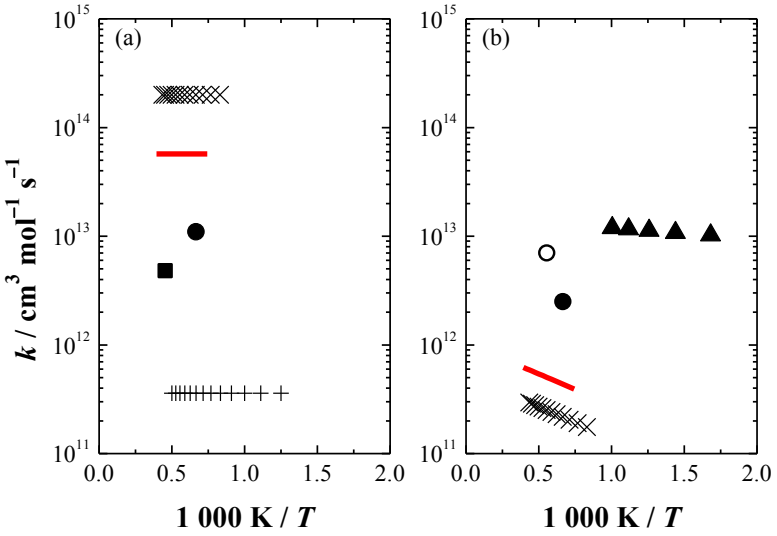

Figure 4.32: Arrhenius plot of the rate coefficients for the reaction (a) C_2 + OH = CH* + CO (R5) and (b) C_2H + O = CH* + CO (R6). Symbols: ○ Joklik et al. [142]; ● Smith et al. [51]; ▲ Devriendt et al. [143-144]; ■ Bulewicz et al. [139]; + Porter et al. [114]; × Hall et al. [53]. Red lines: present work.

The starting values for the rate coefficients k_5 and k_6 were taken from Hall et al. [53]. However, our modeling could not reproduce the temperature dependence of the normalized CH* CL with regard to the shock-tube experiments and the absolute CH* concentration in the flame experiments from [51, 63, 65] when considering the original values from [53]. Therefore, the corresponding rate coefficients k_5 and k_6 were varied with respect to our experimental data. The best correlation between measurement and simulation can be obtained with $k_5 = 5.7\times10^{13}$ cm^{3}mol^{-1}s^{-1} and $k_6 = 1.0\times10^{12}$ exp(−10.9 kJ mol^{-1}/RT) cm^{3}mol^{-1}s^{-1}. Figure 4.32 shows a summary of rate coefficients for the two reactions (R5) and (R6). The rate coefficients for both reactions are close to the initial values from Hall and co-workers [53]. The errors in determining the rate coefficients k_5 and k_6 are estimated to be ±53%.

Acetylene provides high amounts of C_2H via chain-branching reactions which directly leads to CH* CL via (R6) C_2H + O = CH* + CO. The main fraction of C_2H, however, further reacts to C_2 which forms CH* CL from (R5) C_2 + OH = CH* + CO. The rate-of-production (ROP) analysis shown in Figure 4.33 reveals that one-third to half of the CH* formation is attributed to the reaction (R6) whereas the residue is contributed by reaction (R5). The peak position is mainly determined by the reaction (R5) and is in agreement with the measured peak positions τ_{exp} (cf. Figure 4.33). CH* is mainly consumed via collisional quenching with CO and Ar and radiative decay, while other quenching reactions are of minor importance.

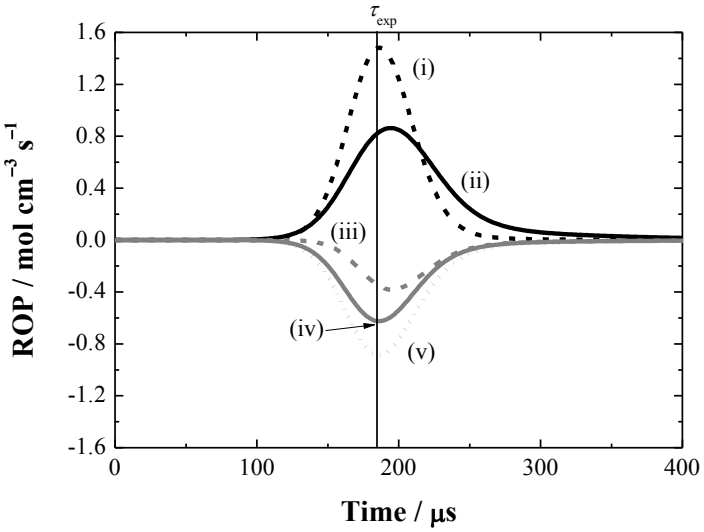

Figure 4.33: Rate-of-production analysis of the CH* formation for mixture 9 at T_5 = 1900 K and p_5 = 1.32 bar. Formation reaction is attributed to (i) C_2 + OH = CH* + CO and (ii) C_2H + O = CH* + CO. Main quenching reactions are identified as (iii) CH* + CO = CH + CO, (iv) CH* = CH + *hv*, (v) CH* + Ar = CH + Ar. The experimental temporal peak location of CH* is illustrated by a vertical line.

To further verify the relative importance of (R6) vs. (R7), CH* CL was investigated by changing the O/O_2 ratio using N_2O-blending to the mixture. For this purpose, the acetylene-oxidation and chemiluminescence model was upgraded by an additional subset of NO_x chemistry described in section 2.2.3. It was ensured that the NO_x chemistry did not influence the predictions of the ground-state chemistry for C_2H_2/O_2-containing mixtures.

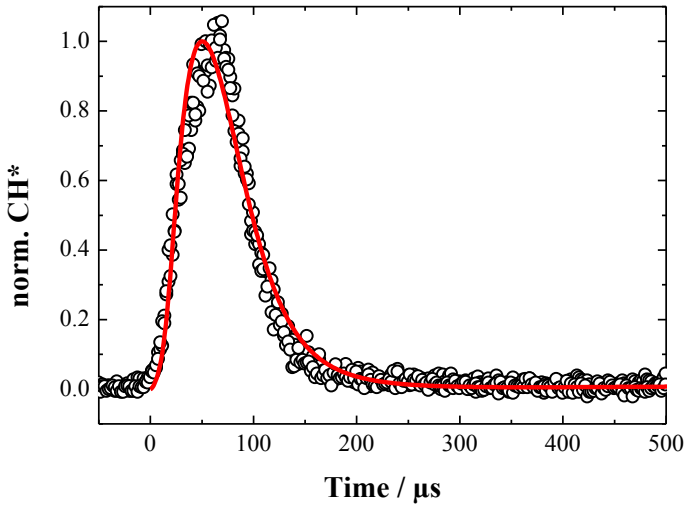

Figure 4.34: Comparison of the temporal variation of the normalized CH* chemiluminescence (symbols) and the CH* concentration (line) simulated with the rate coefficients k_5 and k_6 from this work. The mixture composition is 13 at T_5 = 1900 K and p_5 = 1.32 bar.

The chemical formation pathway of CH* chemiluminescence in the N_2O-based mixtures proceeds similar to the formation of CH* in mixtures with O_2. The temporal variation of the CH*-CL emission is shown in Figure 4.34. CH* is formed quasi instantaneously behind the reflected shock wave. Analogously to the formation of OH* chemiluminescence in mixtures

with N_2O, the CH* rise is faster than its removal. In particular, the CL signal has its peak maximum at 50 µs, whereas CH* reaches its zero-level within 150 µs at this conditions. Overall, the experiments show a significantly faster ignition delay and peak time compared to mixtures with molecular oxygen.

The temperature dependence of the normalized chemiluminescence intensities (a) and peak times (b) are illustrated for fuel-lean mixtures in Figure 4.35. At high temperatures, the predicted temperature dependence of the normalized chemiluminescence intensities deviate with regard to the experiments, particularly the computed temperature behavior is stronger than the experiments show. As it can be seen also for OH* chemiluminescence in various N_2O-based mixtures, in some cases the simulated peak times tend to be faster than the measured one. This disagreement was already discussed for OH* CL and is mainly attributed to an erroneous representation of the ground-state chemistry with N_2O. Overall, there is agreement for the temperature dependence between the experimental data and model predictions.

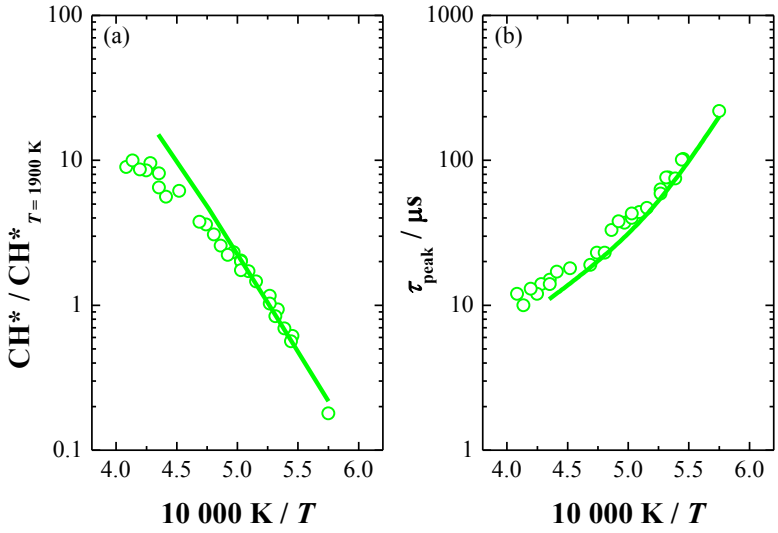

Figure 4.35: Measurement (symbols) and simulation (lines) of (a) CH* chemiluminescence intensities normalized to the corresponding value at T_5 = 1900 K and (b) peak times of CH* for mixture 13.

To represent the experimental and the model predictions for other conditions, the activation energy E_a of the normalized CH* CL intensities and peak times is plotted as a function of ϕ in Figure 4.36. Analog to the approach presented for OH* CL, the temperature-dependent intensities and ignition delay times were described empirically by an Arrhenius-like equation $CL/CL_{T=1900K} = A\times\exp(-E_a/RT)$ and $\tau = A\times\exp(-E_a/RT)$, respectively. CH* chemiluminescence shows a strong temperature dependence of the CL intensities and peak times. Compared to the experiments with C_2H_2/O_2 (activation energy E_a = 100 – 150 kJ mol^{-1}), the temperature dependence for the CH* intensities is stronger for mixtures with N_2O (activation energy E_a = 210 kJ mol^{-1}). The model-predicted activation energy for the peak times for N_2O-based mixtures is 100% higher than for the O_2 case.

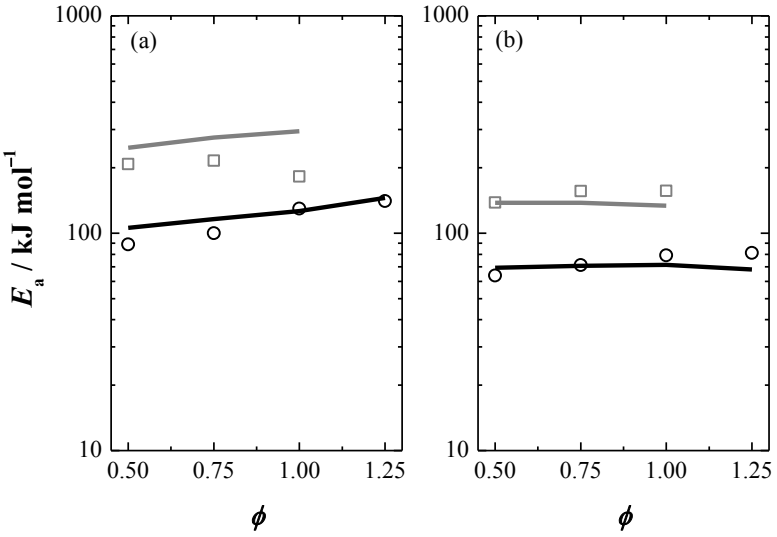

Figure 4.36: Measured (symbols) and simulated (lines) activation energy E_a of (a) CH* intensities and (b) CH* peak times as a function of equivalence ratio ϕ. The open circles and black lines represent the C_2H_2/O_2 mixtures (7 – 10) and the open squares and grey lines represent the C_2H_2/N_2O mixtures (11 – 13).

The present work solely considers relative CH* intensities and their corresponding computed concentrations due to the lack of a suitable CH* calibration procedure under shock-tube conditions. Because OH* concentrations were accurately predicted for a wide range of conditions in various shock-heated acetylene mixtures, the correlation of OH* and CH* chemiluminescence intensities that were measured, respectively, was used to further verify the rate coefficients k_5 and k_6. CH* chemiluminescence was simulated by using the present submechanism with respect to the formation reactions (R5) – (R7) and their corresponding rate coefficients adopted from various authors while for all simulations the same quenching reactions were used. The OH* chemiluminescence was consistently simulated using the submechanism from the present work for all cases while modifications in the rate coefficients were done only for the CH* subset.

The correlation of OH* and CH* intensity and concentration is given by the equation $I_{OH^*} = C_{OH^*} \times [OH^*]$ and $I_{CH^*} = C_{CH^*} \times [CH^*]$, respectively, where C_i is a calibration constant incorporating the properties of the optical setup and the spectroscopic properties of the excited state. In the present study, the optical setup was kept constant within the entire experimental series. When comparing the measured ratio of I_{OH^*}/I_{CH^*} and the simulated ratio of [OH*]/[CH*] for two different experimental conditions, the constants ratio of C_{OH^*} and C_{CH^*} is assumed to be equal to 1 and one can get a direct correlation of measured intensities and simulated concentrations which can be used to verify the predicted CH* concentrations based on the well-known OH* concentrations.

Figure 4.37 exemplarily shows the simulated [OH*]/[CH*] ratios as a function of temperature. Primarily, the OH* and CH* concentrations were predicted using the corresponding rate coefficients from this work. There is good agreement between the experimental (open circles)

and the calculated (solid line) data for a wide temperature range which can be observed for all equivalence ratios. Based on the validated absolute OH* concentrations, these results indicate that the predicted CH* concentrations match the experiments fairly well with the adopted k_5 and k_6 rate coefficients. However, some discrepancies still exist within the temperature range. Additionally, CH* concentrations were calculated using the recommendations from literature (see symbols and lines in Figure 4.37). Similar to the present work, Smith et al. [51] and Hall and co-workers [53] favored reactions (R5) and (R6) as potential formation reactions. However, their suggested rate coefficients for the corresponding reactions are higher compared to the recommendations in the present work which causes an overprediction of CH* CL and thus, to an underestimation of the ratio it can be seen in the Figure 4.37.

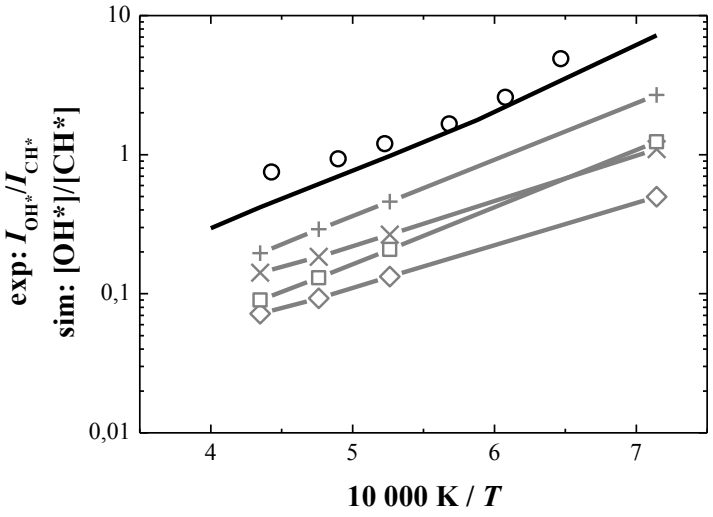

Figure 4.37: Experimental (open circles) and simulated (black line) OH*/CH* intensities and concentrations ratios for mixture 8 from the present work. Symbols and lines are representing the results using recommendations for the reactions (R5) – (R7) and their corresponding rate coefficients k_5 – k_7 from: + Hall et al. [53], × Smith et al. [51], □ Elsamra et al. [145] and ◊ Devriendt et al. [143-144].

To verify the importance of reactions (R5) $C_2 + OH = CH^* + CO$ and (R6) $C_2H + O = CH^* + CO$ versus (R7) $C_2H + O_2 = CH^* + CO_2$, additional simulations were performed considering the suggestions from Devriendt et al. [143-144] and Elsamra et al. [145]. These authors favored reactions (R6) and (R7) as potential pathways leading to CH* chemiluminescence instead of (R5). When comparing the simulation results using these two formation reactions and their corresponding rate coefficients, the underprediciton of the OH*/CH* ratio is more distinct. The discrepancy between experimental and simulated results increases up to one order of magnitude. According to our observations in Figure 4.31 in conjunction with the results from Kathrotia et al. [65], reaction (R7) $C_2H + O_2 = CH^* + CO_2$ leads to a significant overprediction of CH* chemiluminescence. Therefore, it is appropriate to exclude this reaction from the CH* mechanism. Best agreement between experiments and simulations can be observed considering the recommendations from the present work.

Table 4.9: Experimental and simulated OH* and CH* peak concentrations and their relative errors δ for mixture 8.

T / K	1900	2100	2300	Source
[OH*][1]	3.59×10^{-15}	5.25×10^{-15}	7.37×10^{-15}	Experiment
[CH*][1]	3.02×10^{-15}	6.10×10^{-15}	9.96×10^{-15}	[CH*] = [OH*]×I_{CH*}/I_{OH*}
I_{OH*}/I_{CH*}	1.19	0.86	0.74	Experiment
[OH*][1]	2.96×10^{-15}	3.99×10^{-15}	5.49×10^{-15}	Simulations with k_5 and k_6 from the present work
$\delta_{[OH*]}$	–18%	–24%	–26%	
[CH*][1]	3.03×10^{-15}	6.50×10^{-15}	1.31×10^{-14}	
$\delta_{[CH*]}$	+1%	+7%	+32%	
[OH*]/[CH*]	0.98	0.61	0.42	
[CH*][1]	1.11×10^{-14}	2.16×10^{-14}	3.87×10^{-14}	Simulations with k_5 and k_6 from Smith et al. [51]
$\delta_{[CH*]}$	+268%	+254%	+289%	
[OH*]/[CH*]	0.27	0.18	0.14	
[CH*][1]	6.44×10^{-15}	1.37×10^{-14}	2.80×10^{-14}	Simulations with k_5 and k_6 from Hall et al. [53]
$\delta_{[CH*]}$	+113%	+125%	+181%	
[OH*]/[CH*]	0.46	0.29	0.20	
[CH*][1]	2.23×10^{-14}	4.30×10^{-14}	7.64×10^{-14}	Simulations with k_6 and k_7 from Devriendt et al. [143-144]
$\delta_{[CH*]}$	+638%	+605%	+667%	
[OH*]/[CH*]	0.13	0.09	0.07	
[CH*][1]	1.42×10^{-14}	3.07×10^{-14}	6.10×10^{-14}	Simulations with k_6 and k_7 from Elsamra et al. [145]
$\delta_{[CH*]}$	+370%	+403%	+512%	
[OH*]/[CH*]	0.21	0.13	0.09	

[1]unit: mol cm^{-3}

The entire OH* and CH* concentrations for the OH*/CH* ratio evaluation discussed above are tabulated in Table 4.9. The model, considering rate coefficients k_5 and k_6 from the present work, predicts CH* concentrations within the error limits derived from the OH* and CH* ratio, whereas the values based on the rate coefficients k_5 – k_7 adopted from various studies show significant overprediction which is beyond the error limits reported in the present study.

Further validation of the chemiluminescence sub-mechanism was done with regard to laminar flame experiments from the literature presented in section 4.2.8 which provide spatially resolved CH* concentrations.

Overall, the CH* kinetics model developed in this study accurately predicts the *T*-dependence of the normalized CL intensities (Figure 4.36a) and the peak times (Figure 4.36b) for O_2-based mixtures. There is good agreement in absolute peak times for CH* CL (cf. Figure 4.35). The C_2H_2 oxidation model was extended by a separate NO_x subset as described in section 2.2.3.When considering the ground-state and CH* kinetics mechanisms for the C_2H_2/N_2O/Ar cases, discrepancies occur in predicting the temperature dependence of the CH* chemiluminescence and the peak times. These deviations are mainly attributed to the interaction of the acetylene ground-state model and the implemented NO_x model, since the NO_x mechanism is originally implemented in a CH_4 combustion model and it is not validated for acetylene combustion. However, the CH* formation in N_2O-based mixtures can be reproduced by trend using the present model. Further validation of the ground-state chemistry involving the NO_x mechanism is still required to improve the accuracy of the model especially for combustion mixtures with N_2O as oxidant.

4.2.4. CH* chemiluminescence in C_2H_4 systems

The reliability of the CH* sub-mechanism previously developed was additionally checked for C_2H_4 (experimental conditions are listed in Table 4.5). The ground-state model and the developed CH* kinetics data were kept invariant. The experimental and the computed results were compared and are briefly discussed below.

The reaction pathways of C_2H_4 are in principle similar to the acetylene case described in the previous section. The main difference is attributed to the initial chain-branching reactions from ethylene via vinyl radicals (C_2H_3) towards acetylene. The following formation reactions towards C_2H and C_2 radicals and their process to CH* are analogous to the previous acetylene experiments reported in the previous section.

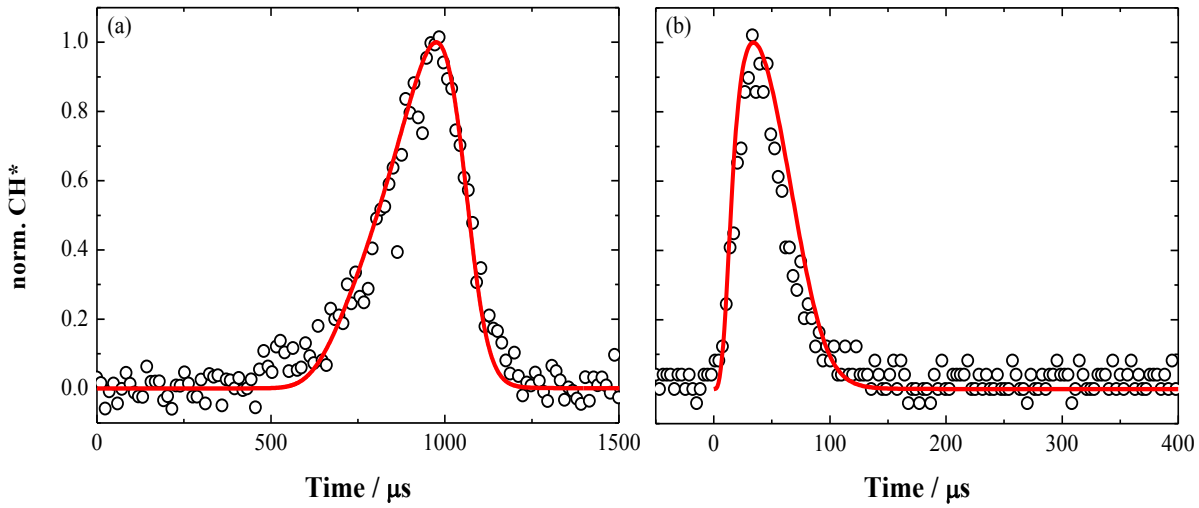

Figure 4.38: Comparison of the temporal variation of the normalized CH* chemiluminescence (symbols) and the CH* concentration (line) simulated with the rate coefficients k_5 and k_6 from this work. (a) Results for a C_2H_4/O_2/Ar mixture 15 at T_5 = 1400 K and p_5 = 1.90 bar. (b) Results for a C_2H_4/N_2O/Ar mixture 18 at T_5 = 2100 K and p_5 = 1.90 bar.

Typical concentration-time histories of the normalized CH* chemiluminescence for Ar-diluted C_2H_4/O_2 and C_2H_4/N_2O mixtures are shown in Figure 4.38. There is good agreement between the experimental and the simulated profiles at the peak position and the formation and decay behavior of the CH* traces for both oxidizers. In agreement with the previous results, CH* signal in N_2O-based mixtures instantaneously forms and thus, shows significantly lower peak times compared to the O_2 case.

The normalized CH* chemiluminescence intensities and the corresponding peak times as function of inverse temperature are illustrated in Figure 4.39. Here again a good correlation between the measurements and the simulations was found for normalized CH* CL and the corresponding peak times for C_2H_4/O_2/Ar mixtures. Both values can be accurately predicted by means of the present CH* kinetics mechanism for O_2- and N_2O-based mixtures, for all studied equivalence ratios and within the entire temperature range that is also reflected in the good consensus between measured and computed activation energies seen in Figure 4.40. The temperature dependence of the chemiluminescence in C_2H_4-based mixtures is comparable to those with C_2H_2 mixture, whereas the CH* CL shows faster peak times for the ethylene mixtures. This was already observed for OH* where peak times for ethylene mixtures are lower compared to the acetylene data due to higher radical pool concentrations attributed to the additional hydrogen atoms in ethylene.

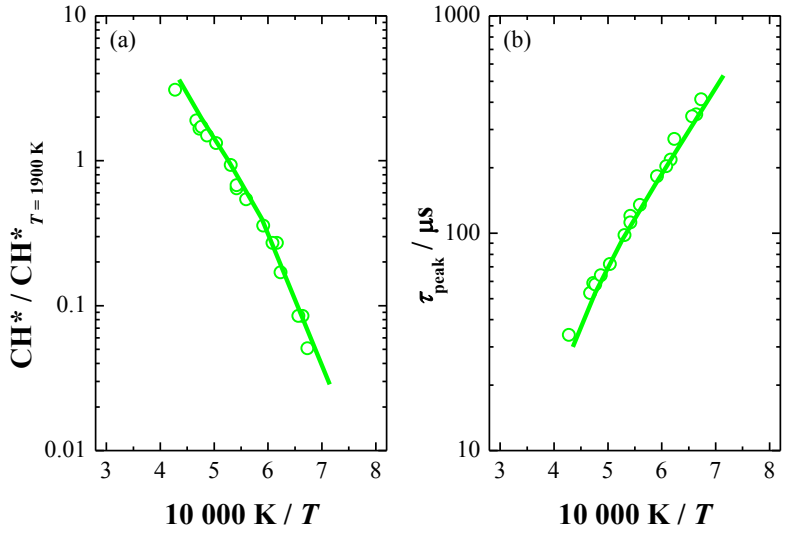

Figure 4.39: Measurement (symbols) and simulation (lines) of (a) CH* chemiluminescence intensities normalized to the corresponding value at T_5 = 1900 K and T_5 = 1.9 bar. (b) delay times for peak CH* for mixture 17.

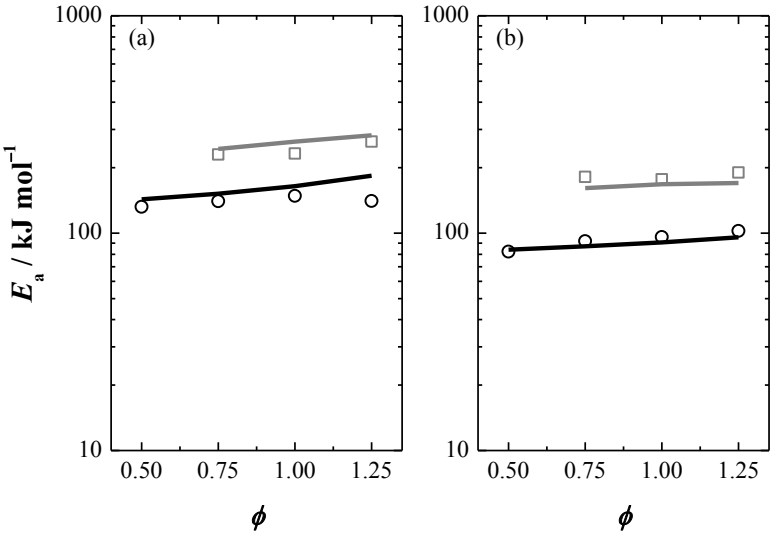

Figure 4.40: Measured (symbols) and simulated (lines) activation energy E_a of (a) CH* intensities and (b) CH* peak times as a function of equivalence ratio ϕ. The open circles and black lines represent the $C_2H_4/O_2/Ar$ mixtures (14 – 17) and the open squares and grey lines represent the $C_2H_4/N_2O/Ar$ mixtures (18 – 20).

For, additional validation of the predicted CH* concentrations, the ratio of measured OH* and CH* intensities are compared with the calculated concentrations for a lean $C_2H_4/O_2/Ar$ mixture shown in Figure 4.41. There is good agreement of experimental and simulated data for temperatures below 1800 K. However, discrepancies occur at higher temperatures where the experimental data show lower temperature dependence compared to the simulations. Additionally, the ratio of simulated OH* and CH* concentrations for different rate coefficients from literature were evaluated. According to the evaluation of the $C_2H_2/O_2/Ar$ system shown in Figure 4.37, the OH* and CH* ratio was determined by using different literature values for k_5 – k_7. The temperature dependent ratio based on simulations using the rate coefficients k_5

and k_6 from Hall et al. [53] and from Smith et al. [51] is underpredicted by a factor of two and up to one order of magnitude, respectively. The results using the recommendations from Devriendt et al. [143-144] and Elsamra [145] incorporating reactions (R6) and (R7) and neglecting (R5) strongly underestimate the experimental results. Depending on the temperature, the error is more than one order of magnitude. The best agreement between experimental and computed results was found here again when using the reactions (R5) and (R6) and the rate coefficients from the present work.

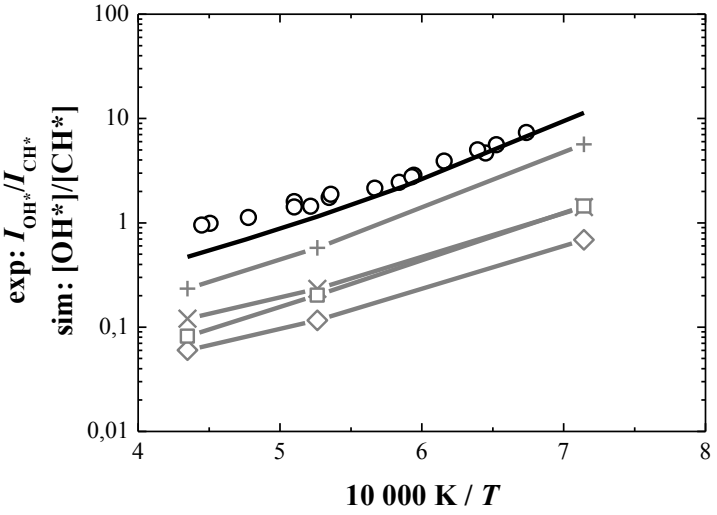

Figure 4.41: Experimental (open circles) and simulated (black line) OH*/CH* intensities and concentrations ratios for mixture 16 from the present work. Symbols and lines are representing the results using recommendations for the reactions (R5) – (R7) and their corresponding rate coefficients k_5 – k_7 from: + Hall et al. [53], × Smith et al. [53], □ Elsamra et al. [145] and ◊ Devriendt et al. [143-144].

4.2.5. CH* chemiluminescence in CH_4 systems

The formation of CH* chemiluminescence was studied in various shock-heated methane mixtures (see Table 4.3). GRI3.0 mechanism was used to simulate the time-resolved CH* concentration for the corresponding experimental conditions. Because of the missing reactions involving C_2 molecules, the C_2 sub-set for from Williams and Pasternack [150] was implemented to the GRI3.0 mechanism [27]. This procedure was already described for the simulations of CH* in acetylene and ethylene combustion.

Recently, Wagner and co-workers [151] directly measured spatially-resolved absolute C_2H_2 concentrations in various laminar premixed CH_4/air flames by means of tunable diode laser absorption spectroscopy (TDLAS) which is an important intermediate for chemiluminescence-relevant C_2 and C_2H molecules. Kathrotia et al. [65] compared these results with simulations based on the GRI3.0 mechanism and found out that the peak concentration as well as the peak position of C_2H_2 can be predicted fairly well. These results indicate that the model should be capable to provide accurate concentrations of the chemiluminescent precursors C_2 and C_2H. However, direct measurements of these latter species would signifi-

cantly improve the accuracy of the chemiluminescence formation reactions. The ground-state mechanism already contains NO_x chemistry. Thus, no changes were done in the mechanism in order to simulate N_2O-based mixtures. The CH* sub-mechanism from the present work was also implemented. According to the previous strategy for the evaluation of the CH* profiles, time-resolved CH* chemiluminescence was normalized the peak maximum and the temperature dependent data were normalized with regard to the value at T_5 = 1900 K.

Figure 4.42 shows typical time-resolved CH* chemiluminescence intensity profile for CH_4/O_2/Ar and CH_4/N_2O/Ar mixtures at comparable conditions. For the O_2 case, the CH* formation starts with a delay time depending on the experimental conditions. In this specific case, the induction time is around 50 µs, the signal peaks at 100 µs. The computed CH* profile shows a deviation in the peak location of less than 10%. While for the N_2O case, the experiment again does not show an induction time. Overall, the model can accurately predict the profile shape and the peak position of CH* chemiluminescence within the experimental temperature range.

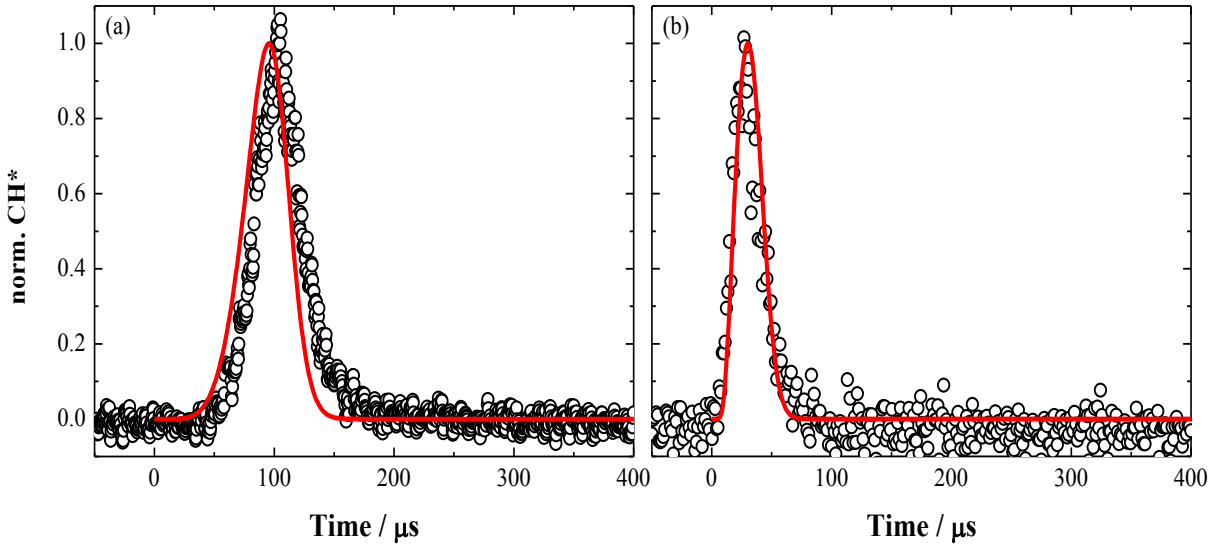

Figure 4.42: Comparison of the temporal variation of the normalized CH* chemiluminescence intensity (symbols) and the CH* concentration (line) simulated with the rate coefficients k_5 and k_6 from this work. (a) Results for a CH_4/O_2/Ar mixture 2. (b) Results for a CH_4/N_2O/Ar mixture 5. Both experiments are conducted at T_5 = 2300 K and p_5 = 1.90 bar.

The results of the temperature dependence for $\phi = 1.00$ and $1837\ \mathrm{K} \leq T \leq 2440\ \mathrm{K}$ around 1.9 bar are summarized in Figure 4.43. The normalized chemiluminescence intensities and concentrations (shown in Figure 4.43a) are in good agreement for stoichiometric conditions. There are small deviations in the predicted slope for higher temperatures. The corresponding peak times as a function of inverse temperature (shown in Figure 4.43b) are very low compared to the values for comparable Ar-diluted CH_4/O_2 mixtures (not shown here). Overall, there is good agreement between experimental and simulated temperature dependence for both values.

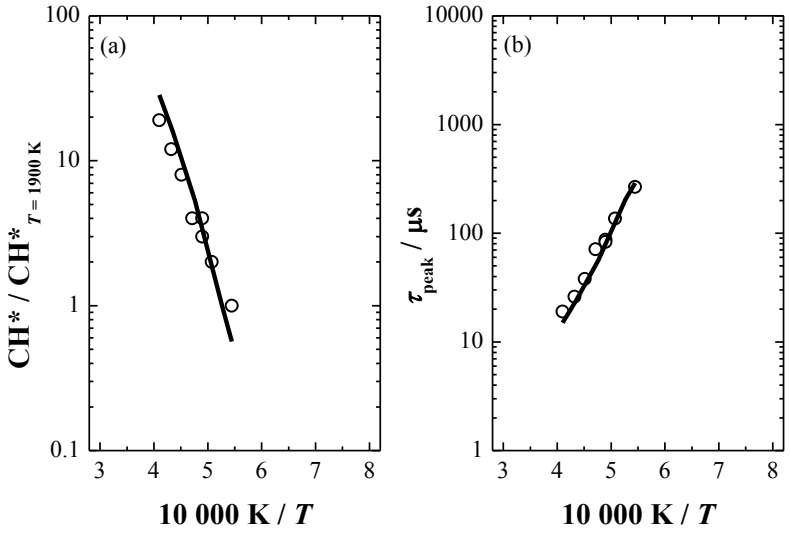

Figure 4.43: Measurement (symbols) and simulation (lines) of (a) CH* chemiluminescence intensities normalized to the corresponding value at T_5 = 1900 K and (b) delay times for peak CH* for mixture 5.

The good concordance between experiment and model is reflected in Figure 4.44 where the measured activation energy are compared for various equivalence ratios for O_2- and N_2O-based CH_4 mixtures. In contrast to the results for other hydrocarbon where the activation energies of O_2-based mixtures have less than half of the corresponding values for N_2O-based mixtures, the activation energies for O_2- and N_2O-containing mixtures have the same values around 200 kJ mol^{-1}.

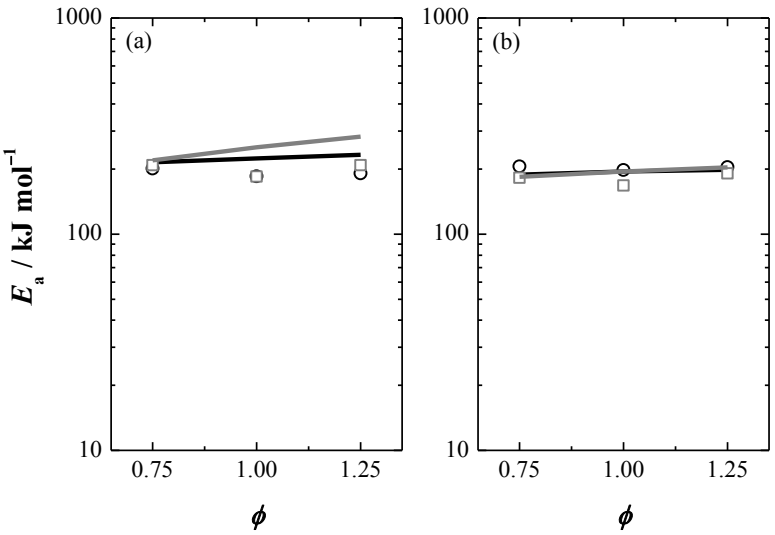

Figure 4.44: Measured (symbols) and simulated (lines) activation energy E_a of (a) CH* intensities and (b) CH* peak times as a function of equivalence ratio ϕ. The open circles and black lines represent the CH_4/O_2/Ar mixtures (1 – 3) and the open squares and grey lines represent the CH_4/N_2O/Ar mixtures (4 – 5).

The ratio of OH* and CH* concentrations from the present work were related to the ratio of the emission intensities of both chemiluminescent species as function of the inverse temperature (see Figure 4.45). The simulated ratio of OH* and CH* is underpredicted especially for

higher temperatures. However, when comparing the results for literature values from different groups, best agreement can be achieved with the recommendations from the present work. The OH* concentration can be accurately predicted especially for CH_4-based mixtures which indicates that the discrepancy of the ratio is mainly attributed to errors in the computed CH* concentrations.

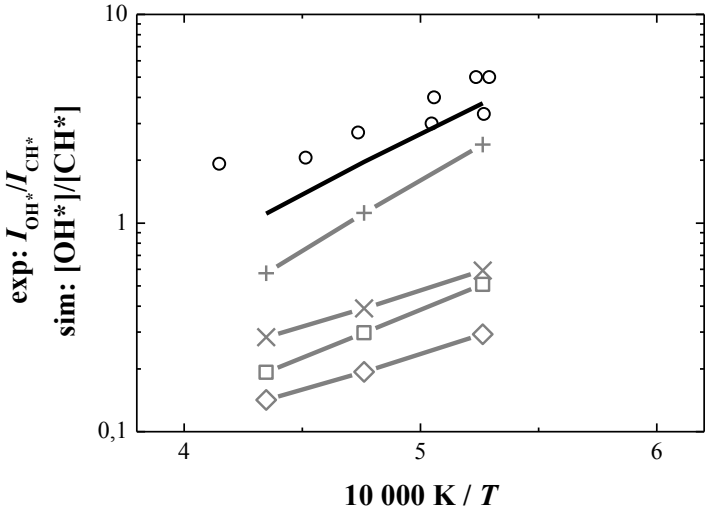

Figure 4.45: Experimental (open circles) and simulated (black line) OH*/CH* intensities and concentrations ratios for mixture 3 from the present work. Symbols and lines are representing the results using recommendations for the reactions (R5) – (R7) and their corresponding rate coefficients k_5 – k_7 from: + Hall et al. [53], × Smith et al. [51], □ Elsamra et al. [145] and ◊ Devriendt et al. [143-144].

Although the CH_4 oxidation mechanism is not explicitly validated for C_2H and in addition, it originally did not consider reactions involving C_2 species, the performance of the modified ground-state mechanism (details are given in section 2.2.2) in conjunction with the CH* kinetics model derived based on the present C_2H_2 shock-tube experiments is satisfying. However, further improvement of the model is required, especially with regard to the temporal occurrence of the chemiluminescent relevant precursor species C_2 and C_2H and their corresponding concentrations.

4.2.6. CH* chemiluminescence in C_2H_5OH systems

For further investigation of the developed CH* sub-mechanism in more complex reaction systems, ethanol was chosen as oxygenated fuel. Simultaneously to the investigation of OH* chemiluminescence discussed in section 4.1.8, time-resolved CH* chemiluminescence in shock-heated $C_2H_5OH/O_2/Ar$ mixtures was recorded and studied for three equivalence ratios (see Table 4.6). Here again, the mechanism from Marinov [38] was chosen with the CH* sub-mechanism and was extended by the C_2 sub-mechanism from Williams and Pasternack [150]. Analogously to the CH* evaluation in the previous section and because of a missing approach for the direct evaluation of CH* chemiluminescence, all profiles were normalized to the corresponding value at 1900 K.

Figure 4.46a shows a typical time-resolved CH* chemiluminescence profile (black solid line) for a fuel-lean mixture. In contrast to other hydrocarbons, the CH* profiles in C_2H_5OH/O_2 reactions do not show any induction time. The instantaneous decomposition of ethanol promotes the formation of intermediate C_2H_4 and CH_3 species that lead to a fast generation of CH* relevant species. Additionally, the computed and normalized CH* concentration (see green line) is plotted as function of time. There is a large deviation in the peak position of the concentration-time history compared to the experimental data. However, the profile shape is in good agreement to the experimental profile as it can be seen for the shifted profile (red line) within the same figure which was shifted by +8 µs. While there is reasonable agreement in the peak location of the experimental and the computed data for temperatures below 1900 K, large discrepancies remain for higher temperatures for all equivalence ratios.

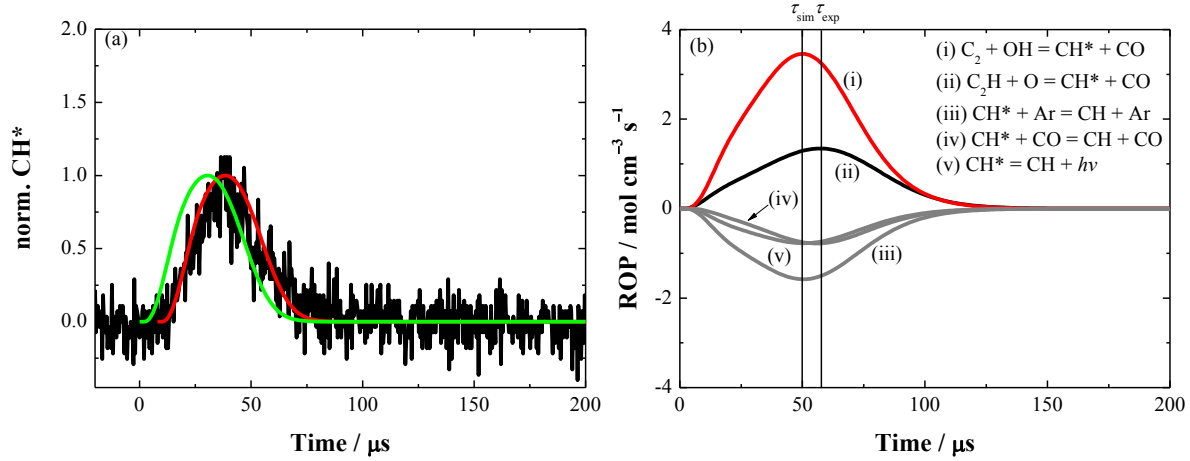

Figure 4.46: (a) Temporal variation of the normalized CH* chemiluminescence (black line) and the CH* concentration (green line) for mixture 23 at T_5 = 1900 K and p_5 = 1.90 bar. (b) ROP analysis of the CH* formation for mixture 22 at T_5 = 1900 K and p_5 = 1.90 bar. The experimental and the simulated peak locations of CH* are illustrated by vertical lines.

The ROP analysis for a stoichiometric mixture composition shown in Figure 4.46b reveals that reactions the predominant CH* formation is attributed to the reaction (i) C_2 + OH = CH* + CO which is responsible for more than 70% of the CH* chemiluminescence. For increasing temperature the ratio (i)/(ii) is further increasing, whereas (ii) C_2H + O = CH* + CO has a minor contribution to CH*.

The comparison of the temporal CH* peak position (indicated by two vertical lines in Figure 4.46b) reveals that the simulation predicts a faster occurrence of CH* chemiluminescence than it can be monitored for the experiments. The simulated CH* peak position is strongly dominated by the reaction (i) because the simulated position is in agreement with the peak of reaction (i) at 50 µs. The experiment, however, shows its peak maximum at 58 µs which perfectly matches with the peak position of the reaction (ii). Based on this finding one can conclude that the model causes a false prediction of the temporal occurrence of C_2 which strongly controls reaction (i) and ultimately CH* which is also reflected in the underestimation of the

CH* peak times. The importance of the reactions (i) and (ii) regarding the contribution to the CH* formation are strongly shifted towards the reaction (i). Apparently, the simulation overestimates the contribution of reaction (i) which leads to a temporal deviation whereas the impact of reaction (ii) with regard to the CH* formation can reproduce the experimental observation. Therefore, the ground-state chemistry which is controlling the formation of C_2 and C_2H and subsequently the contribution of both reactions must be more balanced to match the experimental peak times.

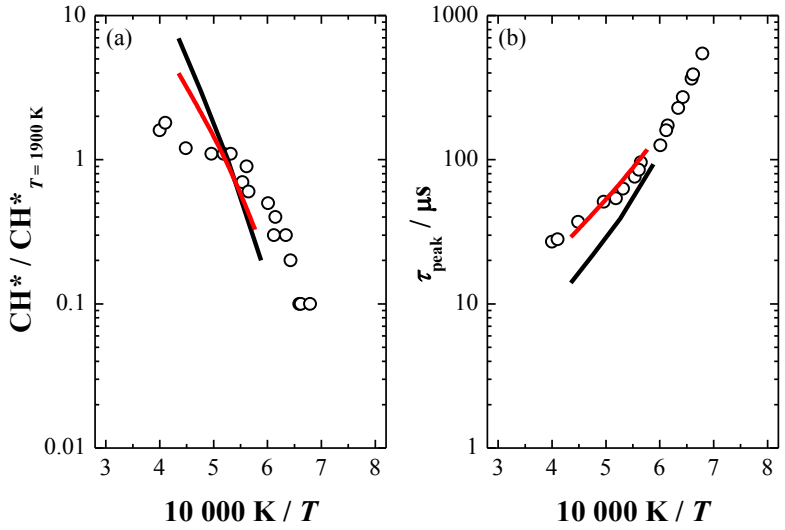

Figure 4.47: Measurement (symbols) and simulation (black lines) of (a) CH* chemiluminescence intensities normalized to the corresponding value at T_5 = 1900 K and (b) delay times for peak CH* for mixture 22. Additional simulations were done using the ground-state mechanism from Saxena and Williams [39] (see solid red line).

Figure 4.47 exemplarily shows the experimental and computed temperature dependence of the CH* chemiluminescence and their corresponding peak times as function of inverse temperature for a stoichiometric $C_2H_5OH/O_2/Ar$ mixture based on the results from the Marinov mechanism (black line). There is a significant deviation in the predicted temperature dependence of the normalized CH* concentrations. The simulation shows a very strong temperature dependence, whereas the experimental data only show a moderate slope. Especially for higher temperatures, the simulations show an almost ten times stronger dependence than the experiments reveal. As mentioned above, the computational data significantly underpredicts the peak times especially for higher temperatures (see Figure 4.47b). Moreover, the predicted temperature dependence of the CH* peak times is stronger in the experimental data. This was observed for all equivalence ratios.

Due to the large deviations in predicting CH*-CL intensities and peak times, additional simulations were done using different ground-state mechanism from Saxena and Williams [39] (cf. Figure 4.47 solid red line). The temperature dependence of the normalized CH*-chemiluminescence intensities still remains overpredicted for both mechanisms. However, the agreement of the slopes is slightly improved compared to the original computational results

based on Marinov mechanism [38]. In contrast to the normalized chemiluminescence intensities, the CH* peak times perfectly match the experimental data. This is attributed to the accurate build-up of the precursor species C_2H and C_2 shown in Figure 4.48. The Marinov mechanism (black lines) predicts a fast formation of C_2H and C_2 radicals. Whereas the calculations using the model from Saxena and Williams compute a later formation of the two precursor species which is reflected in the good correlation with the experimental peak times of CH* chemiluminescence.

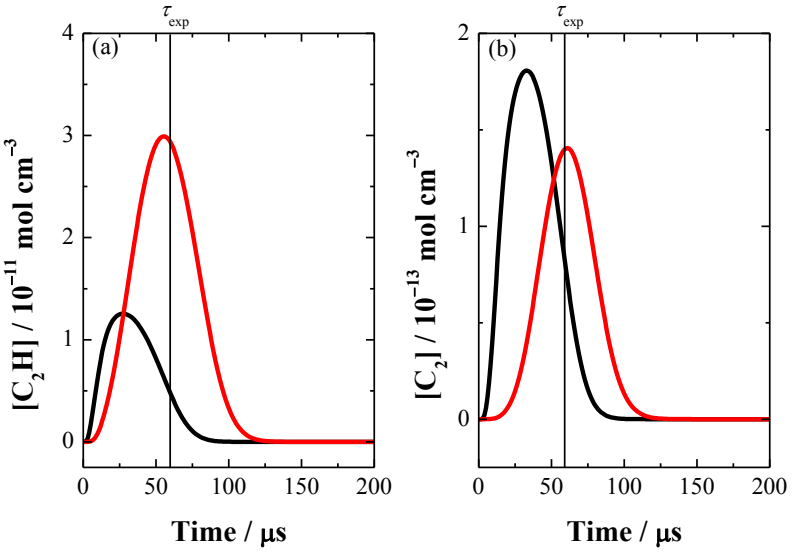

Figure 4.48: Temporal concentration profile of (a) C_2H and (b) C_2 using ground-state mechanisms from Marinov [38] (black line) and from Saxena and Williams [39] (red line) for mixture 22 at T_5 = 1900 K and p_5 = 1.90 bar. The experimental peak time of CH* chemiluminescence is indicated by vertical lines.

The two models predict different C_2 and C_2H concentrations, thus, it is expected that their CH* predictions differ. Again, a good knowledge of the absolute concentration is mandatory. It is shown for the OH* chemiluminescence in section 4.1.3, that the decomposition channels determine the subsequent reactions of the precursors that are required for the formation of chemiluminescence. For the same experimental conditions stated in Figure 4.48, the Marinov model [38] predicts a significantly faster consumption of ethanol which vanishes within 2 µs, whereas it takes 20 µs for the ethanol to be consumed using the alternative model from Saxena and Williams [39]. This overprediction of the ethanol decomposition by the mechanism from Marinov is already reported in several studies [40, 43, 45]. Therefore, further investigations of the ethanol consumption, especially for higher temperatures are strongly required and will be discussed later on in section 4.3.

The ratio of measured OH* and CH* chemiluminescence intensities and the calculated concentrations are presented as function of the inverse temperature (see Figure 4.49). When using the ground-state mechanism from Marinov [38], the ratio of OH*- and CH*-CL is strongly underpredicted and the temperature dependence significantly deviates from the experiment. The discrepancy for higher temperatures is more than one order of magnitude which decreases

for lower temperatures, however, the difference never disappears. The ground-state model from Saxena and Williams [39] predicts a comparable temperature dependence of the OH* and CH* ratio by trend but the absolute values are one order of magnitude lower than the experimental data show. In conjunction with the data evaluation below, one can conclude that here again the overprediction of CH* chemiluminescence is responsible for large deviations in the OH*/CH* ratio.

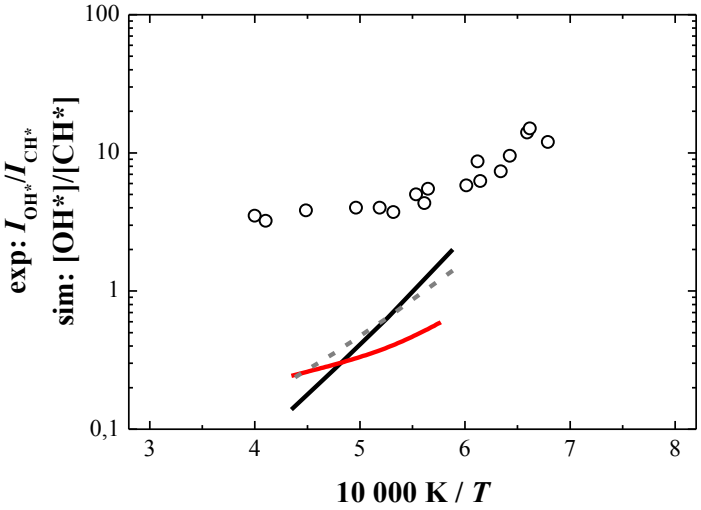

Figure 4.49: Ratio of experimental (symbols) and simulated (black line) OH* and CH* chemiluminescence intensities and concentrations, respectively. Shock-tube experiments and simulations for mixture 22 were used with the rate coefficients k_5 and k_6 from the present work and the Marinov mechanism [38]. Additional simulations were done using the ground-state mechanism from Saxena and Williams [39] (solid red line).

The ratio of the measured OH* and CH* chemiluminescence intensities and the experimental OH* concentration were used to backward calculate target concentrations of CH* (see Table 4.10). The simulated OH* and CH* concentrations using the ground-state mechanism from [39] are tabulated. While the Marinov mechanism can predict the OH* concentration with an accuracy better than ±32%, the computed ratio of OH* and CH* concentrations significantly deviates with regard to the experimental data. Aside from the minor differences in the computed OH* concentrations, the uncertainty of CH* chemiluminescence strongly define the prediction of the OH* and CH* ratio. Both ground-state mechanisms strongly overestimate the CH* chemiluminescence, for the entire temperature range.

Depending on temperature, the CH* concentration ranges from 2.69×10^{-16} to 6.30×10^{-16} mol cm^{-3}. The simulations, however, cannot reproduce the target CH* concentration in any case. At 1700 K, the deviation in the absolute CH* concentration between experiment and simulation is about a factor of 2.5, while for increasing temperature this deviation is more than two orders of magnitude.

Table 4.10: Experimental and simulated OH* and CH* peak concentrations and their relative errors δ for mixture 22.

T / K	1700	1900	2100	2300	Source
[OH*][1]	1.40×10^{-15}	1.78×10^{-15}	2.06×10^{-15}	2.30×10^{-15}	Experiment
[CH*][1]	2.69×10^{-16}	4.08×10^{-16}	5.14×10^{-16}	6.30×10^{-16}	[CH*] = [OH*]×I_{CH*}/I_{OH*}
I_{OH*}/I_{CH*}	5.20	4.36	4.01	3.65	Experiment
[OH*][1]	9.52×10^{-16}	1.54×10^{-15}	2.00×10^{-15}	2.38×10^{-15}	Simulations with the mechanism of Marinov [38] and k_5 and k_6 from the present work
$\delta_{[OH*]}$	−32%	−13%	−3%	−3%	
[CH*][1]	4.55×10^{-16}	2.33×10^{-15}	7.07×10^{-15}	1.66×10^{-14}	
$\delta_{[CH*]}$	+69%	+471%	+1,275%	+2,535%	
[OH*]/[CH*]	2.09	0.66	0.28	0.14	
[OH*][1]	4.83×10^{-16}	1.05×10^{-15}	1.79×10^{-15}	2.77×10^{-15}	Simulations with the mechanism of Williams and Saxena [39] and k_5 and k_6 from the present work
$\delta_{[OH*]}$	−66%	−41%	−13%	−20%	
[CH*][1]	7.28×10^{-16}	2.86×10^{-15}	6.01×10^{-15}	1.14×10^{-14}	
$\delta_{[CH*]}$	+171%	+601%	+1,069%	+1,710%	
[OH*]/[CH*]	0.66	0.37	0.30	0.24	

[1]unit: mol cm^{-3}

The strong deviations between experimental and modeling results, especially for CH* CL in ethanol combustion infer that the available ground-state mechanisms that are used to describe CH* chemiluminescence are not accurate. In particular, the initial decomposition of ethanol strongly controls the formation progress. Thus, more validation efforts are required in particular for the high-temperature oxidation of ethanol. Further characterization of the two ground-state mechanisms considered above will be presented in section 4.3.

4.2.7. CH* kinetics model

Initially, the CH* mechanism consisted of the three potential formation reactions (R5) – (R7). Based on the present experimental findings described in sections 4.2.3 – 4.2.8, reaction $C_2H + O_2 = CH^* + CO_2$ was excluded (recall Figure 4.31). Rate coefficients of the remaining two reactions (R5) and (R6) were optimized with regard to shock-tube data from acetylene combustion. Furthermore, an additional validation was done by means of comparing the results of the present reaction mechanism with premixed-flame experiment from literature [63, 65]

which will be presented in the next chapter. The final mechanism incorporating the formation and consumption reactions considered in the present work is tabulated in Table 4.11.

Table 4.11: Reaction kinetics scheme of CH* species. Reaction rate coefficient $k = AT^n \exp(-E/RT)$.

No.	Elementary reaction	A (cm mol s)	n	E / kJ mol^{-1}	Reference
R5	$C_2 + OH = CH^* + CO$	5.71E+13	0.0	0.0	Present work
R6	$C_2H + O = CH^* + CO$	1.04E+12	0.0	10.9	Present work
R7	$C_2H + O_2 = CH^* + CO_2$	Excluded, see text			
R8	$CH^* = CH + h\nu$	1.86E+06	0.0	0.0	[51]
R9,1	$CH^* + O_2 = CH + O_2$	2.48E+06	2.1	–7.2	[68]
R9,2	$CH^* + CO_2 = CH + CO_2$	2.40E-01	4.3	–7.1	[68]
R9,3	$CH^* + CO = CH + CO$	2.44E+12	0.0	0.0	[68]
R9,4	$CH^* + CH_4 = CH + CH_4$	1.73E+13	0.0	0.7	[68]
R9,5	$CH^* + H_2O = CH + H_2O$	5.30E+13	0.0	0.0	[68]
R9,6	$CH^* + H = CH + H$	2.01E+14	0.0	5.7	[68]
R9,7	$CH^* + OH = CH + OH$	7.13E+13	0.0	5.7	[68]
R9,8	$CH^* + H_2 = CH + H_2$	1.47E+14	0.0	5.7	[68]
R9,9	$CH^* + Ar = CH + Ar$	3.13E+11	0.0	0.0	[152]
R9,10	$CH^* + N_2 = CH + N_2$	3.03E+11	3.4	–1.7	[68]
R9,11	$CH^* + N_2O = CH + N_2O$	5.00E+13	0.0	0.0	[153]

4.2.8. Additional validation of the CH* chemiluminescence mechanism with laminar premixed flames

CH* chemiluminescence was quantitatively measured as a function of height above burner (HAB) under flame conditions by various groups [51, 63, 65] presented in section 4.2.1. Unlike shock-tube experiments, flame experiments can provide absolute CH* concentrations (described in section 4.1.1) giving additional experimental targets to verify the CH* kinetics mechanism derived in the present work. Smith and co-workers [51] studied the spatial distribution of OH*, CH* and C_2* in a premixed CH_4/air low-pressure flame.

Figure 4.50 shows the measured CH* concentrations as a function of HAB for three different equivalence ratios from lean to rich. The simulations were performed using the GRI3.0 mechanism supplemented by the present CH* model. Similar to the OH* data discussed in section

4.1.10, the simulated spatial positions of the CH* peak concentration are slightly shifted towards lower HAB. This was also already reported in [51] and can be attributed to the spatial occurrence of the precursor molecules C_2 and C_2H. The spatial positions of both species were not measured under the given conditions. Aside from the spatial deviations of the CH* peak positions, the predicted CH* peak concentrations and profile shapes are in good agreement with the experimental data. Except for the fuel-lean case where a deviation within the stated error limits was found, however, the model can almost perfectly fit the CH* peak concentration which strengthens the confidence of the determined reaction rates k_5 and k_6.

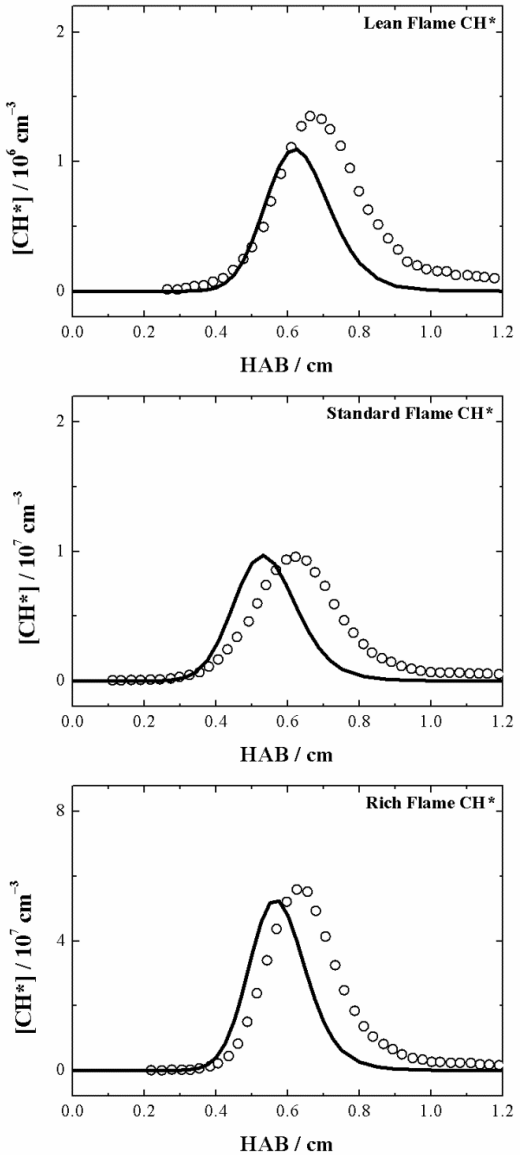

Figure 4.50: Experimental (symbols) and simulated (lines) CH* chemiluminescence for low-pressure methane-air flames of $\phi = 0.81$, 1.07 and 1.27 (from top to bottom) adopted from Smith et al. [51].

Figure 4.51 shows the measured CH* chemiluminescence concentrations from Nau and coworkers [63] as function of the burner distance for two $CH_4/O_2/Ar$ low-pressure flames. The simulated peak positions of CH* chemiluminescence for the stoichiometric case are again

slightly shifted towards the burner, whereas for the fuel-rich case, the presented model can reproduce the shape and spatial position of CH* CL well. However, for the stoichiometric case, the simulated profile is thinner compared to the experimental traces. This observation is attributed to the lower peak concentration. When normalizing the profiles with regard to the corresponding peak values individually, there is good agreement between simulated and experimental profile shapes. This finding was also concluded by the authors using the reaction mechanism from Kathrotia et al. [62, 65, 132]. The CH* concentration for the fuel-rich case is about 20% underpredicted which is covered by the experimental and simulation errors. However, larger discrepancy in the CH* peak concentration is found for stoichiometric conditions where the simulation shows a 50% lower peak concentration which is still covered by the stated error limits. Despite these discrepancies, the trends are well reproduced.

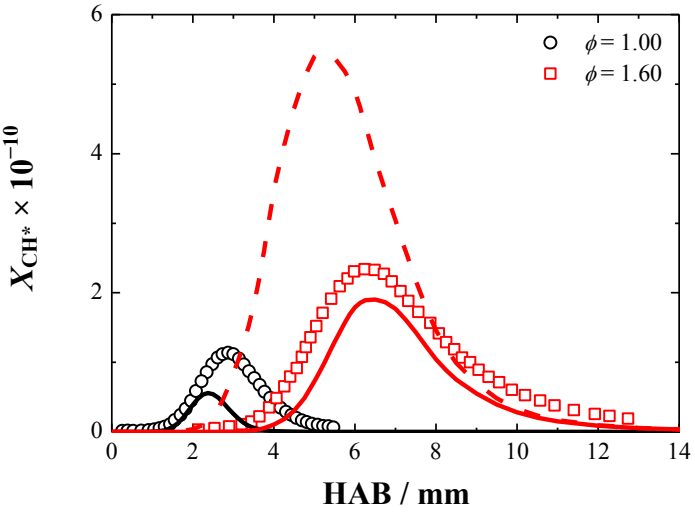

Figure 4.51: Comparison of measurements from [63] (symbols) and simulated (lines) CH* concentrations from the present work at different equivalence ratios. Solid line: simulations with reactions (R5) $C_2 + OH = CH^* + CO$ and (R6) $C_2H + O = CH^* + CO$, dashed line: simulations with reaction (R5), (R6) and (R7) $C_2H + O_2 = CH^* + CO_2$.

To verify that reaction (R7) $C_2H + O_2 = CH^* + CO_2$ has negligible importance as a potential formation pathway of CH* chemiluminescence, additional simulations were performed by incorporating this reaction with the lowest recommended rate coefficient k_7 from [143-144] (see dashed line in Figure 4.51). The predicted CH* peak concentration is very sensitive to reaction (R7) and the simulation is almost three times higher than the experimental concentration. The peak positions also shift towards the burner surface, whereas it almost perfectly fits the experiment when excluding reaction (R7). This observation again verifies the assumption of excluding reaction (R7) from the CH* kinetics mechanism.

According to the procedure described in section 4.1.10, Kathrotia et al. [65] studied the chemiluminescence emission in various methane flames (cf. Figure 4.52). The agreement of the experimental results from [65] and the computed results from the present study for CH* chemiluminescence strongly depends on the equivalence ratio. While for ϕ = 1.5 and 1.6 a

good agreement between the model and the experiment at peak maximum was found, the consensus is, however, less satisfactory for lower equivalence ratios. The computed peak concentrations of CH* chemiluminescence show deviations in some cases, however, there is agreement between experimental and simulated peak concentrations within the stated error limits.

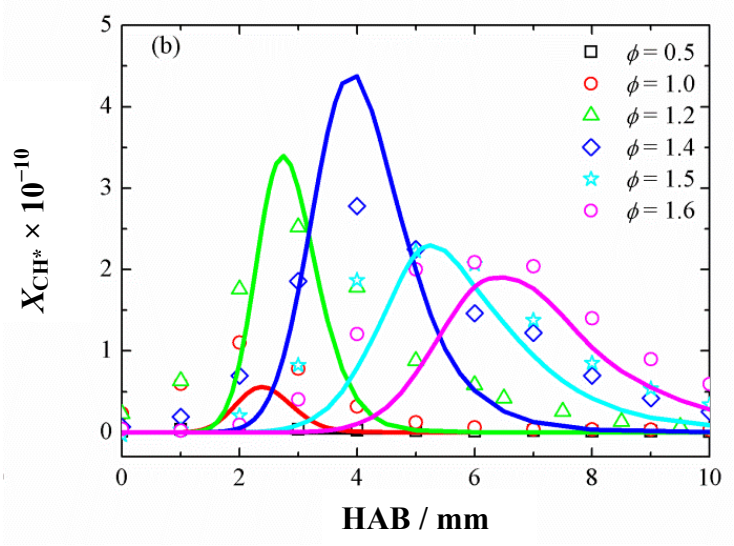

Figure 4.52: Comparison of measurements from [65] (symbols) and simulated (lines) CH* concentrations from the present work at different equivalence ratios.

Overall, aside from the presented shock-tube experiments, the developed CH* model fairly well predicts the formation of CH* chemiluminescence also under flame conditions. However, reliable precursor concentrations are still needed to minimize the error limits of the rate coefficients k_5 and k_6. Both validations emphasized the importance of the reactions (R5) and (R6).

4.3. Validation of the ethanol ground-state chemistry

The investigation of chemiluminescence in ethanol-based mixtures behind reflected shock waves, presented and discussed in section 4.2.6, implied that simulation based on the current knowledge of ground-state chemistry, especially for temperatures above 1600 K does not well reproduce the experimental results. Large deviations were seen for CH* chemiluminescence which can be mainly attributed to deficiencies of the ground-state mechanisms adopted from Marinov [38] and Saxena and Williams [39]. However, these mechanisms were not validated for high-temperature oxidation of ethanol and it was already reported that the pyrolysis reactions of ethanol are not widely studied [40, 43, 45]. Driven by this motivation, additional experiments were performed to study ethanol pyrolysis and oxidation, respectively, by means of shock-tube measurements with multi-species analysis with a high-repetition-rate time-of-flight mass spectrometer (see section 3.2.1) and OH absorption behind shock waves (see section 3.1.2).

4.3.1. Time-of-flight mass spectrometry of ethanol pyrolysis and oxidation under shock-heated conditions

Ethanol pyrolysis was studied based on TOF-MS experiments in the shock tube presented in section 3.2.1. Concentration-time histories of multiple species were recorded to constrain available kinetics models for the ethanol combustion. Based on this evaluation, the thermal decomposition route of ethanol was determined. Additionally, ethanol oxidation measurements were performed. The experimental conditions are tabulated in Table 4.12. Three mechanisms introduced in section 2.2.4 were tested in order to represent the experimental data [38-39, 45].

Table 4.12: Mixture compositions and experimental conditions of shock-heated C_2H_5OH/O_2 experiments.

Mixture	% C_2H_5OH	% O_2	% Ar	% Ne	ϕ	T_5 / K	p_5 / bar
24	1.00	–	1.00	98.00	–	1050 – 1837	1.54 – 2.03
25	1.00	3.00	1.00	95.00	1.00	1047 – 2222	1.18 – 2.11

4.3.1.1. Investigation of ethanol decomposition

The advantage of the high-repetition-rate time-of-flight mass spectrometry is the capability of simultaneously detecting multiple species with appropriate time resolution illustrated by a full spectrum shown in Figure 4.53 measured with a repetition rate of 10 µs. This facility was used to identify intermediates and stable products such as CO, CO_2, CH_4, C_2H_2, C_2H_4 and C_2H_5OH.

The mass spectrum in Figure 4.53 shows two peaks at m/z = 20 and 22 which are attributed to the isotopes of the bath gas neon. Neon was used as bath gas because it provides a comparably low ion signal. Argon (m/z = 40) was used as inert reference gas to account for gas dynamics effects that affect the gas expansion after the shock arrival during the sampling through the nozzle. All signals were then evaluated relative to the argon signal. Due to species fragmentation in the ionization region, data evaluation must be carefully executed in order to separate the contribution from the fragmentation and the underlying chemical kinetics. For this purpose, the impact of the fragmentation must be independently measured by performing additional experiments at room temperature or at low temperatures behind reflected shock waves, typically below 1000 K where no chemical reactions occur on the timescale of the shock tube experiments (< 1 ms). Based on this procedure, the fragmentation spectrum for the original reactants can be determined and subtracted. Quantitative correlation of signal intensities to absolute species concentration can be extracted from stable products such as C_2H_2 and C_2H_4 by performing additional calibration experiments with defined initial concentrations. In contrast to stable species, where intensity calibration is feasible directly, the calibration for

H_2O is not straightforward because of the tendency of water to adsorb on surfaces. Hence, methane oxidation was used as benchmark which generates defined water concentrations in order to calibrate the measured H_2O signal.

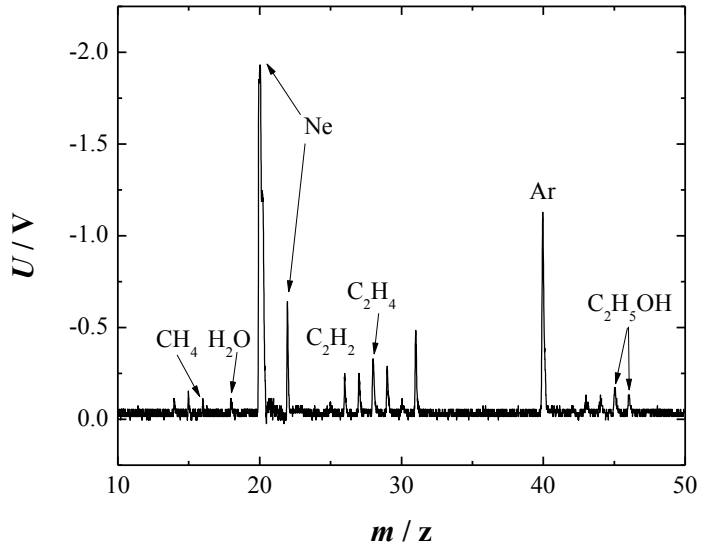

Figure 4.53: Single mass spectrum of ethanol pyrolysis behind the reflected shock wave for mixture 24 at t = 1500 µs. The experimental conditions were: T_5 = 1400 K and p_5 = 1.54 bar.

The pyrolysis of ethanol dominates the entire reaction scheme because it provides high concentrations of important intermediate species such as C_2H_2 and C_2H_4 which are further processed by secondary reactions. Therefore, an accurate knowledge of the different branching reaction pathways during the pyrolysis is mandatory to understand ethanol combustion. Figure 4.54 shows experimental and simulated time-resolved concentration profiles of C_2H_5OH, C_2H_4 and H_2O. The decomposition of C_2H_5OH is not completed for the specified conditions within 1 ms at this conditions. Almost one third of the initial concentration was not converted. At low temperatures between 1000 and 1300 K less than 15% of the total ethanol decomposes within 1 ms whereas in the case of temperatures above 1800 K, the complete conversion of ethanol is completed within 10 µs. The solid lines represent the predictions from Marinov [38] (red line), Saxena and Williams [39] (blue line) and Kiecherer and co-workers [45] (green line) where the rates of the main decomposition channels of ethanol were readjusted in the Marinov model. Overall, both latter models show a good agreement with the experimental data at short reaction times but deviate at long reaction times. Whereas the original Marinov mechanism significantly overestimates the thermal decomposition of ethanol within the entire temperature range. A ROP analysis (not shown) based on the original Marinov mechanism [38] reveals that the fission reaction C_2H_5OH (+ M) = CH_3 + CH_2OH (+ M) consumes two times more ethanol than the isomerization pathway via C_2H_5OH (+ M) = C_2H_4 + H_2O (+ M). In contradiction to this observation, the modified Marinov mechanism based on the recommendations from Kiecherer et al. [45] predicts that ethanol decomposes almost exclusively via

the latter reaction while other reactions are at least one order of magnitude lower. This observation was already supported in [40, 43, 45].

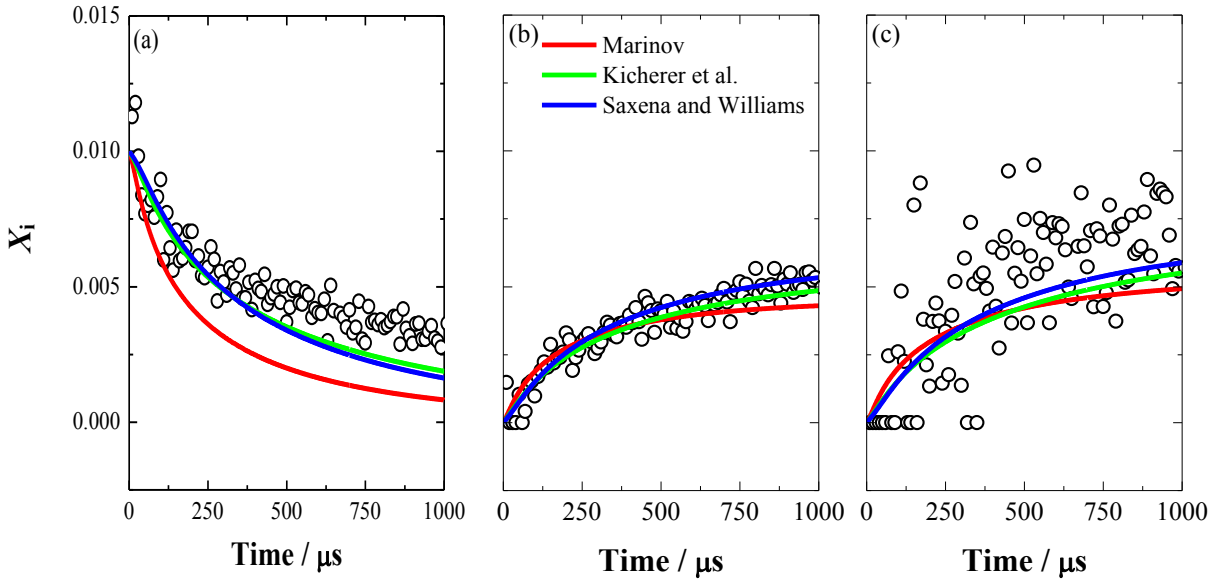

Figure 4.54: Experimental (symbols) and simulated (lines) (a) C_2H_5OH, (b) C_2H_4 and (c) H_2O mole fractions for a shock-heated mixture 24 at T_5 = 1400 K and p_5 = 1.54 bar.

Figure 4.54b and c illustrate that C_2H_4 and H_2O are formed almost in equal proportions. However, the ethylene concentration is slightly lower compared to H_2O due to subsequent consumption reactions of C_2H_4 towards the formation of C_2H_2. Overall, the predictions from Saxena and Williams [39] (blue line) and Kiecherer and co-workers [45] (green line) can retrace the time histories of both species. Although the original Marinov mechanism [38] significantly overpredicts the consumption of ethanol, there are only small deviations in the absolute C_2H_4 and H_2O concentrations.

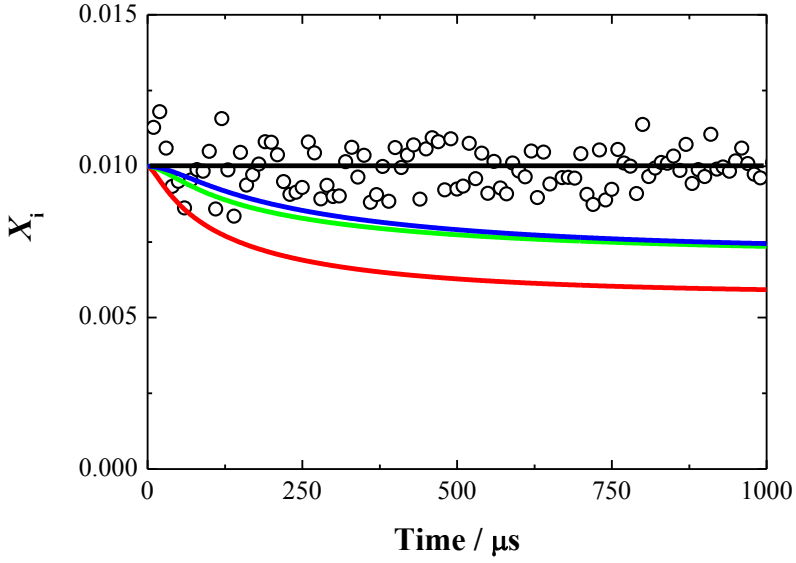

Figure 4.55: Carbon mass balance of the hydrocarbon species C_2H_2, C_2H_4 and C_2H_5OH over time compared with the predictions of the modeling for a shock-heated mixture 24 at T_5 = 1400 K and p_5 = 1.54 bar. The initial concentration is indicated by the black line.

To check the reliability of the experimental data, the carbon balance was evaluated (shown in Figure 4.55) based on the calibration factors for C_2H_2, C_2H_4 and C_2H_5OH. It was found that 30% of the carbon remains in ethanol, around 53% forms C_2H_4 and around 17% is present as C_2H_2. The total initial carbon amount can be solely retraced by summing the measured concentrations of C_2H_2, C_2H_4 and C_2H_5OH. All mechanisms have in common that they do not retrace the experimentally observed carbon balance when solely considering the three latter species. While the results from Saxena and Williams [39] (blue line) and Kiecherer and co-workers [45] (green line) show a deviation of 25%, the original Marinov mechanism shows a deviation of 40% with respect to the initial concentration. The models predict that other carbon-containing intermediate species such as CO, CH_4 and CH_3HCO are available in considerable amounts. When exemplarily evaluating the carbon distribution for the modified Marinov mechanism from Kiecherer and co-workers [45], the following fractions can be obtained with respect to the initial carbon amount: 49% C_2H_4, 19% C_2H_5OH, 8% CH_3HCO, 7% CO, 6% C_2H_2, 4% CH_4 and 7% other hydrocarbons. At the first glance, the measured mass spectra for ethanol pyrolysis seem to show chemical formation especially of CH_3HCO and CO. However, this signal is predominantly induced by the electron bombardment in the ionization chamber where fragmentation of ethanol molecules takes place. A separation between fragmentation and chemical formation is not feasible because of the strong signal scattering at the corresponding mass signal. Furthermore, the simulations also predict a valuable formation of CO molecules. As already shown in Figure 4.54b, the measured and simulated ethylene concentrations show a very good agreement which is also in agreement with the results of [45]. If the simulated C_2H_4 concentration is superimposed by the predicted CO concentration, there would be a 10% overprediction of the sum of C_2H_4 and CO concentrations which does not agree measurement.

A comparison of the experiments with the simulations at temperatures below 1700 K show, that (i) all mechanisms accurately predict temporal concentration profiles of H_2O, C_2H_2, C_2H_4 at short times, however, there are notable differences at longer reaction times. (ii) The original Marinov mechanism strongly overestimates the removal of ethanol within the entire temperature range. (iii) In contrast to the experimental results, the simulations cannot retrace the total carbon concentration by exclusively considering C_2H_2, C_2H_4 and C_2H_5OH. The models consistently predict considerable amounts of other carbon-containing species. (iv) The experiments, however, clearly show that the decomposition of ethanol is predominantly attributed to the reaction C_2H_5OH (+ M) = C_2H_4 + H_2O (+ M) whereas the simulations overestimate the impact of the reaction C_2H_5OH (+ M) = CH_3 + CH_2OH (+ M) and therefore, overestimate the consumption of ethanol which is not in agreement with the experimental observations. This was already reported by Li et al [40].(v) Based on the present experimental data which show that the formation of other carbon-containing species instead of C_2H_4 and C_2H_2 is not likely, one can conclude that the ground-state mechanisms, which predict valuable amounts of CO

and CH_3HCO etc., should the optimized especially in predicting the secondary reactions of ethanol where the occurrence of other species than the two aforementioned is not likely.

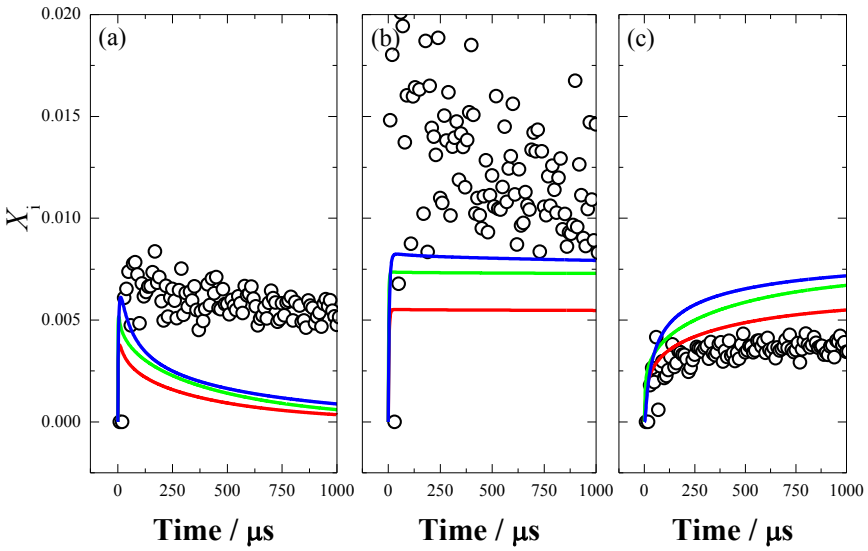

Figure 4.56: Experimental (symbols) and simulated (lines) (a) C_2H_4, (b) H_2O and (c) C_2H_2 mole fractions for a shock-heated mixture 24 at T_5 = 1837 K and p_5 = 1.72 bar.

While for low temperatures ethanol decomposition takes about 2000 µs to complete, the consumption of ethanol for temperatures above 1600 K is completed in less than 10 µs. The temporal behavior of C_2H_4, H_2O and C_2H_2 is exemplarily presented in Figure 4.56 for T_5= 1837 K and the experimental data is compared with the predictions of the three mechanisms. At this temperature, the experimental time resolution does not allow to follow transient C_2H_4 accurately at short times. The comparison is straightforward at longer reaction times where significant deviations in all temporal concentration profiles can be observed. For C_2H_4, the experiment shows a peak concentration of 0.007 at 70 µs which slowly declines to 0.005 at 1000 µs. Water shows an almost steady plateau concentration around 0.0125 and C_2H_2 slowly increases up to 0.003 at 1000 µs. Compared with the simulation results for C_2H_4, there is a large deviation at the peak maximum of 30% while for longer reaction times this value further increases. These deviations were already observed for low temperatures (cf. Figure 4.54), however, their impact at higher temperatures is more pronounced. Furthermore, all mechanisms overpredict the formation of C_2H_2 which is predominantly formed from ethylene via subsequent reactions while H_2O is about a factor of 1.5 underestimated.

According to the simulation results for low-temperature pyrolysis of ethanol, all mechanisms obviously overestimate the contribution of other hydrocarbon species instead of C_2H_2 and C_2H_4 for high-temperature pyrolysis. Again the methyl-abstraction of ethanol is overestimated by the different mechanisms which lead to large discrepancies in the temporal C_2H_4 and C_2H_2 concentrations whereas the measurements again show a carbon distribution where C_2H_4 and C_2H_2 are predominantly formed and other species are only of minor importance. These exper-

imental observations indicate that the decomposition reaction via C_2H_5OH (+ M) = C_2H_4 + H_2O (+ M) is the main decomposition channel leading to high C_2H_4 and C_2H_2 concentrations. Overall, the evaluation of the pyrolysis experiments reveals that the considered mechanisms obviously overestimate the impact of the decomposition reaction via C_2H_5OH (+ M) = CH_3 + CH_2OH (+ M). This initial reaction therefore, the branching ratio of the different decomposition pathways of ethanol must be carefully measured under defined conditions.

4.3.1.2. Investigation of ethanol oxidation

To study the oxidation of ethanol, experiments of stoichiometric ethanol and oxygen mixtures were shock-heated and the species are monitored by TOF-MS. In general, the oxidation of ethanol occurs within the experimental test time at temperatures above 1200 K.

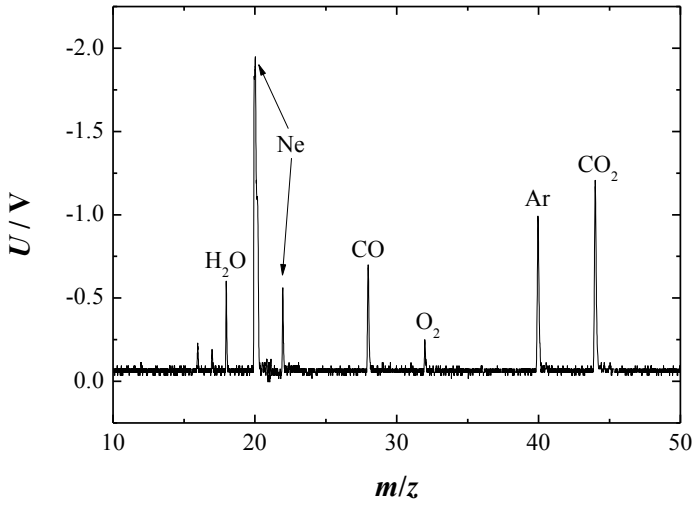

Figure 4.57: Single mass spectrum of ethanol oxidation behind the reflected shock wave for mixture 25 at t = 1530 µs. The experimental conditions were: T_5 = 1572 K and p_5 = 1.40 bar.

A typical post-shock mass spectrum for a stoichiometric ethanol/oxygen mixture is shown in Figure 4.57. The only species that can be monitored in the mass spectrum aside from the bath gas neon and the reference gas argon, are O_2, H_2O, CO and CO_2. Due to the quick conversion of ethanol, the mass of ethanol at m/z = 45 and 46 were not observed. Other species such as CH_4, C_2H_2 or C_2H_4 cannot be observed because of their low concentrations.

In the present evaluation of the mass spectra for ethanol oxidation, the mass signal at m/z = 28 was exclusively attributed to CO although C_2H_4 has the same molecular weight. The mass resolution of the spectrometer is $\Delta m/m$ = 777. Therefore, a separation of C_2H_4 (28.0313) and CO (27.9949) is not feasible, where the mass units in the parenthesis are the ^{12}C isotope contributions. Ethylene as a short-lived intermediate is instantaneously formed at zero-time and is consumed very fast whereas CO as a post-kinetics species is continuously formed within the observation time and can be captured within the time resolution of the mass spectrometer. Therefore, a contribution of C_2H_4 must be considered in the first stage and after 100 µs the

contribution of ethylene disappears and the mass signal is solely attributed to CO. Based on the modeling, we were able to distinguish the contribution of C_2H_4 and CO.

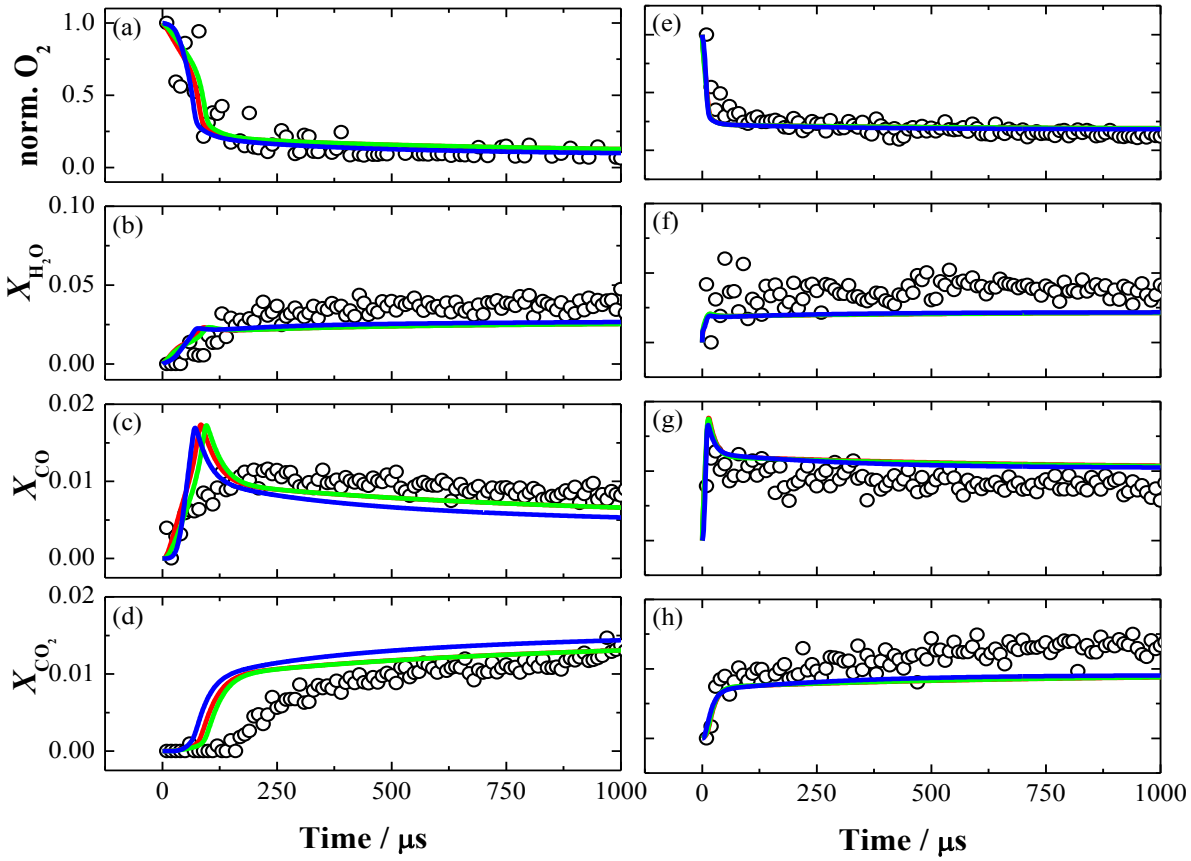

Figure 4.58: Experimental (symbols) and simulated (lines) norm. O_2, H_2O, CO and CO_2 mole fractions for a shock-heated mixture 24. Experimental conditions for (a–d): T_5 = 1572 K and p_5 = 1.40 bar. Experimental conditions for (e–h): T_5 = 2222 K and p_5 = 1.18 bar.

Figure 4.58 shows typical experimental (open circles) concentration-time histories of the combustion relevant species O_2, H_2O, CO and CO_2 at intermediate temperatures. Based on the carbon balance, the oxidation of ethanol is completed within 250 µs whereas the simulations predict an almost three times faster conversion. Although the gas mixtures are prepared for stoichiometric conditions, the oxidation process is not completely finished and residual O_2 and CO can be monitored within the entire test time. Even for higher temperatures over 2000 K, more than 10% of the initial oxygen is remaining unconsumed. While carbon monoxide, oxygen and water do not show any induction time, CO_2 shows a delayed formation. For longer reactions times (> 125 µs under the present experimental conditions) CO is oxidized to CO_2. The experimental results for high temperatures show similar behavior like the low temperature results discussed before (see Figure 4.58 (e–h)). The main differences are the fast reaction progress of the oxidation and the higher final concentrations of the stable products.

The corresponding concentration-time histories were simulated using the model from Marinov [38] (red line, Saxena and Williams [39] (blue line) and Kiecherer and co-workers [45] (green line). For low temperatures, the computed final concentrations for H_2O, CO and

CO_2 from all considered mechanisms match the experimental observations at longer reaction times. Some deviations are, however, seen at short times. The models predict an almost sudden and complete consumption of oxygen within 100 µs, whereas the experiment shows a smooth consumption. As consequence of the fast oxidation behavior, the predicted concentrations of CO and CO_2 are significantly higher at short reaction times. Especially for CO, there is disagreement between computed and measured time profiles at short reaction times. In particular, the simulated CO concentrations from the various mechanisms show a distinct peak around 100 µs which cannot be observed for the experimental data. While CO is underpredicted for longer reaction times, CO_2 as a direct product of CO is overpredicted.

At higher temperatures, there is better agreement between experiments and simulations for ethanol oxidation (see Figure 4.59e–h). Here again, the simulations predict a shoulder for CO that was not observed in the experiments. However, the measured long-term concentrations of the considered species are in agreement with the experiments. The absolute CO concentration at longer reaction times is slightly overpredicted, while the computed CO_2 concentration is lower.

Overall, the evaluation of the measurements at short reaction times and low temperatures is not consistent with any reaction mechanism. There are significant temporal deviations between experimental and simulated concentration-time profiles which are potentially not caused by simulation errors but by an insufficient time-resolution of the TOF-MS. Especially the distinct peak in the CO concentration-time profile, which is typical for hydrocarbon combustion and which was already verified for methyl formate by Ren et al. [154], cannot be reproduced by the present experimental data. A careful verification of the present time-resolution of the TOF-MS seems to be essential to quantitatively compare the present experiments and the available reaction mechanisms.

4.3.2. Ring-dye laser measurements of OH

While C_2H_4 is an important intermediate species during the combustion of most hydrocarbons, OH is a transient species that controls branching reactions at early times. For further validation, ethanol oxidation was monitored by measuring the OH concentration optically. While there is substantiated knowledge available for the combustion of small hydrocarbons such as methane, only sparse information can be found for ethanol combustion. In addition to the shock tube/TOF-MS experiments presented in the previous section, the present study is also devoted to provide additional validation of OH species by probing the A–X transition. Analog to the initial OH absorption experiments in the argon-diluted H_2/O_2 and CH_4/O_2 systems described in section 3.1.2.4, additional investigations of OH formation in ethanol combustion were performed.

4.3.2.1. OH absorption in argon-diluted C_2H_5OH/O_2 mixtures

OH absorption was studied behind reflected shock waves within a wide temperature range for near-atmospheric pressures. Aside from the recent study from Sivaramakrishnan et al. [155], these are the first direct OH absorption experiments under shock-tube conditions for ethanol combustion. The experimental conditions are given in Table 4.13.

Table 4.13: Mixture composition and experimental conditions for $C_2H_5OH/O_2/Ar$ experiments.

Mixture	% C_2H_5OH	% O_2	% Ar	ϕ	T_5 / K	p_5 / bar
26	0.1	0.3	99.6	1.00	1386 – 2518	1.52 – 2.07

The temporal variation of OH for a stoichiometric mixture composition at 1449 K with its significant two-stage behavior is presented in Figure 4.60a. The first stage produces about 25 ppm OH whereas the second stage shows a plateau concentration of 125 ppm. As shown in Figure 4.60b, the dual peak behavior cannot be observed at high temperatures where a distinct rise of the OH* concentration occurs which forms a plateau.

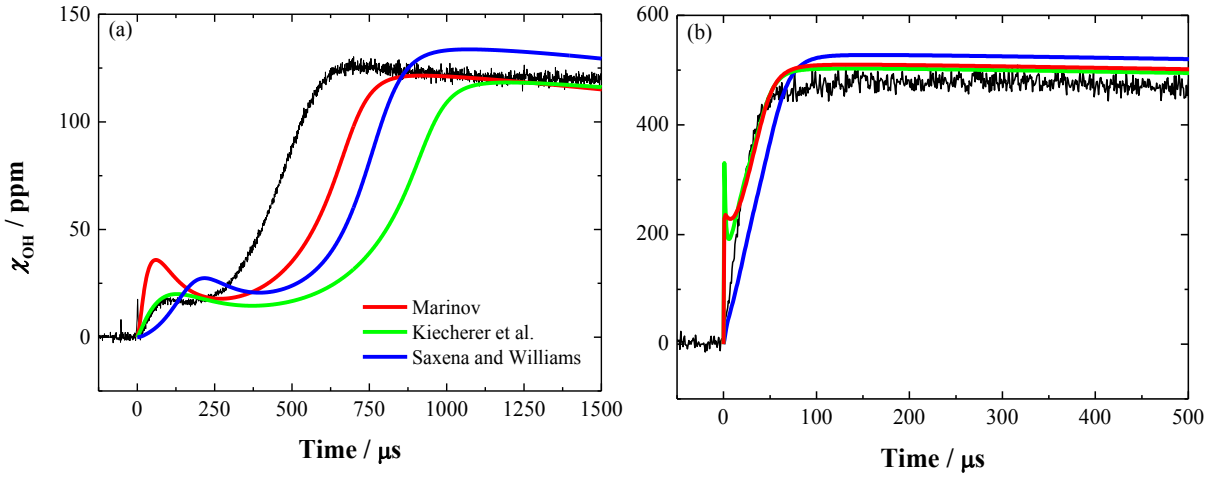

Figure 4.60: Measured temporal variation of the OH concentration (black line) for mixture 26 at (a) T_5 = 1449 K and p_5 = 2.05 bar and (b) T_5 = 2293 K and p_5 = 1.61 bar.

The simulations consistently reveal that the first stage of OH formation is mainly due to the reaction $H + HO_2 = 2OH$ and a minor portion is attributed to $C_2H_4OH = C_2H_4 + OH$. Whereas the second peak shows a strong sensitivity towards the reaction $O_2 + H = OH + O$. None of the considered reaction mechanisms can reproduce both stages accurately. Overall, at low temperature, the best agreement was found with Marinov-based mechanisms, however, the simulated [OH] profiles still disagree with the experiments especially at shorter times. All three models significantly mismatch the peak position of OH. While the peak concentrations and the OH concentrations at long times are in good agreement with simulations based on the Marinov model [38, 45].

According to the measurements at temperatures above 1800 K, the dual peak in the simulated results based on the Saxena and Williams model [39] disappears and only the second peak is seen (see Figure 4.60b). In contrast to this observation, simulations based on the Marinov mechanism [38, 45] still show a two stage behavior with a distinct peak at $t = 0$ µs before merging into the second stage. This temporal discrepancy, however, disappears afterwards and the simulations can perfectly reproduce the experimental shape and the predicted peak concentrations with regard to the experimental uncertainties. The erroneous prediction of the first stage OH at high temperature is still attributed to the contribution of $H + HO_2 = 2OH$. Whereas for high temperatures, the Marinov-based mechanisms [38, 45] reveal that the second stage is strongly dominated by the fission reaction of C_2H_5OH towards $C_2H_5 + OH$. At low temperatures, the second stage was controlled by the chain-branching reaction $O_2 + H = OH + O$. Contrary to the Marinov models, Saxena and Williams [39] predicts an exclusive production of OH via $O_2 + H = OH + O$ which explain the non-appearance of the first stage. However, discrepancies in the temporal shape and the absolute OH concentration were found using the latter mechanism.

Overall, none of the models can accurately and consistently predict the OH formation throughout the entire temperature range covered herein. While the Marinov based mechanisms show a good performance in predicting the absolute OH concentration, they show significant differences in reproducing the temporal behavior. The model from Saxena and Williams shows a slightly better performance in predicting the temporal OH behavior for high temperatures whereas it consistently lacks in prediciting the absolute OH concentrations. An in-depth experimental and modeling investigation of the ethanol ground-state chemistry is necessary to further improve the predictions of OH during ethanol combustion.

5. Conclusions

The optimization and control of practical combustion systems is a prerequisite for increasing fuel efficiency and reduction of pollutant emission. The use of chemiluminescence (CL) detection has proven to be beneficial under lab-scale conditions since it is a non-expensive and non-intrusive approach to get quantitative information of global combustion parameters. For example, the determination of the local equivalence ratios and heat release are potential applications for combustion research. For this purpose, a quantitative link between the measured chemiluminescence intensities and the underlying chemical reactions are necessary. However, the formation kinetics of chemiluminescence is not thoroughly understood and the published corresponding rate coefficients vary by several orders of magnitude. The complication originates from the difficulty to establish a quantitative relationship between measured CL intensities and corresponding species concentrations. An additional complication arises from uncertainties intrinsic to ground-state chemical reactions of relevance to excited-state species formation. In particular, a precise quantification of the molecules that lead towards the formation of electronically-excited species is necessary. Therefore, the purpose of the work was to identify the formation channels of chemiluminescence at atmospheric pressures, to measure their corresponding rate coefficients, and to develop kinetics mechanisms describing the chemiluminescence of various systems. For this task, a combination of shock-tube experiments and kinetics simulations was employed where well-known ground-state mechanisms from literature were used as base to compile kinetics mechanisms for OH* and CH* chemiluminescence consisting of formation reactions and the corresponding collisional quenching reactions adopted from literature.

In this thesis, the chemiluminescence of OH* and CH* were systematically investigated based on CL emission in shock-heated hydrogen and hydrocarbon mixtures. The chemiluminescence emission from the A–X transitions of OH* around 307 nm and of CH* around 430 nm, respectively, were detected by two separate interference filter and photomultiplier combinations. The measured temporally-resolved chemiluminescence profiles were compared with simulated OH* and CH* concentration-time profiles. Within the frame of this thesis the following findings were achieved.

The formation of OH* chemiluminescence was measured in various H_2/O_2/Ar mixtures. Based on a high-temperature calibration where OH* is exclusively formed by OH + M = OH* + M, the measured OH* emission intensities were converted to time-resolved OH* concentrations with an accuracy of ±20%. The measured OH* concentrations were then used for the development and validation of a OH* kinetics mechanism. On the basis of this indirect calibration, the comparison of measured and simulated data revealed that OH* in H_2/O_2 systems is predominantly formed by the reaction (R1) H + O + M = OH* + M. The best agreement in

terms of absolute OH* concentrations and ignition delay times was found for a rate coefficient of $k_1 = (1.5\pm0.45)\times10^{13}\ \exp(-25.0\ \text{kJ mol}^{-1}/RT)\ \text{cm}^6\text{mol}^{-2}\text{s}^{-1}$. The results were used to describe OH* chemiluminescence build-up in a hydrocarbon system. With this approach, the formation channel of OH* in CH_4-blended H_2/O_2 mixtures was investigated. Again, the measured OH* chemiluminescence was compared with simulations. It was found that the main formation channel of OH* in hydrocarbon combustion is (R2) $CH + O_2 = OH^* + CO$. The rate coefficient was determined as $k_2 = (8.0\pm2.56)\times10^{10}\ \text{cm}^3\text{mol}^{-1}\text{s}^{-1}$. Collisional quenching reactions and radiative reactions were adopted to account for losses in chemiluminescence intensity. To check the flexibility of the adopted mechanism further experiments in more complex hydrocarbon oxidation systems were carried out. Shock-tube experiments of various hydrocarbon systems (CH_4, C_2H_2, C_2H_4 and C_2H_5OH) at various equivalence ratios from 0.50 to 1.25 and with O_2 and N_2O as oxidizers were performed. Moreover, the modified OH* sub-mechanism from the present work was tested against flame data from literature. Overall, good agreement between experimental and modeling data was found for all experimental conditions.

The ratio of OH* and CH* chemiluminescence is often evaluated to determine combustion relevant parameters such as the local equivalence ratio and heat release. Therefore, a reliable knowledge of CH* kinetics is important. Because calibration approach for CH* chemiluminescence signal intensities under shock-tube conditions is not feasible so far, the evaluation of CH* CL was done by normalizing the intensities and concentration towards the corresponding value at 1900 K. Acetylene oxidation was chosen as benchmark because it provides a high amount of C_2 and C_2H which are assumed to be important key precursors for CH*. The results showed a significant CH* signal reduction for fuel-lean conditions which was already reported in literature [53]. This observation was used to identify the CH* formation pathways. The kinetics model could only reproduce this signal reduction when considering the reactions (R5) $C_2 + OH = CH^* + CO$ and (R6) $C_2H + O = CH^* + CO$ while reaction (R7) $C_2H + O_2 = CH^* + CO_2$ was excluded. When incorporating the latter reaction with a rate coefficient higher than $k_7 = 1.0\times10^{11}\ \text{cm}^3\text{mol}^{-1}\text{s}^{-1}$, the experimental results could not be reproduced. This rate coefficient therefore can be considered as an upper limit. The rate coefficients for the two favored reactions were determined based on the temperature dependence of the CH* chemiluminescence. The best agreement between experiment and simulations were $k_5 = 5.7\times10^{13}\ \text{cm}^3\text{mol}^{-1}\text{s}^{-1}$ and $k_6 = 1.0\times10^{12}\ \exp(-10.9\ \text{kJ mol}^{-1}/RT)\ \text{cm}^3\text{mol}^{-1}\text{s}^{-1}$ with an estimated error of ±53%. The CH* mechanism was additionally investigated for various hydrocarbon combustion systems (CH_4, C_2H_4 and C_2H_5OH). While the simulated results based on the developed CH* sub-mechanisms are in good agreement with the present shock-tube experiments for methane, acetylene and ethylene systems and flame experiments from literature, deficiencies have been found for the CH* chemiluminescence predictions of ethanol combustion. These deviations are mainly attributed to deficiencies of the ground-state mechanisms since the present mechanisms are only validated for temperatures up to 1700 K which is

below the present experimental conditions. Therefore, the ground-state chemistry of ethanol was investigated for pyrolysis and oxidation under shock-tube conditions using time-of-flight mass spectrometry (TOF-MS) and ring-dye laser absorption spectroscopy (RDLAS).

Time-resolved concentration-times histories of multiple intermediate (C_2H_2, C_2H_4) and product species (CO, CO_2, H_2O) were measured for ethanol pyrolysis using a shock tube/time-of-flight mass spectrometer (TOF-MS) combination. The concentrations of C_2H_2, C_2H_4, CO and CO_2 were well-balanced within the experimental error. The carbon balance reveals that the initial carbon concentration can be reproduced by considering C_2H_5OH, C_2H_4 and C_2H_2 as a subsequent product of ethylene. Therefore, the present study proved that the pyrolysis of C_2H_5OH is strongly controlled by the isomerization pathway C_2H_5OH (+ M) = C_2H_4 + H_2O (+ M) while other reactions are of minor importance, otherwise other intermediate species would be formed and detected by the TOF-MS which was not the case within the present work. Ground-state mechanisms from Marinov [38], Kiecherer et al. [45] and Saxena and Williams [39] were tested with satisfactory agreement between experimental and simulated concentration profiles for C_2H_5OH, C_2H_2, C_2H_4 and H_2O for temperatures below 1700 K. However, large discrepancies were found for the corresponding concentration-time histories at higher temperatures where the simulated ethanol decomposition was much faster than observed in the present experiments reveal. The mechanisms overestimate the impact of the methyl-abstraction via C_2H_5OH (+ M) = CH_3 + CH_2OH (+ M) and therefore, the pyrolysis is overwhelmed by the respective reaction. Based on the disagreement between experiments and simulations, the present mechanism must be carefully reevaluated especially with regard to the branching ratio of the two competeting decomposition pathways of ethanol via C_2H_5OH (+ M) = CH_3 + CH_2OH (+ M) and C_2H_5OH (+ M) = C_2H_4 + H_2O (+ M) while the present study strongly indicates that the latter reaction is the most important for the thermal decomposition of ethanol. Overall, the pyrolysis process of ethanol strongly controls the entire combustion process. For an improvement of the available mechanisms, where none of them can reproduce the experimental results for the entire temperature range of the present study, a detailed evaluation is necessary in future.

Additionally, the oxidation of ethanol was measured for stoichiometric conditions behind reflected shock waves using the TOF-MS. While there are deviations in the short-term concentration-time histories especially for CO_2, the slow formation of CO, CO_2 and H_2O and their absolute concentrations for the ethanol oxidation can be fairly well reproduced by the three models. However, comparison between experiment and simulation reveal that the measured concentration-time histories from the TOF-MS show significant deficiencies in the temporal resolution. The short-term concentrations and fast concentration changes cannot retraced by the present experimental configuration.

The ground-state chemistry of many hydrocarbons is controlled by OH which is responsible for the build-up of the radical pool. Therefore, absolute OH concentrations during the oxida-

tion of ethanol were monitored by differential laser absorption in the UV at 306 nm with an experimental accuracy better than ±5%. The considered kinetics mechanisms for ethanol oxidation can predict the maximum OH concentration with an error of ±10%. However, the models show large deficiencies in reproducing the temporal behavior of OH, especially for low temperatures. While for temperatures up to 1800 K the simulations consistently reveal that OH is formed in two stages via $H + HO_2 = 2OH$ and $O_2 + H = OH + O$, respectively, there is disparity in identifying the reaction scheme for high temperatures. All models show deficiencies at high temperatures because of differences in the initial decomposition channels. While the ground-state mechanisms based on Marinov favor the bond-fission reaction of C_2H_5OH towards C_2H_5 and OH to be the main source of OH, the Saxena and Williams model considers the chain-branching reaction $O_2 + H = OH + O$ responsible for the OH formation. While the importance of OH for the underlying reaction mechanism was clearly demonstrated, its formation reactions in ethanol oxidation are still not clear. The different ground-state mechanisms favor different key reactions for the formation of OH depending on the initial decomposition step of ethanol which is chosen by the different ground-state mechanisms. Overall, the present study reveals that the pyrolysis is of fundamental importance for a comprehensive investigation and modeling for the oxidation processes of ethanol. The present study shows that the available combustion mechanisms are still under-researched and thus, further experimental investigation and modeling validation of the ethanol combustion are needed, in particular at high temperatures.

6. Own publications

Reviewed Publications

- T. Kathrotia, M. Fikri, M. Bozkurt, M. Hartmann, U. Riedel, C. Schulz, *Study of the H + O + M reaction forming OH*: Kinetics of OH* chemiluminescence in hydrogen combustion systems*, Combust. Flame **157**, 1261 – 1273 (2010)
- M. Fikri, M. Bozkurt, H. Somnitz, C. Schulz, *High temperature shock-tube study of the reaction of gallium with ammonia*, Phys. Chem. Chem. Phys. **13**, 4149–4154 (2011)
- M. Bozkurt, M. Fikri, C. Schulz, *Investigation of the kinetics of OH* and CH* chemiluminescence in hydrocarbon oxidation behind reflected shock waves*, Appl. Physics B **107** (2012) 515-527

Conference Contributions

- M. Bozkurt, M. Hartmann, T. Kathrotia, U. Riedel, M. Fikri, C. Schulz, *Experimental and numerical investigation of OH* chemiluminescence in shock tubes: Reactions of highly diluted H_2/O_2 mixtures with various diluents*, European Combustion Meeting (ECM), Vienna, Austria, 2009
- B. Hidding, M. Fikri, M. Bozkurt, C. Schulz, T. Soltner, A. Kornath, M. Pfitzner, M. Lang, A.J. Adamczyk, L. Boradbelt, H. Ellerbrock, D. Simone, C. Bruno, *Spiking of hydrocarbon fuels with silanes-based combustion enhancers*, Transactions of the Japan Society for Aeronautical and Space Sciences, Aerospace Technology Japan **8**, 39 – 45 (2010)
- B. Hindding, P. Lorenz, F. Klaus, C. Hundsdörfer, A. Kornath, A. Kaufmann, S.M. Hadjizadeh, T. Soltner, T. Klapötke, M. Fikri, M. Bozkurt, S.H. Dürrstein, C. Schulz, X. Zhu, M. Möller, C. Bruno, D. Simone, F. Vergine, N. Eisenreich, C.A. Scharlemann, M. Pfitzner, M. Lang, G. Langel, H. Ellerbrock, J. Delis, R. Wagner, *Recent activities in silicone hydride research*, Proceedings of the 17th AIAA International. Space Planes and Hypersonic Systems and Technologies Conference, San Francisco, USA, 2011
- M. Bozkurt, M. Fikri, C. Schulz, *Experimental and numerical investigation of CH* and OH* chemiluminescence in acetylene combustion behind reflected shock waves*, 28th Intl. Symp. Shock Waves, Manchester, UK, 2011
- M. Bozkurt, D. Nativel, M. Aghsaee, M. Fikri, N. Chaumeix, C. Schulz, *Study of the kinetics of ethanol pyrolysis and oxidation*, 24th ICDERS, Taipei, Taiwan, 2013

7. Bibliography

1. G. Merker, C. Schwarz, G. Stiesch, F. Otto, *Internal Combustion Engines*, Springer-Verlag, Berlin, 2006.
2. H.-J. Wagner, M. K. Koch, J. Burkhardt, N. Feck, P. Kruse, *CO_2-Emissionen der Stromerzeugung*, *BWK* 59 (2007) 44-52.
3. M. P. Auer, C. Gebauer, K. G. Mosl, C. Hirsch, T. Sattelmayer, *Active instability control: feedback of combustion instabilities on the injection of gaseous fuel*, *J. Eng. Gas Turbines Power* 127 (2005) 748-754.
4. J. E. Harrington, K. C. Smyth, *Laser-Induced Fluorescence Measurements of Formaldehyde in a Methane/Air Diffusion Flame*, *Chemical Physics Letters* 202 (1993) 196-202.
5. P. H. Paul, H. N. Najm, *Planar laser-induced fluorescence imaging of flame heat release rate*, *Proc. Combust. Inst.* 27 (1998) 43-50.
6. Y. Hardalupas, M. Orain, *Local measurements of the time-dependent heat release rate and equivalence ratio using chemiluminescent emission from a flame*, *Combust. Flame* 139 (2004) 188-207.
7. Y. Hardalupas, C. S. Panoutsos, A. M. K. P. Taylor, *Spatial resolution of a chemiluminescence sensor for local heat-release rate and equivalence ratio measurements in a model gas turbine combustor*, *Exp. Fluids* 49 (2010) 883-909.
8. F. V. Tinaut, M. Reyes, B. Gimenez, J. V. Pastor, *Measurements of OH* and CH* Chemiluminescence in Premixed Flames in a Constant Volume Combustion Bomb under Autoignition Conditions*, *Energy Fuels* 25 (2011) 119-129.
9. N. Docquier, S. Belhalfaoui, F. Lacas, N. Darabiha, C. Rolon, *Experimental and numerical study of chemiluminescence in methane/air high-pressure flames for active control applications*, *Proc. Combust. Inst.* 28 (2000) 1765-1774.
10. T. S. Cheng, C. Y. Wu, Y. H. Li, Y. C. Chao, *Chemiluminescence measurements of local equivalence ratio in a partially premixed flame*, *Combust. Sci. Technol.* 178 (2006) 1821-1841.
11. V. Nori, J. M. Seitzman, *Chemiluminescence Measurements and Modeling in Syngas, Methane and Jet-A Fueled Combustors*, in: 45th AIAA Aerospace Sciences Meet. Exhib., Reno, NV, 2007.
12. N. Docquier, S. Candel, *Combustion control and sensors: a review*, *Prog. Energy Combust. Sci.* 28 (2002) 107-150.

13. M. Lauer, T. Sattelmayer, *On the Adequacy of Chemiluminescence as a Measure for Heat Release in Turbulent Flames With Mixture Gradients*, *J. Eng. Gas Turbines Power* 132 (2010) 061502/1-8.

14. M. Lauer, M. Zellhuber, T. Sattelmayer, C. J. Aul, *Determination of the Heat Release Distribution in Turbulent Flames by a Model Based Correction of OH* Chemiluminescence*, *J. Eng. Gas Turbines Power* 133 (2011) 121501/1-8.

15. M. Roeder, T. Dreier, C. Schulz, *Simultaneous measurement of localized heat release with OH/CH_2O-LIF imaging and spatially integrated OH* chemiluminescence in turbulent swirl flames*, *Appl. Phys. B* 107 (2012) 611-617.

16. J. Kojima, Y. Ikeda, T. Nakajima, *Basic aspects of OH(A), CH(A), and C_2(d) chemiluminescence in the reaction zone of laminar methane-air premixed flames*, *Combust. Flame* 140 (2005) 34-45.

17. J. G. Lee, D. A. Santavicca, *Experimental diagnostics for the study of combustion instabilities in lean premixed turbine combustors*, *J. Propul. Power* 19 (2003) 735-750.

18. N. Docquier, F. Lacas, S. Candel, *Closed-loop equivalence ratio control of premixed combustors using spectrally resolved chemiluminescence measurements*, *Proc. Combust. Inst.* 29 (2002) 139-145.

19. P. G. Aleiferis, Y. Hardalupas, A. M. K. P. Taylor, K. Ishii, Y. Urata, *Cyclic variations of fuel-droplet distribution during the early intake stroke of a lean-burn stratified-charge spark-ignition engine*, *Exp. Fluids* 39 (2005) 789-798.

20. T. M. Muruganandam, B. H. Kim, M. R. Morrell, V. Nori, M. Patel, B. W. Romig, J. M. Seitzman, *Optical equivalence ratio sensors for gas turbine combustors*, *Proc. Combust. Inst.* 30 (2005) 1601-1609.

21. J. Warnatz, U. Maas, R. W. Dibble, *Combustion*, Springer-Verlag, Berlin Heidelberg New York, 2006.

22. O. K. Rice, H. C. Ramsperger, *Theories of Unimolecular Gas Reactions at Low Pressures*, *J. Am. Chem. Soc.* 49 (1927) 1617-1629.

23. L. S. Kassel, *Studies in Homogeneous Gas Reactions. I*, *J. Phys. Chem.* 32 (1928) 225-242.

24. H. Eyring, *The Activated Complex in Chemical Reactions*, *J. Chem. Kin.* 3 (1935) 107-115.

25. M. Quack, J. Troe, *Specific Rate Constants of Unimolecular Processes II. Adiabatic Channel Model.*, *Ber. Bunsenges. Phys. Chem.* 78 (1974) 240-252.

26. J. Troe, *Specific rate constants k(E,J) for unimolecular bond fissions*, *J. Chem. Phys.* 79 (1983) 6017-6029.

27. M. Frenklach, M. Goldenberg, N. Moriarty, C. T. Bowman, R. K. Hanson, D. F. Davidson, W. C. Gardiner, Jr., V. Lissianski, G. P. Smith, D. M. Golden, R. V. Serauskas, *Optimized kinetics mechanism and calculator for natural gas combustion, NO_x production and reburning (GRI-MECH 3.0)*, *Proc. Int. Gas Res. Conf.* (1998) 329-336.

28. L. R. Cancino, M. Fikri, A. A. M. Oliveira, C. Schulz, *Ignition delay times of ethanol-containing multi-component gasoline surrogates: Shock-tube experiments and detailed modeling*, *Fuel* 90 (2011) 1238-1244.

29. C. I. Heghes, *Hydrocarbon Oxidation Mechanism*, PhD Thesis, University of Heidelberg, 2007.

30. D. L. Baulch, C. T. Bowman, C. J. Cobos, R. A. Cox, T. Just, J. A. Kerr, M. J. Pilling, D. Stocker, J. Troe, W. Tsang, R. W. Walker, J. Warnatz, *Evaluated kinetic data for combustion modeling: Supplement II*, *J. Phys. Chem. Ref. Data* 34 (2005) 757-1397.

31. J. Vandooren, J. Bian, *Validation of hydrogen/oxygen reaction mechanisms by comparison with the experimental structure of a rich hydrogen-oxygen flame*, *Proc. Combust. Inst.* 23 (1991) 341-346.

32. J. Warnatz, *The structure of laminar alkane-, alkene, and acetylene flames*, *Proc. Combust. Inst.* 18 (1981) 369-384.

33. C. K. Westbrook, F. L. Dryer, *Chemical kinetic modeling of hydrocarbon combustion*, *Prog. Energy Combust. Sci.* 10 (1984) 1-57.

34. J. A. Miller, R. E. Mitchell, M. D. Smooke, R. J. Kee, *Toward a comprehensive chemical kinetic mechanism for the oxidation of acetylene: comparison of model predictions with results from flame and shock tube experiments*, *Proc. Combust. Inst.* 19th (1982) 181-196.

35. H. Wang, A. Laskin, in: *A comprehensive kinetic model of ethylene and acetylene oxidation at high temperatures*, Progress Report of the Department of Mechanical Engineering: University of Delaware.

36. K. Natarajan, K. A. Bashkaran, *An experimental and analytical investigation of high-temperarture ignition of ethanol*, in: 13th International Symposium on Shock Waves, Niagara Falls, 1981.

37. A. A. Borisov, V. M. Zamanskii, A. A. Konnov, V. V. Lissyanskii, S. A. Rusakov, G. I. Skachkov, *High-temperature ignition of mixtures of ethanol and acetaldehyde with oxygen*, *Sov. J. Chem. Phys.* 4 (1989) 2561-2575.

38. N. M. Marinov, *A detailed chemical kinetic model for high temperature ethanol oxidation*, *Int. J. Chem. Kinet.* 31 (1999) 183-220.

39. P. Saxena, F. A. Williams, *Numerical and experimental studies of ethanol flames*, *Proc. Combust. Inst.* 31 (2007) 1149-1156.

40. J. Li, A. Kazakov, F. L. Dryer, *Experimental and Numerical Studies of Ethanol Decomposition Reactions*, *J. Phys. Chem. A* 108 (2004) 7671-7680.

41. W. Tsang, *Chemical kinetic database requirements for real fuels*, *Chem. Phys. Processes Combust.* (2001) 15-24.

42. J. Herzler, J. A. Manion, W. Tsang, *Single-Pulse Shock Tube Study of the Decomposition of Tetraethoxysilane and Related Compounds*, *J. Phys. Chem. A* 101 (1997) 5500-5508.

43. J. Li, A. Kazakov, M. Chaos, F. L. Dryer, *Chemical Kinetics of Ethanol Oxidation*, in: 5th US Combustion Meeting, San Diego, CA, 2007.

44. A. A. Borisov, V. M. Zamanskii, A. A. Konnov, V. V. Lissyanski, S. A. Rusakov, G. I. Skachkov, *A mechanism of high-temperature ethanol ignition*, *Sov. J. Chem. Phys.* 9 (1992) 2527-2537.

45. J. Kiecherer, T. Bentz, C. Hüllemann, K. Blumenstock, M. Olzmann, *Pyrolysis of Ethanol - Shock-Tube/TOF-MS Study and Kinetic Modeling*, in: 5th European Combustion Meeting, Cardiff, UK, 2011.

46. H. N. Najm, P. H. Paul, C. J. Mueller, P. S. Wyckoff, *On the adequacy of certain experimental observables as measurements of flame burning rate*, *Combust. Flame* 113 (1998) 312-332.

47. M. Röder, *Personal communication*.

48. A. G. Gaydon, *The Spectroscopy of Flames*, Wiley, New York, 1957.

49. D. Gutman, R. W. Lutz, N. F. Jacobs, E. A. Hardwidge, G. L. Schott, *Shock-tube study of OH chemiluminescence in the hydrogen-oxygen reaction*, *J. Chem. Phys.* 48 (1968) 5689-5694.

50. D. Gutman, S. Matsuda, *Shock-tube study of the acetylene-oxygen reaction. I. CH(A^2Delta --> X^2Pi) chemiluminescence and carbon monoxide production during the induction period*, *J. Chem. Phys.* 52 (1970) 4122-4132.

51. G. P. Smith, J. Luque, C. Park, J. B. Jeffries, D. R. Crosley, *Low pressure flame determinations of rate constants for OH(A) and CH(A) chemiluminescence*, *Combust. Flame* 131 (2002) 59-69.

52. J. M. Hall, E. L. Petersen, *Kinetics of OH chemiluminescence in the presence of hydrocarbons*, in: 40th AIAA Joint Propulsion and Exhibit, Fort Lauderdale, 2004.

53. J. M. Hall, J. de Vries, A. R. Amadio, E. L. Petersen, *Towards a Kinetics Model of CH Chemiluminescence*, in: 43th AIAA Aerospace Sciences Meeting and Exhibit, Reno, NV, 2005.

54. M. I. Savadatti, H. P. Broida, *Spectral study of flames of carbon vapor at low pressure*, *Western States Sect. Combust. Inst., Paper* WSS-CI 66-13 (1966) 12 pp.

55. J. Grebe, K. H. Homann, *Blue-green chemiluminescence in the system acetylene/atomic oxygen/atomic hydrogen. Formation of the emitters methylidyne (A^2Delta), diatomic carbon(d^3Pig) and ethynyl (C_2H*)*, *Ber. Bunsenges. Phys. Chem.* 86 (1982) 587-597.

56. G. P. Smith, C. Park, J. Schneiderman, J. Luque, *C_2 Swan band laser-induced fluorescence and chemiluminescence in low-pressure hydrocarbon flames*, *Combust. Flame* 141 (2005) 66-77.

57. D. L. Baulch, et al., *Evaluated Kinetic Data For High Temperature Reactions*, Butterworths & Co. Ltd, London/Boston, 1976.

58. A. M. Pravilov, L. G. Smirnova, *Temperature dependence of the spectral distribution of the chemiluminescence rate constant in the $O(^3P) + CO \rightarrow CO_2 + hv$*, *Kinet. Katal.* 22 (1981) 832-838.

59. M. Slack, A. Grillo, *High temperature rate coefficient measurements of carbon monoxide + atomic oxygen chemiluminescence*, *Combust. Flame* 59 (1985) 189-196.

60. M. Kopp, M. Brower, O. Mathieu, E. Petersen, F. Guethe, *CO_2* chemiluminescence study at low and elevated pressures*, *Appl. Phys. B* 107 (2012) 529-538.

61. M. Bozkurt, M. Fikri, C. Schulz, *Investigation of the kinetics of OH* and CH* chemiluminescence in hydrocarbon oxidation behind reflected shock waves*, *Appl. Phys. B* 107 (2012) 515-527.

62. B. Prabasena, M. Roeder, T. Kathrotia, U. Riedel, T. Dreier, C. Schulz, *Strain rate and fuel composition dependence of chemiluminescent species profiles in non-premixed counterflow flames: comparison with model results*, *Appl. Phys. B* 107 (2012) 561-569.

63. P. Nau, J. Krueger, A. Lackner, M. Letzgus, A. Brockhinke, *On the quantification of OH*, CH*, and C_2* chemiluminescence in flames*, *Appl. Phys. B* 107 (2012) 551-559.

64. A. Brockhinke, J. Krueger, M. Heusing, M. Letzgus, *Measurement and simulation of rotationally-resolved chemiluminescence spectra in flames*, *Appl. Phys. B* 107 (2012) 539-549.

65. T. Kathrotia, U. Riedel, A. Seipel, K. Moshammer, A. Brockhinke, *Experimental and numerical study of chemiluminescent species in low-pressure flames*, *Appl. Phys. B* 107 (2012) 571-584.

66. T. Koike, K. Morinaga, *Further studies of the rate constant for chemical excitation of hydroxyl in shock waves*, *Bull. Chem. Soc. Jpn.* 55 (1982) 52-54.

67. M. De Leo, A. Saveliev, L. A. Kennedy, S. A. Zelepouga, *OH and CH luminescence in opposed flow methane oxy-flames*, *Combust. Flame* 149 (2007) 435-447.

68. M. Tamura, P. A. Berg, J. E. Harrington, J. Luque, J. B. Jeffries, G. P. Smith, D. R. Crosley, *Collisional quenching of CH(A), OH(A), and NO(A) in low pressure hydrocarbon flames*, *Combust. Flame* 114 (1998) 502-514.

69. M. Klessinger, J. Michl, *Physical Organic Chemistry, Vol. 6: Light Absorption and Photochemistry of Organic Molecules*, VCH, New York, 1990.

70. M. I. Lester, R. A. Loomis, R. L. Schwartz, S. P. Walch, *Electronic Quenching of OH $A^2\Sigma^+$ (v' = 0, 1) Complexes with Hydrogen and Nitrogen*, *J. Phys. Chem. A* 101 (1997) 9195-9206.

71. D. T. Anderson, M. W. Todd, M. I. Lester, *Reactive quenching of electronically excited OH radicals in collisions with molecular hydrogen*, *J. Chem. Phys.* 110 (1999) 11117-11120.

72. L. P. Dempsey, C. Murray, M. I. Lester, *Product branching between reactive and nonreactive pathways in the collisional quenching of OH $A^2\Sigma^+$ radicals by H_2*, *J. Chem. Phys.* 127 (2007) 151101/1-4.

73. G. C. Light, *The effect of vibrational excitation on the reaction of atomic oxygen(^3P) with molecular hydrogen and the distribution of vibrational energy in the product hydroxyl*, *J. Chem. Phys.* 68 (1978) 2831-2843.

74. A. Lifshitz, H. Teitelbaum, *The unusual effect of reagent vibrational excitation on the rates of endothermic and exothermic elementary combustion reactions*, *Chem. Phys.* 219 (1997) 243-256.

75. A. M. Starik, B. I. Lukhovitskii, V. V. Naumov, N. S. Titova, *On combustion enhancement mechanisms in the case of electrical-discharge-excited oxygen molecules*, *Tech. Phys.* 52 (2007) 1281-1290.

76. K. H. Becker, B. Engelhardt, H. Geiger, R. Kurtenbach, P. Wiesen, *Temperature dependence of the reactions of CH radicals with NO, NH_3 and N_2O in the range 200-1300 K*, *Chem. Phys. Lett.* 210 (1993) 135-140.

77. S. L. N. G. Krishnamachari, H. P. Broida, *Effect of molecular oxygen on the emission spectra of atomic oxygen-acetylene flames*, *J. Chem. Phys.* 34 (1960) 1709-1711.

78. J. M. Hall, E. L. Petersen, *An optimized kinetics model for OH chemiluminescence at high temperatures and atmospheric pressures*, *Int. J. Chem. Kinet.* 38 (2006) 714-724.

79. T. Kathrotia, M. Fikri, M. Bozkurt, M. Hartmann, U. Riedel, C. Schulz, *Study of the H + O + M reaction forming OH*: Kinetics of OH* chemiluminescence in hydrogen combustion systems*, *Combust. Flame* 157 (2010) 1261-1273.

80. C. J. Jachimowski, *Kinetics of oxygen atom formation during the oxidation of methane behind shock waves*, *Combust. Flame* 23 (1974) 233-248.

81. H. P. Broida, A. G. Gaydon, *Luminous reaction between carbon monoxide and atomic oxygen*, *Trans. Faraday Soc.* 49 (1953) 1190-1193.

82. E. Petersen, M. Kopp, N. Donato, F. Güthe, *Assessment of Current Chemiluminescence Kinetics Models at Engine Conditions*, *J. Eng. Gas Turbines Power* 134 (2012) 051501/1-7.

83. J. Luque, D. R. Crosley, LIFBASE (version 2.0.6), Report MP 99-009, SRI International, Menlo Park, CA, 1999.

84. M. Letzgus, A. Brockhinke, K. Kohse-Hoeinghaus, LASKINv^2. Bielefeld University, Chemistry Department, Physical Chemistry 1, available at: http://pc1.uni-bielefeld.de/~laskin, 2012

85. A. G. Gaydon, H. G. Wolfhard, *Excitation of the OH spectrum in flames at low pressures*, *Rev. Inst. Franc. Petrole* 4 (1949) 405-417.

86. W. R. Kane, H. P. Broida, *Rotational "temperatures" of OH in diluted flames*, *J. Chem. Phys.* 21 (1953) 347-354.

87. H. P. Broida, D. F. Heath, *Spectroscopic survey of energy distributions of OH, C_2, and CH radicals in low pressure acetylene-oxygen flames*, *J. Chem. Phys.* 26 (1957) 223-229.

88. E. F. Greene, J. P. Toennies, *Chemische Reaktionen in Stosswellen*, Dr. Dietrich Steinkopff Verlag, Darmstadt, 1962.

89. A. G. Gaydon, I. R. Hurle, *The Shock Tube in High Temperature Chemical Physics*, Chapman and Hall Ltd., London, 1963.

90. H. Oertel, *Stossrohre*, Springer Verlag, Wien, New York, 1966.

91. J. Herzler, L. Jerig, P. Roth, *Shock-tube study of the ignition of propane at intermediate temperatures and high pressures*, *Combust. Sci. Technol.* 176 (2004) 1627-1637.

92. R. J. Kee, F. M. Rupley, J. A. Miller, M. E. Coltrin, J. F. Grcar, E. Meeks, H. K. Moffat, A. E. Lutz, G. Dixon-Lewis, M. D. Smooke, J. Warnatz, G. H. Evans, R. S.

Larson, R. E. Mitchell, L. R. Petzold, W. C. Reynolds, M. Caracotsios, W. E. Stewart, P. Glarborg, C. Wang, O. Adigun, in: *CHEMKIN Collection*, San Diego, CA, 2000; Vol. Release 3.6.

93. M. Colberg, *Aufbau und Charakterisierung einer Stoßwellenapparatur zur Untersuchung von Hochtemperaturreaktionen des Formylradikals*, PhD Thesis, University of Kiel, 2006.

94. G. Friedrichs, M. Colberg, M. Fikri, Z. Huang, J. Neumann, F. Temps, *Validation of the Extended Simultaneous Kinetics and Ringdown Model by Measurements of the Reaction $NH_2 + NO$*, *J. Phys. Chem. A* 109 (2005) 4785-4795.

95. K. Kohse-Hoeinghaus, D. F. Davidson, A. Y. Chang, R. K. Hanson, *Quantitative amidogen concentration determination in shock tube laser-absorption experiments*, *J. Quant. Spectrosc. Radiat. Transfer* 42 (1989) 1-17.

96. D. F. Davidson, K. Kohse-Hoeinghaus, A. Y. Chang, R. K. Hanson, *A pyrolysis mechanism for ammonia*, *Int. J. Chem. Kinet.* 22 (1990) 513-535.

97. J. T. Herbon, R. K. Hanson, D. M. Golden, C. T. Bowman, *A shock tube study of the enthalpy of formation of OH*, *Proc. Combust. Inst.* 29 (2002) 1201-1208.

98. D. F. Davidson, M. A. Oehlschlaeger, J. T. Herbon, R. K. Hanson, *Shock tube measurements of iso-octane ignition times and OH concentration time histories*, *Proc. Combust. Inst.* 29 (2002) 1295-1301.

99. J. T. Herbon, *Shock Tube Measurements of $CH_3 + O_2$ Kinetics and the Heat of Formation of the OH Radical*, PhD Thesis, Stanford University, 2004.

100. M. Markus, *Laser-Anwendungen in der Hochtemperaturkinetik: Farbstoff-Ringlaser-Spektroskopie und UV-Laser-Photolyse*, PhD Thesis, University of Duisburg, 1995.

101. A. Y. Chang, D. F. Davidson, M. Di Rosa, R. K. Hanson, C. T. Bowman, *Shock Tube Experiments for Development and Validation of Kinetic Models of Hydrocarbon Oxidation*, in: 25th Intl. Symposium on Combustion, Poster 2-23, Irvine, CA, 1994.

102. S. H. Duerrstein, M. Aghsaee, L. Jerig, M. Fikri, C. Schulz, *A shock tube with a high-repetition-rate time-of-flight mass spectrometer for investigations of complex reaction systems*, *Rev. Sci. Instrum.* 82 (2011) 084103/1-7.

103. R. S. Tranter, S. J. Klippenstein, L. B. Harding, B. R. Giri, X. Yang, J. H. Kiefer, *Experimental and Theoretical Investigation of the Self-Reaction of Phenyl Radicals*, *J. Phys. Chem. A* 114 (2010) 8240-8261.

104. R. S. Tranter, B. R. Giri, J. H. Kiefer, *Shock tube/time-of-flight mass spectrometer for high temperature kinetic studies*, *Rev. Sci. Instrum.* 78 (2007) 034101/1-11.

105. W. E. Kaskan, *Abnormal excitation of OH in $H_2/O_2/N_2$ flames*, *J. Chem. Phys.* 31 (1959) 944-956.

106. F. E. Belles, M. R. Lauver, *Origin of OH chemiluminescence during the induction period of the H_2-O_2 reaction behind shock waves*, *J. Chem. Phys.* 40 (1964) 415-422.

107. W. C. Gardiner, Jr., K. Morinaga, D. L. Ripley, T. Takeyama, *Shock-tube study of OH (^{2}Sigma --> ^{2}Pi) luminescence*, *Phys. Fluids* 12 (1969) 120-124.

108. C. S. T. Marques, L. H. Benvenutti, C. A. Bertran, *Kinetic modeling for chemiluminescent radicals in acetylene combustion*, *J. Braz. Chem. Soc.* 17 (2006) 302-315.

109. O. V. Skrebkov, Y. P. Myagkov, S. P. Karkach, V. M. Vasil'ev, A. L. Smirnov, *Formation mechanism of the excited OH(^{2}Sigma$^+$) radical during the ignition of the diluted H_2-O_2 mixture by shock waves*, *Dokl. Phys. Chem.* 383 (2002) 93-96.

110. M. Charton, A. G. Gaydon, *Excitation spectra of OH in hydrogen flames and its relation to excess concentrations of free atoms*, *Proc. R. Soc. London, Ser. A* 245 (1958) 84-92.

111. Y. Hidaka, S. Takahashi, H. Kawano, M. Suga, W. C. Gardiner, Jr., *Shock-tube measurement of the rate constant for excited hydroxyl(A^{2}Sigma$^+$) formation in the hydrogen-oxygen reaction*, *J. Phys. Chem.* 86 (1982) 1429-1433.

112. G. P. Smith, C. Park, J. Luque, *A note on chemiluminescence in low-pressure hydrogen and methane-nitrous oxide flames*, *Combust. Flame* 140 (2005) 385-389.

113. E. L. Petersen, D. M. Kalitan, M. J. A. Rickard, *Calibration and Chemical Kinetics Modelling of an OH Chemiluminescence Diagnostics*, in: 39th AIAA Joint Propulsion Conference and Exhibit, Huntsville, AL, 2003.

114. R. P. Porter, A. H. Clark, W. E. Kaskan, W. E. Browne, *Study of hydrocarbon flames*, *Proc. Combust. Inst.* 11 (1967) 907-917.

115. T. Koike, *Mixture dependencies of OH($^2\Sigma$) produced in the oxidations of C_2H_2 and C_2H_6 in shock waves*, *Bull. Chem. Soc. Jpn.* 64 (1991) 1017-1018.

116. K. T. Walsh, M. B. Long, M. A. Tanoff, M. D. Smooke, *Experimental and computational study of CH, CH*, and OH* in an axisymmetric laminar diffusion flame*, *Proc. Combust. Inst.* 27 (1998) 615-623.

117. S. A. Carl, M. Van Poppel, J. Peeters, *Identification of the CH + O_2 -> OH(A) + CO Reaction as the Source of OH(A-X) Chemiluminescence in C_2H_2/O/H/O_2 Atomic Flames and Determination of Its Absolute Rate Constant over the Range T = 296 to 511 K*, *J. Phys. Chem. A* 107 (2003) 11001-11007.

118. P. H. Paul, J. L. Durant, Jr., J. A. Gray, M. R. Furlanetto, *Collisional electronic quenching of OH A^2Sigma (n' = 0) measured at high temperature in a shock tube*, *J. Chem. Phys.* 102 (1995) 8378-8384.

119. K. H. Becker, D. Haaks, T. Tatarczyk, *Natural lifetime of hydroxyl($^2\Sigma^+$,v=O,N=2,J=3/2) and its quenching by atomic hydrogen*, *Chem. Phys. Lett.* 24 (1974) 564-567.

120. P. W. Fairchild, G. P. Smith, D. R. Crosley, *Collisional quenching of $A^2\Sigma^+$ hydroxyl at elevated temperatures*, *J. Chem. Phys.* 79 (1983) 1795-1807.

121. J. B. Jeffries, K. Kohse-Hoeinghaus, G. P. Smith, R. A. Copeland, D. R. Crosley, *Rotational-level-dependent quenching of hydroxyl($A^2\Sigma^+$) at flame temperatures*, *Chem. Phys. Lett.* 152 (1988) 160-166.

122. A. E. Bailey, D. E. Heard, P. H. Paul, M. J. Pilling, *Collisional quenching of OH ($A^2\Sigma^+$, v' = 0) N_2, O_2 and CO_2 between 204 and 294 K Implications for atmospheric measurements of OH by laser-induced fluorescence*, *J. Chem. Soc., Faraday Trans.* 93 (1997) 2915-2920.

123. B. L. Hemming, D. R. Crosley, J. E. Harrington, V. Sick, *Collisional quenching of high rotational levels in $A^2\Sigma^+$ OH*, *J. Chem. Phys.* 115 (2001) 3099-3104.

124. B. L. Hemming, D. R. Crosley, *Rotational-Level Dependence of OH $A^2\Sigma^+$ Quenching at 242 and 196 K*, *J. Phys. Chem. A* 106 (2002) 8992-8995.

125. D. E. Heard, D. A. Henderson, *Quenching of OH ($A^2\Sigma^+$, v' = 0) by several collision partners between 200 and 344 K. Cross-section measurements and model comparisons*, *Phys. Chem. Chem. Phys.* 2 (2000) 67-72.

126. K. Kohse-Hoeinghaus, J. B. Jeffries, Editors, *Applied Combustion Diagnostics: Combustion an International Series*, CRC Press, New York, 2002.

127. R. J. Cattolica, T. G. Mataga, *Rotational-level-dependent quenching of hydroxyl $A^2\Sigma$ (v' = 1) by collisions with water in a low-pressure flame*, *Chem. Phys. Lett.* 182 (1991) 623-631.

128. U. Maas, J. Warnatz, *Ignition processes in hydrogen-oxygen mixtures*, *Combust. Flame* 74 (1988) 53-69.

129. O. V. Skrebkov, S. P. Karkach, V. M. Vasil'ev, A. L. Smirnov, *Hydrogen-oxygen reactions behind shock waves assisted by OH(^{2}Sigma$^+$) formation*, *Chem. Phys. Lett.* 375 (2003) 413-418.

130. G. D. Smekhov, L. B. Ibraguimova, S. P. Karkach, O. V. Skrebkov, O. P. Shatalov, *Numerical simulation of ignition of a hydrogen-oxygen mixture in view of electronically excited components*, *High Temp.* 45 (2007) 395-407.

131. P. A. Berg, D. A. Hill, A. R. Noble, G. P. Smith, J. B. Jeffries, D. R. Crosley, *Absolute CH concentration measurements in low-pressure methane flames: comparisons with model results*, *Combust. Flame* 121 (2000) 223-235.

132. T. Kathrotia, *Reaction Kinetics Modeling of OH*, CH*, and C_2* Chemiluminescence*, PhD thesis, University of Heidelberg, 2011.

133. J. D. Mertens, *A shock tube study of CH* reactions kinetics in CH_4 and C_2H_2 oxidation*, in: 22nd International Symposium on Shock Waves, London, UK, 1999.

134. C. S. Panoutsos, Y. Hardalupas, A. M. K. P. Taylor, *Numerical evaluation of equivalence ratio measurement using OH* and CH* chemiluminescence in premixed and non-premixed methane-air flames*, *Combust. Flame* 156 (2009) 273-291.

135. M. Orain, Y. Hardalupas, *Effect of fuel type on equivalence ratio measurements using chemiluminescence in premixed flames*, *Comptes Rendus Mecanique* 338 (2010) 241-254.

136. H. P. Broida, A. G. Gaydon, *The mechanism of formation of OH, CH, and HCO in flame spectra with deuterium as tracer*, *Proc. R. Soc. London, Ser. A* 218 (1953) 60-69.

137. A. M. Bass, H. P. Broida, *Spectrophotometric atlas of the spectrum of CH from 3000 to 5000 A*, *NBS Monogr. (U. S.)* 24 (1961) 20 pp.

138. R. Bleekrode, W. C. Nieuwpoort, *Absorption and emission measurements of C_2 and CH electronic bands in low-pressure oxyacetylene flames*, *J. Chem. Phys.* 43 (1965) 3680-3687.

139. E. M. Bulewicz, P. J. Padley, R. E. Smith, *Spectroscopic studies of C_2, CH and OH radicals in low pressure acetylene + oxygen flames*, *Proc. Roy. Soc., Ser. A* 315 (1970) 129-147.

140. G. P. Glass, G. B. Kistiakowsky, J. V. Michael, H. Niki, *Mechanism of the acetylene-oxygen reaction in shock waves*, *J. Chem. Phys.* 42 (1965) 608-621.

141. W. Brennen, T. Carrington, *Chemiluminescence of CH in the O + C_2H_2 reaction: rotational relaxation and quenching*, *J. Chem. Phys.* 46 (1967) 7-18.

142. R. G. Joklik, J. W. Daily, W. J. Pitz, *Measurements of methylidyne concentrations in an acetylene/oxygen flame and comparisons to modeling calculations*, *Proc. Combust. Inst.* 21 (1988) 895-904.

143. K. Devriendt, H. Van Look, B. Ceursters, J. Peeters, *Kinetics of formation of chemiluminescent CH(A^2Delta) by the elementary reactions of $C_2H(X^2Sigma^+)$ with $O(^3P)$ and $O_2(X^3Sigma^{g-})$: a pulse laser photolysis study*, *Chem. Phys. Lett.* 261 (1996) 450-456.

144. K. Devriendt, J. Peeters, *Direct Identification of the $C_2H(X^2Sigma^+)$ + $O(^3P)$ -> $CH(A^2Delta)$ + CO Reaction as the Source of the $CH(A^2Delta$ -> $X^2Pi)$ Chemiluminescence in C_2H_2/O/H Atomic Flames*, *J. Phys. Chem.* 101 (1997) 2546-2551.

145. R. M. I. Elsamra, S. Vranckx, S. A. Carl, *$CH(A^2Delta)$ Formation in Hydrocarbon Combustion: The Temperature Dependence of the Rate Constant of the Reaction C_2H + O_2 -> $CH(A^2Delta)$ + CO_2*, *J. Phys. Chem. A* 109 (2005) 10287-10293.

146. C. W. Hand, G. B. Kistiakowsky, *Ionization accompanying the acetylene-oxygen reaction in shock waves*, *J. Chem. Phys.* 37 (1962) 1239-1245.

147. S. Matsuda, I. R. Slagle, D. J. Fife, J. R. Marquart, D. Gutman, *Shock-tube study of the acetylene-oxygen reaction. IV. Kinetic study of CH, C_2, and continuum chemiluminescence during the induction period*, *J. Chem. Phys.* 57 (1972) 5277-5285.

148. A. M. Renlund, F. Shokoohi, H. Reisler, C. Wittig, *Gas phase reactions of ethynyl radical(~X^2Sigma^+) with oxygen, hydrogen, and methane studied via time-resolved product emissions*, *Chem. Phys. Lett.* 84 (1981) 293-299.

149. S. M. Hwang, W. C. Gardiner, Jr., M. Frenklach, Y. Hidaka, *Induction zone exothermicity of acetylene ignition*, *Combust. Flame* 67 (1987) 65-75.

150. B. A. Williams, L. Pasternack, *The effect of nitric oxide on premixed flames of CH_4, C_2H_6, C_2H_4, and C_2H_2*, *Combust. Flame* 111 (1997) 87-110.

151. S. Wagner, M. Klein, T. Kathrotia, U. Riedel, T. Kissel, A. Dreizler, V. Ebert, *In situ TDLAS measurement of absolute acetylene concentration profiles in a non-premixed laminar counter-flow flame*, *Appl. Phys. B* 107 (2012) 585-589.

152. C. Chen, Y. Sheng, S. Yu, X. Ma, *Investigation of the collisional quenching of $CH(A^2\Delta$ and $B^2\Sigma)$ by Ar, O_2, CS_2, alcohol, and halomethane molecules*, *J. Chem. Phys.* 101 (1994) 5725-5730.

153. N. L. Garland, D. R. Crosley, *Collisional quenching of methylidyne $(CH)A^2Delta$, v' = 0 at 1300 K*, *Chem. Phys. Lett.* 134 (1987) 189-194.

154. W. Ren, A. Farooq, D. F. Davidson, R. K. Hanson, *CO concentration and temperature sensor for combustion gases using quantum-cascade laser absorption near 4.7 μm*, *Appl. Phys. B* 107 (2012) 849-860.

155. R. Sivaramakrishnan, M. C. Su, J. V. Michael, S. J. Klippenstein, L. B. Harding, B. Ruscic, *Rate Constants for the Thermal Decomposition of Ethanol and Its Bimolecular Reactions with OH and D: Reflected Shock Tube and Theoretical Studies*, *J. Phys. Chem. A* 114 (2010) 9425-9439.

8. List of abbreviations

CL	Chemiluminescence
LIF	Laser-induced fluorescence
LII	Laser-induced incandescence
Ma	Mach number
RDLAS	Ring-dye laser absorption spectroscopy
RET	Rotational energy transfer
TOF-MS	Time-of-flight mass spectrometry
VET	Vibrational energy transfer

9. Symbols

A_{21}	Einstein coefficient for spontaneous emission
c_p	Heat capacity
E	Total energy
E_a	Activation energy
h	Specific enthalpy
h	Planck constant
I	Transmitted light intensity
I_0	Reference light intensity
J	Rotational quantum number
K_C	Equilibrium constant
k	Rate coefficient
l	Absorption length
M	Molar mass
n	Exponential factor
p	Pressure
R	Gas constant
R	Rate of formation
T	Temperature
t	Time
u	Specific internal energy
v	Vibrational quantum number
v	Stoichiometric coefficient
x_i	Mole fraction
δ	Relative error
κ	Heat capacity ratio
λ	Wavelength
v	Wave number

ρ	Density
σ	Absorption cross section
τ	Peak time

10. Acknowledgement

First of all, I thankfully acknowledge my supervisor Prof. Dr. Christof Schulz for giving me the opportunity to work in his group and to finish my dissertation. I am grateful to him for his encouraged support and his guidance throughout my work.

I am very grateful to my group leader Dr. Mustapha Fikri, who took me under his wings and who has continuously and energetically instructed and motivated me during my research. I would like to express my deepest appreciation to him for his great scientific and personal support. Without his persistent patience and help this dissertation would not have been possible.

Special thanks go to my colleague Mohammad Aghsaee for his great support in performing and evaluating the TOF-MS experiments.

Further I want to gratefully acknowledge Dr. Axel Hoffmann for his great support and his steady engagement in reactivating and optimizing the "new" ring-dye laser and the development of the differential detection setup. Special thanks to Jürgen Leistikow for his accurate construction of the detection setup.

I want to acknowledge my current and former colleagues of the kinetics group: Matthias Beuting, Leonel Cancino, Steffen Dürrstein, Bo Shu and Siavash Zabeti.

My hearty thanks to Dr. Ralf Starke for his organizational and personal guidance. It has been a great pleasure to work alongside him for the past five years. I express my thanks to Dieter Hermanns for his technical assistance and the fruitful non-scientific discussions. Additional thanks to Ludger Jerig for his helpful technical hints.

I wish to thank our outstanding laboratory assistants Birgit Nelius, Natascha Schlösser and Beate Endres for their continuous and helpful assistance in the lab. My special thanks go to our all-round man Jörg Albrecht for his speedy technical assistance in the workshop. Further thanks to Barbara Nota and Barbara Graf for managing the administrative tasks.

Special thanks to Dr. Khadijeh Mohri and Dr. Brandon Rotavera for doing the proof-reading.

Further thanks to the whole IVG group and to my colleagues in the ChemLum project for the prosperous collaboration. It was a pleasure for me to work with you in a very friendly and familiar atmosphere which will be a pleasant memory.

Special thanks to my parents Hatice and Ağahan Bozkurt and to my brother Oğuzhan Bozkurt for their steady support and their motivation.

Finally, I would like to thank my beloved wife Burcu for her never-ending optimism, motivation, support and patience throughout my study. This thesis is dedicated to our dearest son, Egehan, born on the 12th December 2010